Table of Content

Asian Power Electronics Journal, Vol. 2, No. 1, Apr 2008

Comparison of Neural Network and Fast Fourier Transform Based Selective Harmonic Extraction and Total Harmonic Reduction for Power Electronic Converters

E.Chandra Sekaran[1] and P.Anbalagan[2]

Abstract - A new strategy to estimate harmonic distortion from an AC line is presented for power electronic converters. An Adaptive linear neural network (ADALINE) is used to determine precisely the necessary currents in order to cancel harmonics. The proposed strategy is based on an original decomposition of the measured currents to specify the neural network inputs. This new decomposition is based on the Fourier series analysis of the current signals and Least Mean Square (LMS) training algorithm carries out the weights. This new estimation strategy appreciably improves the performances of traditional compensating methods and is valid both for single-phase and three-phase systems. The proposed strategy also allows extracting the harmonics individually. The method is based on the extraction of fundamental components of distorted line current using an ADALINE network. The output of the ADALINE is compared with distorted supply current to construct modulating signals and to generate PWM pulses for active line conditioner. Speed and accuracy of ADALINE results in improved performance of the active power line filter. In this paper converter is used as a non-linear load. The performance of ADALINE is verified with single phase fully controlled AC-DC converter simulated with neural network based active filter using MATLAB/SIMULINK. Also in this paper, harmonic components can be selectively extracted using ADALINE network and harmonic content analyzed by artificial neural network (ANN) is compared with the Fast Fourier Transform (FFT).

Keywords - FFT, ADALINE, LMS, Active Power Filter, THD

I. INTRODUCTION

The deterioration of currents and voltages in electrical networks is due to the presence of non-linear loads (rectifiers, variable speed transmissions, lighting etc) absorbing non sinusoidal currents. These harmonic current circulate in the electrical network, disturb the correct operation of the components and even it may damage them. The harmonic compensators called Active Power Filters (APFs) are advanced solutions for eliminating harmonic distortion [1]. APFs are able to correct the power factor without any additional equipment. The concept of the active power filter is to detect or extract the unwanted harmonic components of a line current, and then to generate and inject a signal into the line in such a way to produce partial or total cancellation of the unwanted components.

Active power filters could be connected either in series or in parallel to power systems. Therefore, they can operate as either voltage sources or current sources. The shunt active filter is controlled to inject a compensating current into the utility system so that it cancels the harmonic currents produced by the nonlinear load. B.M.Bird, the first attempts to reduce harmonics without the use of conventional passive filter [2]. Their proposed design is changing the waveform of the current drawn by the load by injecting a third harmonic current, displaced in phase, in to the converter itself. With this method it is not possible to eliminate all the harmonic components. Ametani, et.al proposed an idea to expand the current injection method by to eliminate multiple harmonics [3]. According to this theory, an active control circuit could be used to precisely shape the injected current. Ideally this current would contain harmonic currents of opposing phase, thus the harmonics would be neutralized, and only the fundamental component would remain. Ametani was not successful in producing a practical circuit capable of creating a precise current. The total harmonic distortion was reduced, but single harmonics were not completely eliminated. Gyugyi and Strycula presented the concept to compensate for harmonics by the applications of semiconductor switches in the form of PWM inverter [4]. They developed a method by injecting PWM current using Voltage Source Inverter (VSI) and Current Source Inverter (CSI), results are verified experimentally.Akagi, and et.al introduced PQ theory and developed a PWM voltage type converter topology for instantaneous reactive power compensation [5]. In their work, the authors decomposed the instantaneous voltages and currents into orthogonal components yielding, in the time domain, a component termed the instantaneous reactive power. The active filter is controlled to eliminate this instantaneous reactive power thus resulting in reactive power compensation in the time domain.

The performance in terms of the harmonic compensation strongly depends on the selected identification method. Indeed, an efficient control device will not be able to make the sufficient corrections if the harmonic currents are badly identified. For this reason several identification methods have been developed in recent years. For example, Kalman filters have been applied with the need for a dynamic state model [6]. The simplest way to identify harmonics and generate the harmonic current is to use discrete Fourier transformation (DFT) of fast Fourier transformation (FFT). Although it has wide applications, the DFT or FFT has certain limitations in harmonic analysis [7]. The Fast Fourier Transform (FFT), which needs a lot of computation resources, has also been applied. [8] Presently, neural network has received special

---

The paper first received 04 Apr 2006 and in revised form 27 Mar 2008
Digital ref: AI70201121

[1] Senior Lecturer, Department of Electrical and Electronics Engineering, Coimbatore Institute of Technology, Coimbatore. INDIA.
[2] Professor and HOD, Department of Electrical and Electronics Engineering, Coimbatore Institute of Technology, Coimbatore. INDIA.
E-mail : ecs04@rediffmail.com

attention from researchers because of its simplicity, learning and generalization ability, and it has been applied in the field of engineering , such as in harmonic detection since early 1900s[9].

K.Hartana and G.G.Richards were among the first who used back propagation ANN to track harmonics in large power systems, where it is difficult to locate the magnitude of the unknown sources [10]. In their method, an initial estimation of the harmonic source in a power system was made using neural network. P.K.Dash et.al utilized the ADALINE, a version of ANN, as a new harmonic estimation technique [11]. The learning rule of the method is based on the LMS introduced by Widro-Hoff. J.R.Vazquez and P.Salmeron presented an active power filter control using neural network technologies. The proposed control design is a pulse width modulation control with two blocks that include neural networks [12]. Adaptive networks estimate the compensation currents. In their scheme, J.R.Vazquez and P.Salmeron used two signals load voltage and load current as the input to the adaptive network block and the compensation current is compared with actual current error, is trained in feed forward network block. The actual compensation currents are the result of controlling the switching logic of the power transistors.

In this paper an improved scheme is proposed in which only the actual load current is given to adaptive neural network and the reference current is obtained. The load voltage is given to a DC regulator with a simple PI controller which gives the actual filter current and which is compared with reference current the gating pulses to IGBTs are provided through a hysteresis band comparator. The proposed model can be used to eliminate harmonics in on line. The ADALINE neural network uses to separate the fundamental component form the distorted supply current. Based on the Fourier series, this new decomposition of current signals allows to define the neural network inputs for which an LMS algorithm carriers out the weights training. The method utilizes adaptive neurons (ADALINE) to process the signals obtained from the line. This ADALINE is current ADALINE. [13, 14]

This current ADALINE extracts the fundamental components of the distorted line current signal and the output of the ADALINE is compared with distorted supply current to construct the modulating signal. This modulating signal is used to generate the PWM pulses and PWM pulses are fed to the active power filter to generate compensating current. This compensating current is fed against to the distorted line current. Thus the power quality will be maintained.

Many frequency domain approaches to active power line conditioning are available, among these ADALINE-based harmonic extraction has been chosen because of its superior characteristics compared with other available methods. [6, 8, 13].
In the following sections, first basic principle of harmonic compensation is discussed. In section III ADALINE based Active Power Filter is explained with detailed discussion on basics of LMS or Widrow-Hoff learning rule. In section IV proposed scheme is described with simulated model. In section V the simulated results are given. In section VI comparisons of the results are given with the advantages of the proposed scheme.

II. BASIC PRINCIPLE

The harmonic compensation is of high importance for the energy suppliers as well as consumers. The APF thus constitutes the solution the most commonly used today in industry [15]. These systems are placed in derivation between the nonlinear load and the electrical supply network. Only small portion of the energy is processed, resulting in greater overall efficiency and increased power processing capability. An identifying module estimates the harmonic currents from the AC line and a control module injects these currents in the network. The second module strongly depends on the first one. Indeed, if the harmonic currents are badly identified, this inevitably involves a lower quality of the compensation. Several methods can be used to estimate the harmonic currents in an electrical network [1, 13].

A typical topology of a shunt active filter is shown in Fig.1 The active filter injects the equal amplitude compensating currents, opposite in phase, at the point of connection to cancel the harmonics currents caused by any nonlinear load.

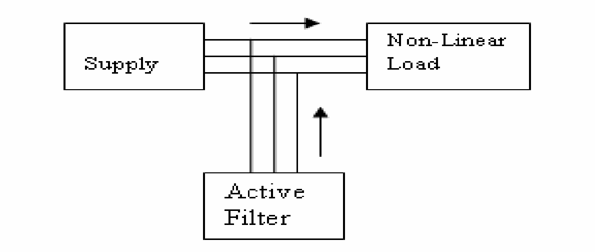

Fig. 1: Simplified diagram of a shunt active filter

III. LINEAR ADAPTIVE NEURAL NETWORK (ADALINE)

Neural networks are composed of simple elements operating in parallel. These elements are inspired by biological nervous systems. As in nature, the network function is determined largely by the connections between elements. A neural network can be trained to perform a particular function by adjusting the values of the connections (weights) between elements.

The ADALINE networks are similar to the perceptron, but their transfer function is linear rather than hard-limiting. This allows their outputs to take on any value, whereas the perceptron output is limited to either 0 or 1. Both the ADALINE and the perceptron can only solve linearly separable problems. However, here the Least Mean Square (LMS) learning rule is used, which is much more powerful than the perceptron learning rule. The LMS or Widrow-Hoff learning rule minimizes the mean square error and, thus, moves the decision boundaries as far as it can from the training patterns. [11, 13, 16]

Consider a single ADALINE with two inputs as shown in fig2. The weight matrix W in this case has only one row. The input to the ADALINE is the vector $X = [X_0 X_1 X_2 ....X_n]^T$ where X_0 is the bias term and is set to 1. The ADALINE has a weight vector $W = [W_0 W_1 W_2 .....W_n]^T$ and its output, can be, simply written as

$$y = W^T X = W_0 + W_1 X_1 + ...W_n X_n \qquad (1)$$

The weight adjustment, or adaptation, is performed during the training process of the ADALINE using a nonlinear adaptation algorithm.

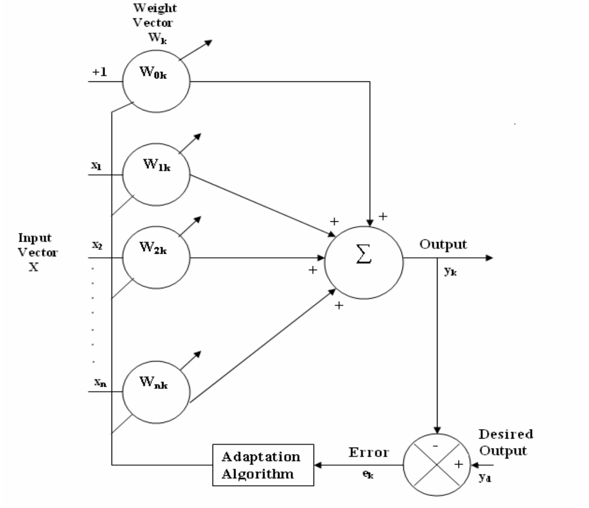

Fig. 2: ADALINE Network

The weight vector is updated using Widrow-Hoff delta rule [12]:

$$W(k+1) = W(k) + \alpha \left[\frac{e(k) * X(k)}{X^T(k) X(k)} \right] \qquad (2)$$

where k = time index of iteration,
$W(k)$ = weight vector at time k,
$X(k)$ = input vector at time k,
$e(k) = y_d(k) - y(k)$ =error at time k,
and α = learning parameter.

The ADALINE is used to estimate the time varying magnitudes of selected harmonic in a distorted waveform [13].Consider a distorted signal f (t) with the Fourier series expansion as

$$f(t) = \sum_{n=1}^{N} A_n \sin(n\omega t + \phi_n) \qquad (3)$$

where An and φn, are the amplitude and the phase angle of the harmonic, respectively, N is the total number of harmonics. The discrete-time representation of f(t) will be

$$f(k) = \sum_{n=1}^{N} \frac{A_n \cos\phi_n * \sin(2\pi nk)}{N_s} + \sum_{n=1}^{N} \frac{A_n \sin\phi_n * \cos(2\pi nk)}{N_s} \qquad (4)$$

where N_s = sampling rate = $\frac{F_s}{F_o}$, F_s = sampling Frequency, and F_o = nominal system frequency.

Fig 3.shows the proposed current adaline network. The input to the ADALINE input vector is chosen to be:

$$x(k) = \left[\frac{\sin(n\pi k)}{N_s} * \frac{\cos(n\pi k)}{N_s} \right]^T \qquad (5)$$

where n is the selected harmonic order, t (k) is the time and its desired output Yd (k) is set to be equal to the actual signal, f (k). The weight vector is set to be

$$Wo = [A_1 \cos\phi_1 A_1 \sin\phi_1 ....A_n \cos\phi_n A_n \sin\phi_n] \qquad (6)$$

The tap weight vector of the adaptive filter is denoted by $e(k) = y_d(k) - y(k)$ and perfect tracking is attained when the tracking error e (k) approaches zero. This optimum condition is realized when the estimation variance and the lag variance contribute equally to the mean square deviation. Therefore,

$$y(k) = y_d(k) = f(k) = W_o^{\ T} * x(k) \qquad (7)$$

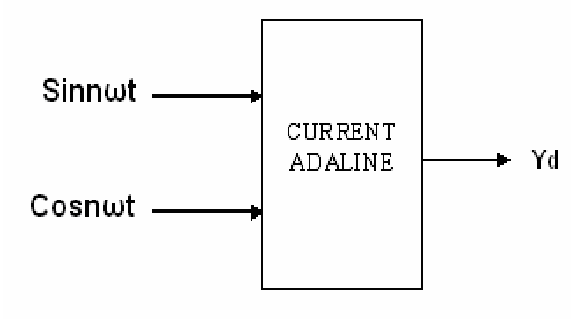

Fig. 3: Proposed Current ADALINE Network

IV. Operation Of The Proposed Scheme

The block diagram of the proposed power line conditioner using active power filter is shown in Fig.4. The proposed Modular Active power filter connected to the electric Distribution system. The line current signal is obtained and fed to an ADALINE which extracts the fundamental components of the line current signal. In the controller block, fundamental component is compared with distorted line current to generate modulating signal. This modulating signal is used to generate Pulse-Width Modulated (PWM) switching pattern for the switches of the active line conditioner module.[12][17] The output current of the active filter is injected into the power line. The injected current, equal-but opposite to the harmonic components to be eliminated. Harmonics are suppressed by connecting the active filter modules to the electric grid. The higher-order harmonics are taken care of by a passive low-pass filter[11]. Fig.5.shows the simulated block diagram of proposed ANN based active filter connected to the electric distribution system. Fig.5 consists of a single phase fully controlled converter feeding RL load, Active filter and its ANN based control circuit. Fig.6 shows the details of control block using ANN. In the control block an improved scheme is proposed in which only the actual load current is given to adaptive neural network and the reference current is obtained. The load voltage is given to a DC regulator with a simple PI controller which gives the actual filter current and which is compared with reference current the gating pulses to IGBTs are provided through a hysteresis band comparator.

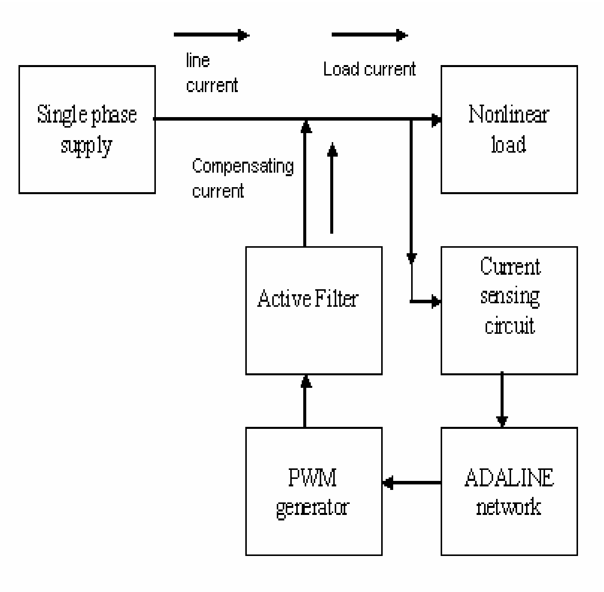

Fig. 4: Block Diagram of the Proposed Scheme

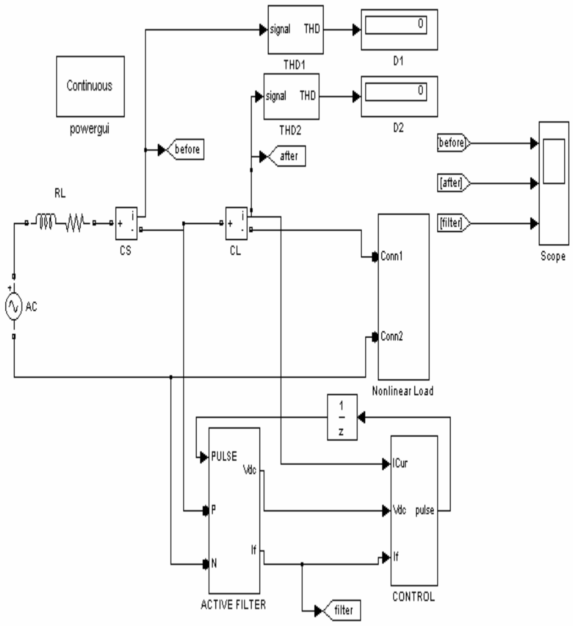

Fig. 5: Simulated circuit diagram of proposed ANN based active filter connected to non-linear load.

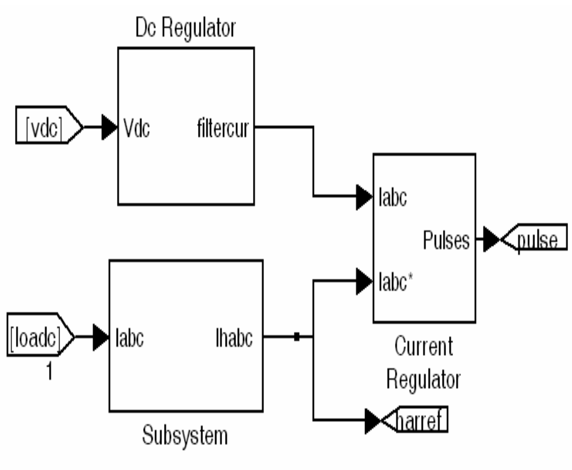

Fig. 6: Control block using ANN

V. SIMULATION RESULTS

The effectiveness of the proposed model is verified with a single phase fully controlled converter with the following parameters. Supply voltage = 220V, frequency=50Hz, load Resistance(R) = 153 Ω and load inductance(L) =0.328 H. The converter is tested with different firing angles. First the converter is operated with a firing angle of 18^o. Fig.7 shows the waveforms of the supply current, load current and filter current after the application of the proposed active power filter filter. Fig.8. and Fig.9 represent the harmonic spectrum of the supply current before and after the application of the proposed shunt active power filter respectively. The supply current waveform is improved and its THD is reduced to 2.14% from 16.32%.

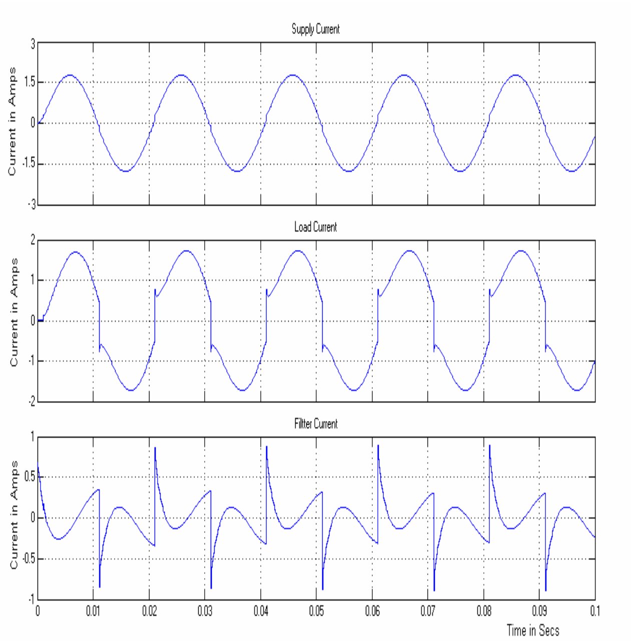

Fig. 7: Supply current, Load current and filter current waveforms of the converter (with filter for a firing angle of 18^o)

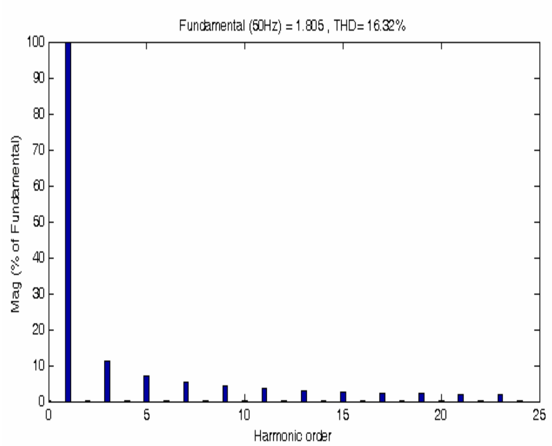

Fig. 8: Harmonic spectrum of the supply (Load) current (without filter for the firing angle of 18^o)

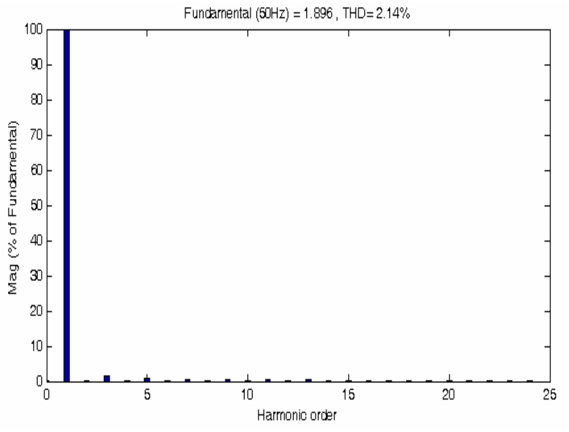

Fig. 9: Harmonic spectrum of the supply current (with filter for the firing angle of 18°)

In the second case the firing angle of the converter is varied to 36°. Fig.10 shows the waveforms of the supply current, load current and filter current after the application of the proposed active power filter. Fig.11. and Fig.12 represent the harmonic spectrum of the supply current before and after the application of the proposed shunt active power filter respectively. The supply current waveform is improved and its THD is reduced to 2.43% from 22.43%.

Finally the firing angle of the converter is varied to 54°. Fig.13 shows the waveforms of the supply current, load current and filter current after the application of the proposed active power filter. Fig.14. and Fig.15 represent the harmonic spectrum of the supply current before and after the application of the proposed shunt active power filter respectively. The supply current waveform is improved and its THD is reduced to 3.49% from 25.11%.

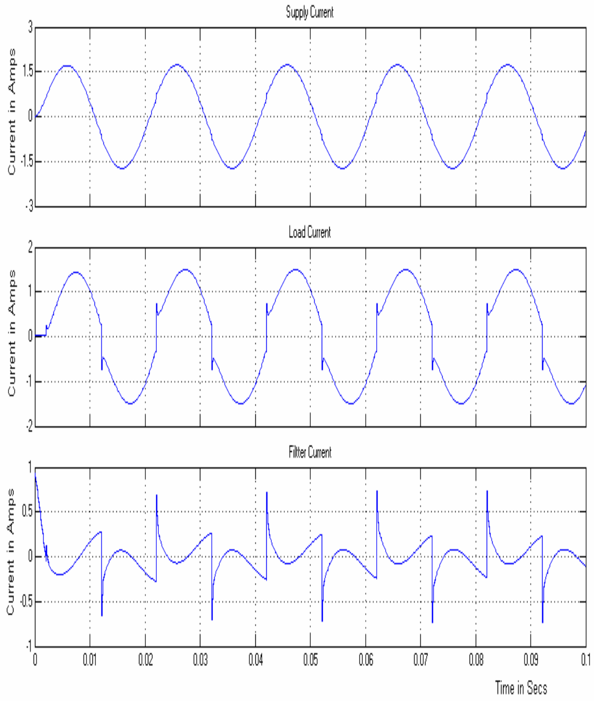

Fig. 10: Supply current, Load current and filter current waveforms of the converter (with filter for a firing angle of 36°)

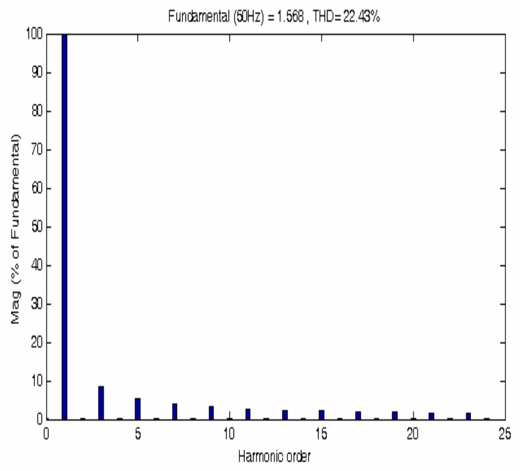

Fig. 11: Harmonic spectrum of the supply (Load) current (without filter for the firing angle of 36°)

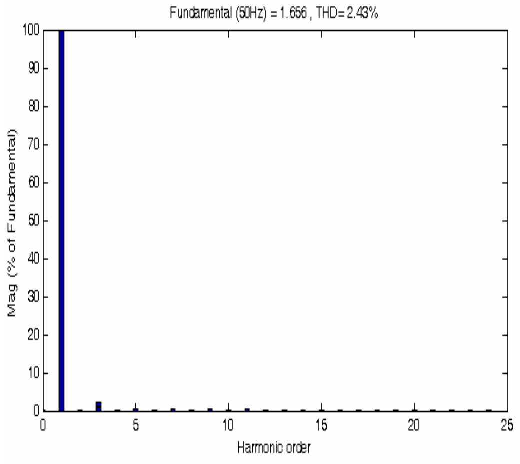

Fig. 12: Harmonic spectrum of the supply current (with filter for the firing angle of 36°)

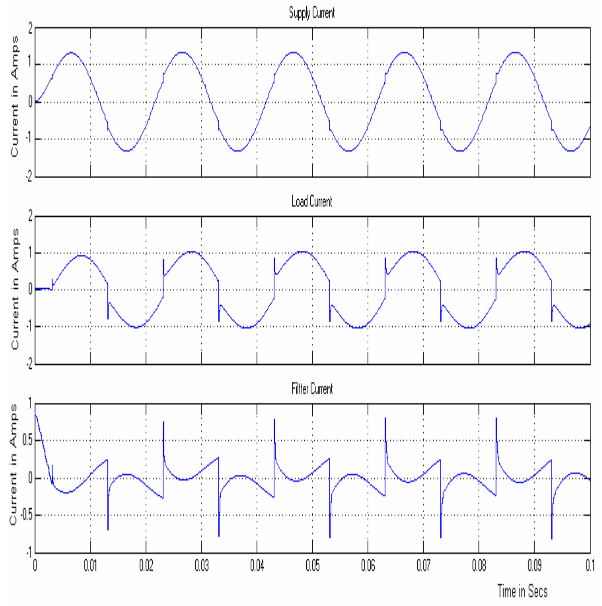

Fig. 13: Supply current, Load current and filter current waveforms of the converter (with filter for a firing angle of 54°)

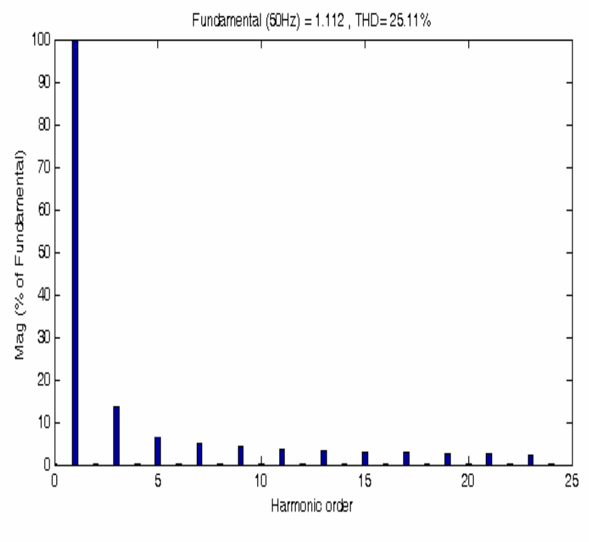

Fig. 14: Harmonic spectrum of the supply (Load) current (without filter for the firing angle of 54°)

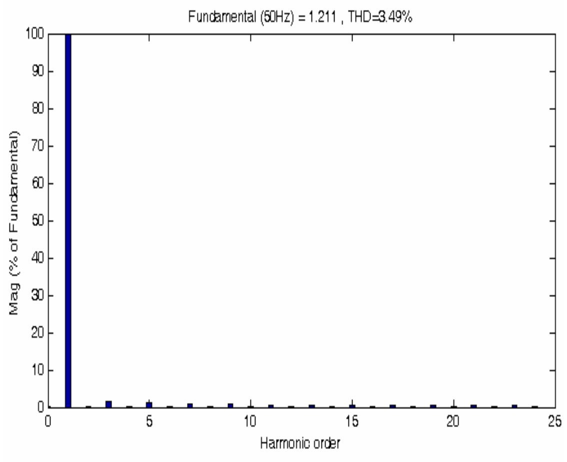

Fig. 15: Harmonic spectrum of the supply current (with filter for the firing angle of 54°)

The proposed shunt active power filter was also tested with different loads i.e by connecting a single phase half controlled converter parallel to the single phase fully controlled converter. The fully controlled converter is operated with the same load conditions with a firing angle of 18°. The half controlled converter is operated with a firing angle of 36° to supply a RL load (R=180Ω and L=1H). Fig.16 shows the waveforms of the total supply current, load current of fully controlled converter ,load current of half controlled converter, total load current and filter current after the application of the proposed active power filter. Fig.17. and Fig.18 represent the harmonic spectrum of the load (supply) current of the half controlled and fully controlled converter, before application of the proposed shunt active power filter respectively. The THD value for the supply current of half controlled converter is 23.55% and for that of fully controlled converter is about 16.53%. Fig.19. and Fig.20 represent the harmonic spectrum of the total supply current before and after the application of the proposed shunt active power filter respectively. So the supply current waveform is improved and its THD is reduced to 3.70% from 16.30%.

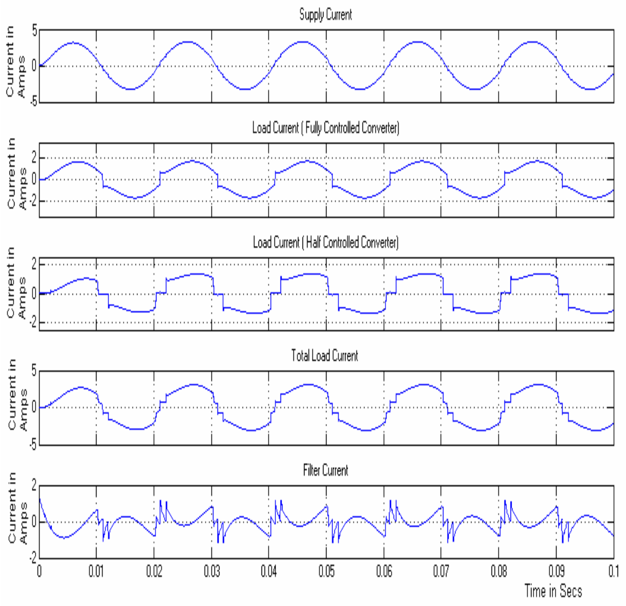

Fig. 16: Supply current, Load current and filter current waveforms of the parallel combination of half controlled and fully controlled converter

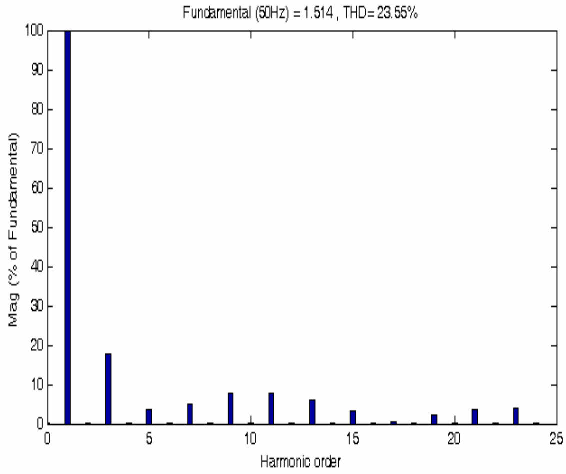

Fig. 17: Harmonic spectrum of the supply (Load) current of half controlled converter (without filter for the firing angle of 36°)

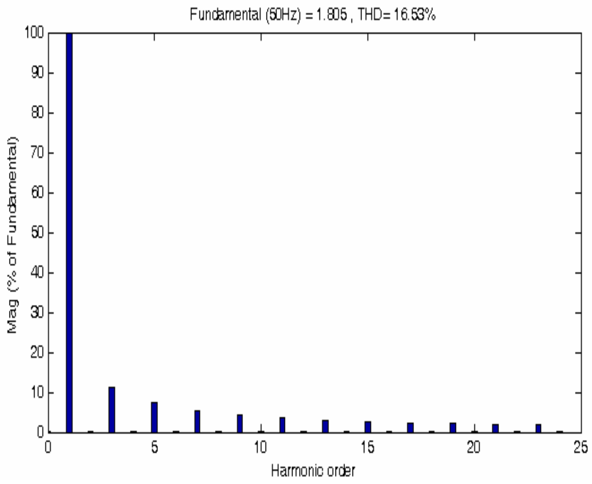

Fig. 18: Harmonic spectrum of the supply (Load) current of fully controlled converter (without filter for the firing angle of 18°)

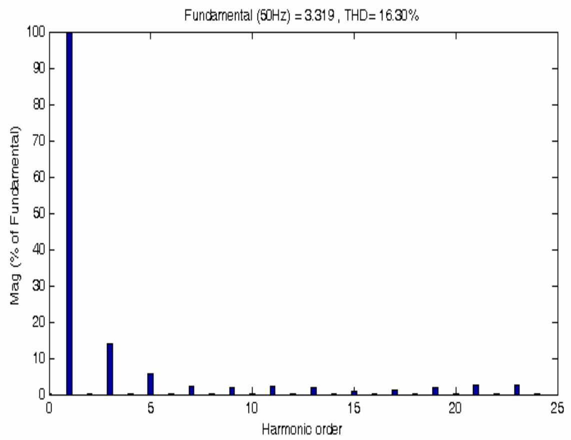

Fig.19:Harmonic spectrum of the total load current (without filter)

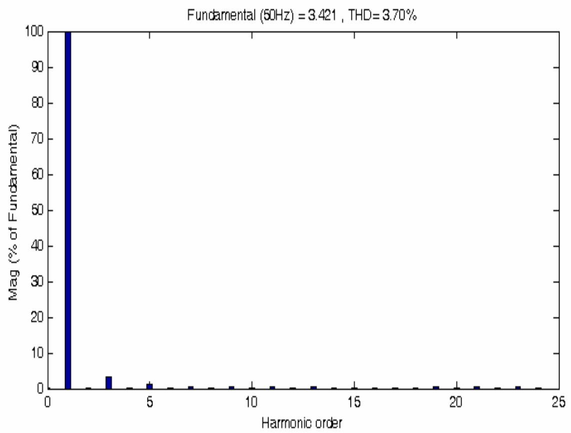

Fig.20:Harmonic spectrum of the total supply current (with filter)

VI. COMPARISON BETWEEN ANN AND FFT (BEFORE AND AFTER HARMONIC REDUCTION)

The most common frequency-domain harmonic analysis techniques are Fast Fourier transform (FFT) and Artificial Neural Network (ANN). In FFT method, the harmonic components are computed by implementing Fast Fourier Transform on digitized samples of a measured waveform in a time window. When the signal is distorted by noise and/or the decaying nature of the DC component, the harmonic extraction by FFT will lead to incorrect results. ADALINE has a better performance in terms of convergence speed and noise rejection compared with FFT for the dynamic systems with random noise. One of the common problems with FFT is the spectral leakage effect resulting from the deviation in fundamental frequency. A fundamental frequency offset of 0.4Hz produces an error of 10% in the amplitude of the 5th harmonic. To overcome this problem, a variety of numerical algorithms have been developed for frequency measurement, such as the zero crossing technique. This technique is simple and reliable but its performance has a cost ,i.e long measurement times (generally more than 3cycles of the fundamental) and this algorithm can cause computational error owing to rounding of errors.[18]. FFT may use zero crossing as an external algorithm to measure the fundamental frequency. Hence the performance of ANN is improved over FFT in both speed and accuracy. Table 1 describes the harmonic content of the individual harmonics up to 23rd harmonic for the firing angle of 36°. The THD supply current waveform is reduced to 3.84% from 22.43% after compensation in the FFT method, where as in the proposed neural network approach it further reduced to 2.43%. The same kind of table may be prepared for other firing angles also. From this, it may be concluded that ADALINE based Active power Filter gives better result than FFT and also it can be observed that the harmonic content is greatly reduced by the control scheme through the same.

Table 1 : Comparison of harmonic analysis by ANN network (For firing angle $\alpha = 36^o$)

Sl.No.	Harmonic Order	Before Compensation	After Compensation	
			Using FFT Method (%)	Using Neural Network (%)
1.	1	100.00	100.00	100.00
2.	3	18.36	3.12	1.93
3.	5	9.40	1.12	0.84
4.	7	5.94	0.90	0.71
5.	9	4.27	0.77	0.53
6.	11	2.42	0.38	0.46
7.	13	2.12	0.67	0.38
8.	15	2.02	0.76	0.32
9.	17	1.84	0.44	0.28
10.	19	1.72	0.47	0.23
11.	21	1.51	0.68	0.21
12.	23	1.31	0.53	0.19
THD		**22.43**	**3.84**	**2.43**

VII. CONCLUSION

The proposed neural network based shunt active power filter can compensate a highly distorted line current by creating and injecting appropriate compensation current. In the test cases simulated for different firing angles , the THD of the supply current is improved to less than 5% with the proposed shunt active power filter. In addition to this the simulation was carried out for the additional non linear loads (single phase half controlled converter) and the THD in the supply current is also improved to less than 5%. The performances reached by the proposed method are better than those obtained by more traditional techniques as mentioned in the introduction. It enhances the reliability of active filter. The overall switching losses are minimized due to selected harmonic elimination. Speed and accuracy of ADALINE results in improved performance of the Active Power Filter. Finally the harmonic content analyzed by artificial neural network (ANN) is compared with the Fast Fourier Transform (FFT) and it shows ANN gives accurate result than FFT, because of its speed and accuracy. In future it is planned to implement the hardware model of the Shunt Active Power Filter using DSP based controller.

ACKNOWLEDGEMENT

The authors wish to express their sincere thanks to the respectable reviewers for providing valuable suggestions to improve the quality of the paper.

APPENDIX

MATLAB CODE FOR ANN

```
clc;
function Y = bb(loadcurrt)
N=1;newW= rand(2*N);
delw= 0;e=rand(2*N);
error=0.2;alpha=0.005;
num=0;dina=0;out=0;Ts=10e-5;
f=50;phase_degree=90;w=0;
M=0;max=2*pi;Wt=0;
phase_rad=phase_degree*pi/180;
sines= fopen('E:\Tsine.dat','r');
cosines=fscanf(sines,'%g');
fclose(sines);
format long;
cosines=cosines+Ts;
Ts=cosines;
sines= fopen('E:\Tsine.dat','w');
fprintf(sines,'%g',cosines);
fclose(sines);
w=f*Ts*2*pi;
w=w+phase_rad;
M=mod(w,max);
wt=M;
for n=1:N
c(n)=(cos((2*n-1)*wt))/(2*n-1);
s(n)=sin((2*n-1)*wt)/(2*n-1);
x(2*n-1)=c(n);
x(2*n)=s(n);
y(2*n-1)=0.5*((1-exp(-alpha*c(n)))/(1+exp(-
alpha*c(n))))+0.5*c(n);
y(2*n)=0.5*((1-exp(-alpha*s(n)))/(1+exp(-
alpha*s(n))))+0.5*s(n);
end
for n=1:2*N
dina=dina+x(n)*y(n);
end
weight= fopen('E:\tst.dat','r');
W=fscanf(weight,'%f');
fclose(weight);
E= fopen('E:\eror.dat','r');
error=fscanf(E,'%f');
fclose(E);
for n=1:2*N
out=out+x(n)*W(n);
delw=(alpha*error*y(n))/dina;
W(n)=W(n)+delw;
end
error=loadcurrt-out;
E= fopen('E:\eror.dat','w');
fprintf(E,'%f',error);
fclose(E);
weight= fopen('E:\tst.dat','w');
fprintf(weight,'% f',W);
fclose(weight);
Y=error;
```

REFERENCES

[1] Alali,M.A.E, Saadate.S, Chapuis.Y.A, and Braun.F, “Control and analysis of series and shunt active filters with SABER.” International Power Electronics Conference (IPEC'2000), April3-7, Tokyo, Japan, 2000, pp. 1467-1472.

[2] Bird.B.M, Marsh.J.F and McLellan.P.R, “Harmonic reduction in multiple converters by triple-frequency current injection,” IEE Proc., vol. 116, no. 10, pp. 1730–1734, 1969.

[3] Arnetani.A, et.al, A"Harmonic Reduction in ac-dc Converters by Harmonic Current Injection," Proc. IEE, 119, July 1972, pp. 857-864.

[4] Gyugyi.L and Strycula.E.C, "Active AC Power Filters," IEEE Industrial applications Society Annual Meeting, 1976 pp. 529-535.

[5] Akagi.H, Kanazawa.Y and Nabae.A, "Instantaneous Reactive Power Compensators Comprising Switching Devices without Energy Storage Components," IEEE Trans. Industry Applications, 20(3), May/June 1984, pp. 625-630.

[6] Soliman.S.A, El-Naggar.K, and Al-Kandari, “Kalman filtering based algorithm for low frequency power systems sub harmonics identification,” International Journal of Power and Energy Systems, Vol. 17, No. 1, 1997.

[7] Chan.Y.T and Plant.J.B, “A parameter estimation approach to estimation of frequencies of sinusoids,” IEEE Transactions on Acoustics, speech, signal processing Vol. 29, No. 2, April 1981, pp. 214-219 .

[8] El-adany.E.F, Elshatshat.R, Salama.M.M.A, and Kazerani.M, and A.Y.Chikhani, “Reactance one-port compensator and modular active filter for voltage and current harmonic reduction in non-linear distribution systems: A comparative study,” Electric Power Systems Research, Vol. 52, 1999, pp. 197-209.

[9] Pecharanin.N, Sone.M and Mitsui.H,“An application of neural network for harmonic detection in active filter” in proceedings of IEEE International Conference on Neural Networks, Vol. 6, July 1994, pp. 3756-3760.

[10] Hartana.K, and Richards.G.G, “Harmonic source monitoring and identification using neural networks", IEEE Trans. on Power Systems, Vol. 5, No. 4, NOV. 1990, pp. 1098-1 104.

[11] Dash.P.K, Swain.O.P, Liew.A.C and Rahman.S , "An adaptive linear combiner for on-line tracking of power system harmonics" IEEE Trans. on Power Systems, Vol. 11, No. 4, Nov. 1996, pp. 1730-1735.

[12] Vazquez.J.R, Salmeron.P.R, “Active power filter control using neural network technologies” IEE proceedings on Electrical Power Applications, Vol. 150, No2 March 2003, pp 139-145.

[13] Ould Abdeslam.D, Mercklé.J, Ngwanyi.R and Chapuis.Y.A, “Artificial Neural Networks for Harmonic Estimation in Low-Voltage Power Systems”, Fourth International ICSC Symposium on Engineering of Intelligent Systems (EIS 2004), Island of Madeira, Portugal, 2004.

[14] Widrow.B, Lehr.M.A, “30 years of adaptive neural networks: Perceptron, Madaline and Back propagation”, proceedings of the IEEE, Vol. 78, No.9, Sep, 1990, pp. 1415-1442.

[15] Bruyant.N, Machmoum.M and Chevrel.P, “Control of a three-phase active power filter with optimized design of the energy storage capacitor”, PESC'98, Vol.13, May17-22, Fukuoka,Japan, 1998, pp. 878-88.

[16] Vazquez.J.R. and Salmeron.P.R “Three Phase Active Power Filter Control Using Neural Networks” 10th Meditterranean Electrotechnical Conference, Vol III, MElecon 2000, pp. 924-927.

[17] Rukonuzzaman.M and Mutsuo Nakaoka, “Single phase shunt active power filter with knowledge based harmonic detection algorithm”, PCC –Osaka 2002 pp. 778-783.

[18] Girgis.A.A and Ham.F, “A quantitative Study of Pitfalls in FFT”, IEEE Trans. on Aerosp. Electron. Syst., Vol. 16, No. 4, 1980, pp. 434-439.

BIOGRAPHIES

E.Chandra Sekeran received B.E Degree in Electrical and Electronics Engineering from PSG College of Technology in the year 1990 and M.E (Applied Electronics) from Bharathiar University in 1999. Currently he is pursuing Ph.D research work in the area of Power Quality under the guidance of Dr.P.Anbalagan. He is a senior grade lecturer of EEE department in Coimbatore Institute of Technology. He is having a 2 years of industrial and 12 years in teaching experience. He has published 32 technical papers in national /international conferences and journals. He is Life Member in Indian Society for Technical Education (India). His special fields of interest are Power electronics and Electric drives and control.

Dr. P.Anbalagan received B.E. Degree in Electrical and Electronics Engineering from Government College of Technology in the year 1973 and M.Sc (Engg.) from Madras University in 1977. He obtained Ph.D from Bharathiar University in the area of Digital Protection of Power Systems in the year 1994. He is having a teaching experience of 24 years. He is currently Professor and Head of EEE department in Coimbatore Institute of Technology. He has published 111 technical papers in national /international conferences and journals. He is a fellow member IE (India) and senior member of IEEE. Life Member in Indian Society for Technical Education (India),Life Member in Systems Society of India, and Life Member in Council of Engineers (India). His special fields of interest are Digital protection of power systems and Embedded Systems.

A Mathematical Model for IGBT

Vineeta Agarwal

Abstract - A mathematical model has been developed for an IGBT by compartmenting it into two diodes, which are connected in series with reverse configuration. One diode is an ordinary diode while other is a controlled diode. The performance of the controlled diode depends upon the magnitude of gate emitter voltage and collector emitter voltage. A gate emitter voltage greater than gate emitter threshold voltage modulates the conductivity of controlled diode together with hole injection from the p+ base near the collector terminal. Parameters of these diodes are estimated by applying curve fitting tool and power invariance method. The validity of the model has been checked by a simulation example. The results of simulation show appreciable closeness with actual one.

Keywords - Insulated Gate Bipolar Transistor (IGBT), Gate Emitter Threshold Voltage, Collector Emitter Threshold Voltage, Conductivity Modulation, Gate Emitter, Collector Emitter

List of Symbols

a_o = *Coefficients(dimensionless)*
a_1 = *Coefficients* (V^{-1})
b = *Incremental wattage of IGBT which raises temperature by* 1^oC
C_{ix} = *Nonlinear capacitance between gate and emitter (Farad)*
C_C = *Shunt capacitance of diode* D_1 *(Farad)*
C_e = *Shunt capacitance of diode* D_2 *(Farad)*
i_C = *Collector current(ampere)*
I_{d1} = *Current source(ampere)*
$I_o(T)$ = *Reverse saturation current of diode* D_1 *at Temperature* T^o *K,(ampere)*
I_o = *Reverse saturation current of diode* D_1 *at Temperature* 0^o *K,(ampere)*
k = *Boltz mann constant, (Joule /*^oK*)*
m = *Modulation factor (dimensionless)*
M = *Mass of IGBT (gram)*
Q = *Electronic Charge (coulomb)*
R_c = *Resistance of diode* D_1 *(ohm)*
r_e = *Variable resistance of diode* D_2 *(ohm)*
S = *Equivalent specific heat (joule/gm °C)*
T = *Temperature of the junction of diode D ,(*^oK*)*
V_g = *Gate emitter voltage (V)*
V_{d1} = *Constant voltage source (V)*
V_{d2} = *Variable voltage source (V)*
V_d = *Voltage between collector and emitter (V)*
V_{d1} = *Constant voltage source (V)*
V_{d2} = *Variable voltage source (V)*
V_d = *Voltage between collector and emitter (V)*
V_{GET} = *Gate emitter threshold voltage (V)*
V_{CET} = *Collector emitter threshold voltage (V)*
V^+ = *Potential at junction of two diodes (V)*
V_T = *kT/q, (V).*

I. INTRODUCTION

Ever since the evolution of IGBT a number of models have been reported in literature namely IG SPICE, PSPICE [1-3], analytical [4] and EMTP [5]. Most of them explain both steady state and dynamic behavior of IGBT with varying degree of accuracy. In utility related applications such as flexible ac transmission systems (FACTS) [6], requiring high power electronics, the system is generally described by means of differential/algebraic equations which are solved using any one of the several higher level computer languages such as FORTRAN, C, etc. For such cases the detailed model of the devices will result a large computation time, loss of accuracy and an overwhelming amount of information, which is difficult to digest [7-8]. In order to keep the execution time within reasonable limit, complex devices in power electronics system such as IGBT etc. may be represented by approximate models, which may be represented by standard algebraic equations [9-12]. An improved and simplified EMI modeling method considering the IGBT switching behavior model has been proposed in [13] where device turn-on and turn-off dynamics are investigated by dividing the nonlinear transition by several stages.

This paper proposes a simple mathematical model of IGBT, consisting of only diodes that are described by well-known algebraic equations. The model is illustrated with controlled diode characteristics whose performance depends on a modulation factor *m*, which is function of the voltages applied at different points across the device. The parameters of this model are obtained by applying power invariance [14] and curve fitting technique [15]. The model is tested for an existing IGBT in the lab extracting the required data from the instruction sheet.

II. PROPOSED MODEL

Fig. 1 shows the basic architecture of an IGBT. It is compartmented into two parts by segmenting with dotted lines as shown near the junction J_1 in *n-* base region. By inspection, the part of IGBT, between the dotted line and collector terminal forms a *p-n* junction diode D_1.

The remaining part of IGBT, which accommodates the gate and emitter, can be viewed as a controlled diode, D_2.

The paper first received 22 Sept. 2006 and in revised form 31 Mar 2007.
Digital ref. AI70201139
Department of Electrical Engineering, MNNIT, India
Allahabad, 211004, India, Email: vineeta@mnnit.ac.in

Between the junction of two diodes and gate terminal, a parallel combination of RC circuit of constant values is added. This RC circuit is attributed because of the insulation resistance and capacitance of SiO_2 layer underlying the gate terminal. A non-linear capacitance C_{ix}, between gate and emitter is also added which gives intermediate circuit of IGBT as shown in Fig. 2.

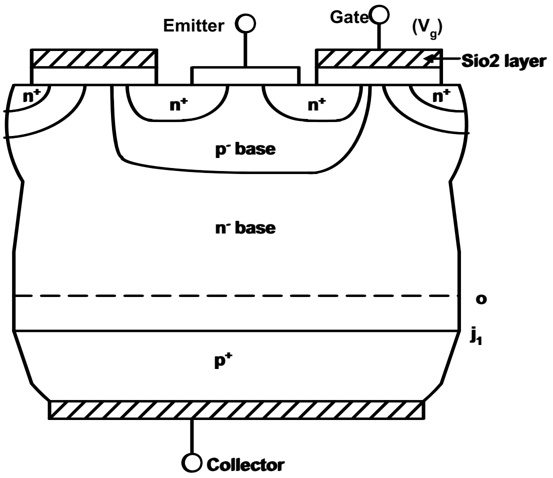

Fig. 1: Basic Construction of IGBT

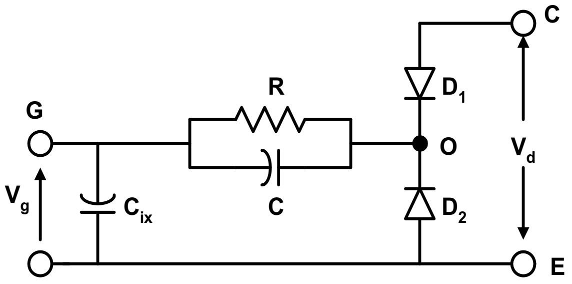

Fig. 2: Inter-mediate circuit of IGBT

The final model can be obtained by replacing the diodes by their equivalent circuit as shown in Fig. 3.

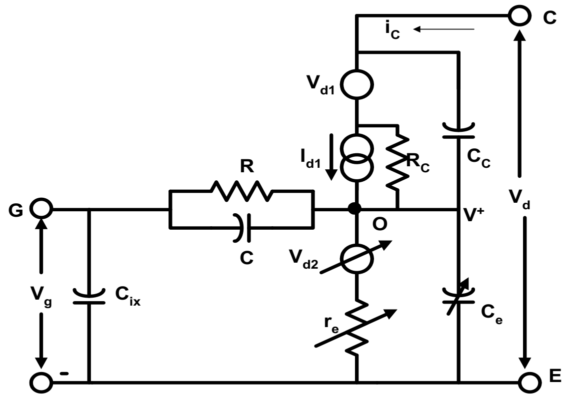

Fig. 3: Steady- State Model of IGBT

In this model, the ordinary diode has been replaced by a constant voltage source V_{d1} in series with a parallel combination of a current source, I_{d1}, a resistance R_c and a shunt capacitance C_C. The controlled diode is modeled as a variable capacitance C_e in parallel to a series combination of variable voltage source V_{d2} and resistance r_e.

At low frequencies all these capacitances become open circuit and the resultant circuit becomes the steady state DC model of IGBT as shown in Fig. 4.

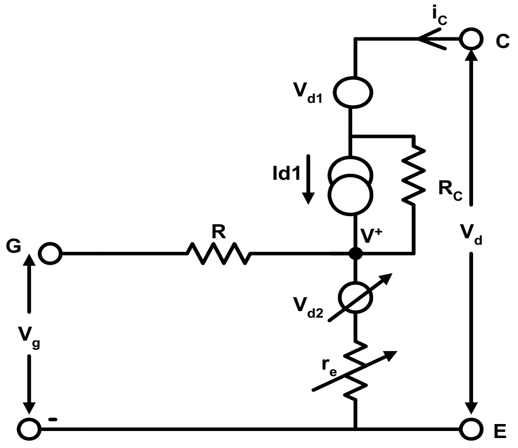

Fig .4: DC Model of IGBT

III. PARAMETER IDENTIFICATION

In order to identify the parameters of the proposed model, two strategies are resorted: 1) the principle of invariance of power in the components and 2) mathematical tool of curve fitting. Let a positive voltage V_d is applied at collector with respect to emitter. Also a voltage $V_g > V_{GET}$ is applied at gate terminal.

If V_+ is the potential of point 'o' which is junction of two diodes then the voltage $V_d - V_+$ will appear across the diode D_1. If i_C is the current flowing through the circuit, then the voltage-current relation of diode D_1 can be expressed as,

$$i_C = I_o(T)\{e^{\frac{V_d - V_+ - V_{d1}}{V_T}} - 1\} \tag{1}$$

Rearrangement of equation (1), gives,

$$V_d - V_+ = V_{d1} + (kT/q)\ ln\ [1 + i_C/I_o(T)] \tag{2}$$

Differentiation of equation (2) with respect to i_C gives the resistance of the diode

$$R_C = \frac{d(V_d - V_+)}{d(i_C)} = \frac{kT}{q}(i_C + I_o(T)) \tag{3}$$

To identify the current source, principle of power invariance is applied to the diode D_1 and its equivalent. Power consumed by diode D_1 is given by,

$$(V_d - V_+)\ i_C = (V_{d1} + (kT/q)\ ln\ [1 + \frac{i_C}{I_o(T)}]\ i_C \tag{4}$$

and its equivalence is given by

$$(\ V_{d1} + r_C.i_C - r_C.I_{d1})\ i_C \tag{5}$$

Power invariance requires

$$(V_{d1}+ \frac{kT}{q}) \ln [1 + \frac{i_C}{I_o(T)}]\, i_C$$

$$= (V_{d1} + R_C.i_C - R_C I_{d1})\, i_C \tag{6}$$

Above equality should hold for all value of i_C This implies that differentiation of (6) for both side with respect to i_C does not affect the equality or

$$\frac{d}{d(i_C)}\left(\frac{kT}{q}\ln(1+\frac{i_C}{I_o(T)})i_C\right) =$$

$$\frac{d}{d(i_C)}\left((R_C i_C - R_C I_{d1}))i_C\right) \tag{7}$$

Substituting the value of R_C and dR_C/di_C in equation (7) and simplifying it gives

$$\frac{d}{d(i_C)} + \frac{I_{d1}}{i_C} - \frac{I_{d1}}{i_C + I_0(T)} =$$

$$1 - \frac{I_{d1}}{i_C + I_0(T)} - (1+\frac{I_0(T)}{i_C}) \ln (1+\frac{i_C}{I_0(T)}) \tag{8}$$

or $I_{d1} = i_C - (i_C + I_o(T)) \ln (1+\frac{i_C}{I_0(T)})$ (9)

In order to investigate the mathematical description of controlled diode D_2 a functional relationship between i_C, V_g and V_d is required. Since IGBT model has been approximated to consist of mainly diodes, therefore, it is appropriate to describe collector emitter voltage drop equal to product of ordinary diode voltage drop multiplied by a modulating factor m which should of course be function of collector emitter voltage and gate emitter voltage. Thus, overall, IGBT can be described with a modified diode characteristics as given below

$$V_d = m(V_g, V_d)\, V_T \ln (1+\frac{i_C}{I_0(T)}) + V_{CET} \tag{10}$$

Thermo-dynamic equation governing the temperature [16] of IGBT is given by

$$M.S. \frac{dT}{dt} + b(T- T_0) = V_d\, i_C \tag{11}$$

For steady state analysis $\frac{dT}{dt}$ = 0 therefore from (11)

$$T = T_0 + \frac{V_d i_C}{b} \tag{12}$$

Substituting the value of T in (10) and rearranging the terms we get

$$V_d = \frac{\frac{mkT_o}{q}\ln\left(1+\frac{i_C}{I_o}\right)+V_{CET}}{1-\left(\frac{mki_C}{qb}\right)\log\left(1+\frac{i_C}{I_o}\right)} \tag{13}$$

From (13) it is clear that for very large value of V_d, denominator of equation (13) approaches to zero. This implies that

$$m\,(V_g) = \frac{bq}{ki_C \log\left(1+\frac{i_C}{I_o(T)}\right)} \tag{14}$$

Equation (14) reveals that m becomes sole function of V_g for large value of V_d**.** That is what IGBT characteristics shows at higher value of V_d. From equation (13), m can be written as follows:

$$m(V_g, V_d) = \frac{V_d - V_{CET}}{\left(\frac{kV_d i_C}{qb}+\frac{kT_o}{q}\right)\log\left(1+\frac{i_C}{I_o(T)}\right)} \tag{15}$$

Basically IGBT is dual input single output device. The input ordered pair (V_g, V_d) corresponds to the output i_C. Thus equation (15) transforms above mentioned correspondence into (V_g, V_d) and $m\,(V_g, V_d)$.

IV. MODEL VALIDATION

To identify m as function of (V_g, V_d) a table is generated from the characteristics sheet of IGBT [1] by extracting the data required for the model. For 4 distinct values of V_g and 7 distinct values of V_d the value of m is calculated from the equation (15) knowing corresponding value of i_C. This covers almost all the operating range of IGBT. Table 1 is thus obtained which gives the different parameter of IGBT. From this table it is observed that as the value of V_d is increased, m increases correspondingly whereas for an increase of V_g, m decreases. To obtain exact relation between m and V_d for a given value of V_g, the method of least square curve fitting is used. Let m be approximated by one-dimensional polynomial given by equation (16)

$$m = a_o + a_1 V_d \tag{16}$$

Then, for V_g equal to 7, the coefficients a_o and a_1 will be calculated as -0.714 and 1.115 respectively and the above polynomial will be given by equation (17)

$$m = 1.115\, V_d - 0.714 \tag{17}$$

Similarly, for V_g equal to 8, 9 and 10 the above polynomial may be written, respectively, as

$$m = 0.852\, V_d - 0.526 \tag{18}$$

$$m = 0.502\, V_d + 1.098 \tag{19}$$

$$m = 0.346\, V_d + 1.3748 \tag{20}$$

The coefficients a_o and a_1 are plotted in Fig. 5 for different values of V_g. It is observed that if these points are joined together it will result a straight line, which can be extended on both axis. These lines will provide the value of coefficients a_o and a_1 for any other value of V_g not calculated in the above equations.

Now if the value of a_o and a_1 are known for a specified value of V_g, then the value of m may be calculated for a specified value of V_d and V_g using (16). Once the value of m is known, the current i_C is directly calculated from (13).

Table 1: Various Parameters of IGBT

	V_d =1.0	V_d =2.0	V_d = 4.0	V_d = 6.0	V_d = 8.0	V_d =10.0	V_d =20.0
V_g =7	i_C= 0.5 m=0.392	i_C= 2 m=1.633	i_C= 3.33 m=4.056	i_C= 3.33 m=4.456	i_C= 3.33 m=8.794	i_C= 3.33 m=11.069	i_C= 3.33 m=21.497
V_g =8	i_C= 0.9 m=0.385	i_C= 5.5 m=1.58	i_C= 12.2 m=3.677	i_C=12.2mm = 5.58	i_C= 12.2 m=7.31	i_C= 12.2 m=8.87	i_C=12.2 m=14.84
V_g =9	i_C= 0.95 m=0.384	i_C= 6 m=1.57	i_C=16.4 m=3.45	i_C= 23.3 m=4.78	i_C= 25 m=5.89	i_C= 25 m=6.91	i_C= 25 m=10.27
V_g =10	i_C= 1 m=0.384	i_C= 6.25 m=1.57	i_C=20.8 m=3.34	i_C= 34.2 m=4.19	i_C= 39.6 m=4.83	i_C= 40.5 m=5.46	i_C=40.5 m=7.49

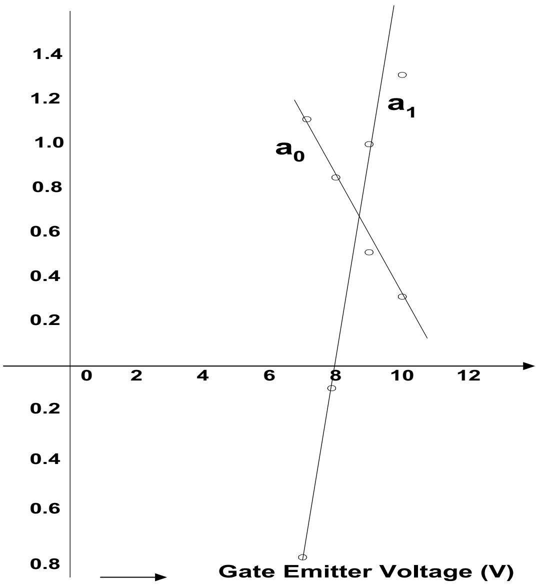

Fig. 5: Relation between V_g & a_o and V_g & a_1

The proposed model is compared with the models available in reference [9]. Table 2 shows the value of *m* calculated from (16) for a specified value of gate and collector voltage and compared with the value obtained in Table 1 for a known value of i_C. As data are extracted from the characteristics sheet of IGBT, therefore it is inevitable that there is an error due to scaling factor and other manual factor. The results are appreciably close in the face of this avoidable error.

V. CONCLUSIONS

A simple model for an IGBT has been developed which consists of only two diodes. One diode is an ordinary diode D_1 and other diode is a controlled diode D_2. The characteristics of IGBT have been approximated as modified diode characteristics, where the total voltage drop across collector and emitter is equal to the product of an ordinary diode voltage drop and a modulating factor m.

This modulating factor, *m*, has been established as the function of collector emitter voltage and gate emitter voltage. A one-dimensional polynomial approximation has been used to identify the value of modulating factor, m. In order to identify the modulating factor and in turn the circuit parameters, power invariance and curve-fitting technique has been used. For curve fitting technique, data are extracted from the data sheet of IGBT available in lab. The value of modulating factor obtained from the polynomial and that extracted from the data sheet are in closed agreement. The proposed model is simple accurate and integrates the DC behavior into a single formula.

Table 2: Calculated value of modulating factor m

V_g	V_d	i_C	m	m (calculated)	Error%
7	4	3.33	4.05	4.0	3.16×10^{-4}
7	12	3.33	13.28	12.96	2.4
8	6	12.2	5.5751	5.571	6.4×10^{-4}
9	2	5.5	1.570	1.5702	-4×10^{-4}
10	20	40.0	7.49	7.4905	-4×10^{-4}
10	6	34.2	4.19727	4.1973	8.32×10^{-2}
11	8	47.7	4.3907	4.0446	7.88
12	6	45.0	3.744	3.4141	8.81

REFERENCES

[1] F. Mihalic, K. Jezenik, K. Krishan & Manfred Rentmister, "IGBT SPICE Model" IEEE Trans. On Industrial Electronics, Vol. 42, No.1, February 1995, pp. 98-105.

[2] A. Maxim, G, Maxim," A Novel Analog Behavioral IGBT SPICE Macro Model, 30th Annual IEEE Power Electronics Specialist Conference, IEEE PESC 99, Vol. 1 pp. 364-369

[3] S. C. Yaun, "Non Destructive parameters Extraction for IGBT SPICE Model and Compared with results", Solid State Electronics, Vol. 49, issue 2, January 2005,pp. 123-129.

[4] Allen R. Hefner, "Analytical Modeling of Device Circuit Interaction for the Power Insulated Gate Bipolar Transistor" IEEE Transaction on Industry Application, Vol. 26, No.6, November/December 1990, pp. 995-1005.

[5] Chuck Wong, "EMTP Modeling of IGBT Dynamic Performance for Power Dissipation Estimation", IEEE Trans. on Industry Application, Vol. 3, No.1, January/

February 1997, pp. 64 – 71.

[6] N.G Hingorani, “Flexible ac Transmission,” IEEE Spectrum, Vol.30, April 1993, pp 40-45.

[7] N. Mohan, W.P. Robbins, T.M. Undeland, R. Nilssen and Olve Mo, “Simulation of Power Electronics and Motion Control Systems-An Overview,” Proceeding of IEEE Vol. 82, No. 8, August 1994, pp. 1287-1302.

[8] V. J. Thottuvelil, D. Chin, and G.C Verghese, “Hierarchical approaches in modeling high power factor ac-dc converters,” IEEE Transaction on Power Electronics, Vol. 6, April 1991,pp. 179-187.

[9] Kuang Sheng, Barry W. Williams and Stephen J. Finney, “A Review of IGBT Models”, IEEE Transaction on Power Electronics, Vol. 15, No. 6, November 2000, pp. 1250-1266.

[10] F. Charfi, M Ben Messaoud, B. Francois, K. Al Haddad and F. Sellami,, “IGBT Modeling Based on state graph Representation”, Proceedings 353 of Modelling and Simulation, 2002, pp. 70-74.

[11] S. EI Baroudi, S.D. Bocus, A. Berthon, “New Approach in IGBT Modeling for Power Circuit Simulation”, International Journal of Power and Energy Systems, Vol. 19, No.2, 1999, pp.107-114.

[12] A. R. Hefiner, Jr. S. Bouche, “Automated Parameter Extraction Software for Advanced IGBT Modeling” 7th Workshop on Computers in Power Electronics, 2000 COMPEL, 2000, pp. 10-18.

[13] Meng Jin; Ma Weiming; “Power converter EMI analysis including IGBT nonlinear switching transient model, Proceedings of IEEE International Symposium on Industrial Electronics, ISIE 2005,Vol. 2, 2005, Dubrovnik, Croatia, 20-23 June, pp. 499 – 504.

[14] de.I.M. Silva, N. K. Shrestha, F. Udrea, G.A.J. Amaratunga, D. Chamund, L. Coulbeck, P. Waind, “Accurate Conduction and Switching loss Models of IGBTs for Resonant Converter Design” 35th Annual IEEE Power Electronics Specialists Conference,Vol.4, Aachen, Germany, 2004, pp. 2950- 2955.

[15] S. S. Sastry, “Introductory Methods of Numerical Analysis”, Prentice-Hall of India Pvt. Ltd, New Delhi, 2002

[16] B. Lu, and J.L. Hudgins, and A.T. Bryant, A.T. and E. Santi, and P.R.Palmer, “Expanded thermal model for IGBT modules” IEEE Industry Applications Conference, 8-12 Tampa, FL, USA, Oct 2006, pp. 777-784.

BIOGRAPHY

Vineeta Agrawal has graduated from Allahabad University, India, in 1980, and received Master’s degree in Electrical Engineering in 1984, from the same university. She joined as lecturer in 1982 in Electrical Engineering Department in M. N. R. Engineering College. During teaching, she did her Ph.D. course in Power Electronics.

At present she is Professor and Head of Department of Electrical Engineering at Moti Lal Nehru National Institute of Technology, Allahabad. She has taught numerous courses in Electrical and Electronics. Her research interests are in single phase to three-phase conversion and AC drives. She has a number of publications in Journals and Conferences in her field. She has attended both National and International Conferences and presented papers there.

Asian Power Electronics Journal, Vol. 2, No. 1, Apr 2008

Parameter Identification Scheme for Induction Motors Using Output Inter-Sampling Approach

Masaru Hasegawa[1], Daisuke Ogawa[1] and Keiju Matsui[1]

Abstract –This paper shows a parameter identification scheme for speed sensorless vector controlled induction motor using output inter-sampling approach and experimentally evaluates this method. It is well known that both the rotor speed and the rotor time-constant of induction motors cannot be identified under steady state operation. This is because vector control system of induction motors consists of a closed loop system, in which *d* axis current is always kept constant under steady state operation. In this paper, a novel signal processing method, output inter-sampling approach, is employed from the viewpoint of the amplitude of high frequency signal injection to realize accurate parameter identification. This paper describes an identification strategy based on output inter-sampling approach and robust estimation method of the *d* axis using adaptive observer with robust observer design, and finally accuracy of parameter identification is experimentally evaluated using 1.5kW test induction motor.

Keywords - Induction Motor, Parameter Identification, Output Inter-Sampling Approach

I. INTRODUCTION

Induction motors have widely been used for traffic machines, in industrial fields, and so on. Especially, speed sensorless vector controlled induction motor is superior to any other electrical motors in terms of cost, robustness, and its performance is still being improved.

Generally, the mathematical model of the induction motor necessitates in order to construct the control system, which means that all parameters should be identified in advance or in real-time. Especially, some of parameters need to be identified in on-line since the dynamics of the induction motor might change because of parameter perturbation, which is caused by temperature variation or load condition, and speed variation. This parameter identification problem of the vector controlled induction motor had been attractive for many researchers. Shinnaka has proved, however, that the simultaneous identification of both rotor speed and rotor time constant is impossible in continuous time domain [1]. This is because some current control loops are often constructed in vector control system of induction motors, in which d axis current is always kept constant in steady state operation.

In order to avoid this problem, many researches have already proposed some kinds of strategies such as high frequency signal injection to obtain the parameter knowledge from only stator quantities, which would cause the torque vibration and the degradation of efficiency unfortunately [2][3][4]. In addition, a method of utilizing the transitional d axis estimation error, which is appeared just when the rotor speed changes of the induction motor, have been proposed so far [5]. Consequently, simultaneous identification at steady state is impossible without high frequency signal injection, and is still remains as an open problem in continuous time domain.

For parameter identification, it is desirable to decrease the amplitude of the injected signal, but there exists few methods to minimize the amplitude of this unnecessary signal to control induction motors. In recent years, the closed-loop identification is becoming one of the most interesting problems among researchers in control theory field, which means that the identification of the input-output characteristics of the plant with feedback controllers. One of the difficulties on the closed-loop identification is known that all of the parameter knowledge cannot be obtained from input quantities (stator voltages) and the plant output (stator current) because some variables (e.g. d-axis current) are kept constant in steady state operation, which results in that some of parameters to be identified are not excited. In this problem (closed-loop identification), Sano et al. have proposed 'Output Inter-Sampling Approach' to realize closed-loop identification [6]. According to this literature, this approach makes it possible to relax necessary condition of the closed-loop identification. Even although this approach necessitates high frequency signal injection, this literature concludes that it is possible to reduce the amplitude of this unnecessary signal for plant control [7].

This paper proposes an appropriate strategy to apply 'Output Inter-Sampling Approach' for identification of speed sensorless vector controlled induction motor in steady state operation. Based on 'Output Inter-Sampling Approach' technique, this paper will firstly discuss simultaneous identification problem in discontinuous time domain, in which 'Output Inter-Sampling Approach' is utilized to identify the PWM inverter fed induction motor under speed sensorless vector control. Although an exogenous signal is also injected in this paper, reduction of the amplitude of this injected signal can be expected by using output inter-sampling approach.

This paper is organized as follows: Firstly, the identification model of the induction motor is defined in section II. Next, output inter-sampling approach is introduced for identification of vector controlled induction motor in section III, and a design of an adaptive observer is described, which can reduce phase estimation error of rotor flux in section IV. This becomes necessary condition for accurate d-axis model identification. Finally, some

---

The paper first received 11 Nov. 2006 and in revised form 17 Mar 2008.
Digital ref: AI70201142

[1] Department of Electrical Engineering, Chubu University, Japan
E-mail: mhasega@isc.chubu.ac.jp

identification experiments are carried out, and the feasibility and the effectiveness of the proposed strategy are shown in Section V. Section VI describes the conclusions of this paper.

II. IDENTIFICATION MODEL OF INDUCTION MOTOR

This section defines the identification model of an induction motor. It should be noted that this model must not include rotor speed knowledge because this paper aims to identify parameters under speed sensorless vector control.

The state equation of the induction motor in a rotational reference frame (*d*-*q* axis) aligned with the rotor flux direction is expressed by

$$\frac{d}{dt}\begin{bmatrix} i_{ds} \\ i_{qs} \\ \lambda_{dr} \\ \lambda_{qr} \end{bmatrix} = \begin{bmatrix} -\frac{R_s+M^2R_r/L_r^2}{\sigma L_s} & \omega & \frac{MR_r}{\sigma L_s L_r^2} & \frac{\omega_r M}{\sigma L_s L_r} \\ -\omega & -\frac{R_s+M^2R_r/L_r^2}{\sigma L_s} & -\frac{\omega_r M}{\sigma L_s L_r} & \frac{MR_r}{\sigma L_s L_r^2} \\ \frac{MR_r}{L_r} & 0 & -\frac{R_r}{L_r} & \omega-\omega_r \\ 0 & \frac{MR_r}{L_r} & -(\omega-\omega_r) & -\frac{R_r}{L_r} \end{bmatrix} \begin{bmatrix} i_{ds} \\ i_{qs} \\ \lambda_{dr} \\ \lambda_{qr} \end{bmatrix} + \frac{1}{\sigma L_s}\begin{bmatrix} v_{ds} \\ v_{qs} \\ 0 \\ 0 \end{bmatrix} \quad (1)$$

where

v_{ds}, v_{qs} : stator voltages on *d*-*q* axis

i_{ds}, i_{qs} : stator currents on *d*-*q* axis

λ_{dr}, λ_{qr} : rotor flux on *d*-*q* axis

R_s, R_r : stator and rotor resistances

L_s, L_r : stator and rotor inductances

M : mutual inductance

ω_r : angular speed of rotor in electrical angle

ω : angular frequency of rotational reference frame *d*-*q* axis

$\sigma = 1 - M^2 / L_s L_r$: total leakage coefficient

In this paper, the direction of the actual rotor flux can be assumed to be aligned with that of the estimated flux by using an adaptive observer with a robust gain design, rotor flux can be regarded as $\lambda_{dr} = |\lambda_r|,\ \lambda_{qr} = 0$, respectively. Therefore, (1) is rewritten by the following equation:

$$\frac{d}{dt}\begin{bmatrix} i_{ds} \\ i_{qs} \\ |\lambda_r| \end{bmatrix} = \begin{bmatrix} a & \omega & c \\ -\omega & a & -\frac{\omega_r M}{\sigma L_s L_r} \\ b & 0 & e \end{bmatrix}\begin{bmatrix} i_{ds} \\ i_{qs} \\ |\lambda_r| \end{bmatrix} + g\begin{bmatrix} v_{ds} \\ v_{qs} \\ 0 \end{bmatrix} \quad (2)$$

in which

$$a = -\frac{R_s + M^2R_r/L_r^2}{\sigma L_s}, \quad b = \frac{MR_r}{L_r},$$
$$c = \frac{MR_r}{\sigma L_s L_r^2}, \quad e = -\frac{R_r}{L_r}, \quad g = \frac{1}{\sigma L_s}.$$

This induction motor model is then digitized with sampling time *T* from the first row in (2) and the third one as following:

$$\begin{aligned} i_{ds}[k+1] &= (1+aT)i_{ds}[k] + \frac{cbT^2z^{-1}}{1-(1+eT)z^{-1}}i_{ds}[k] \\ &\quad +\omega T i_{qs}[k] + gTv_{ds}[k]\ , \\ &= \frac{(1+aT)-(1+(a+e)T-(ae-bc)T^2)z^{-1}}{1+(-1-eT)z^{-1}}i_{ds}[k] \\ &\quad +\omega T i_{qs}[k] + gTv_{ds}[k]\ , \end{aligned} \quad (3)$$

and $(ae-be)T^2$ is neglectable in this equation, the following equation can be obtained:

$$i_{ds}[k] = \frac{gTz^{-1} - gT(1+eT)z^{-2}}{1-(2+(a+e)T)z^{-1}+(1+(a+e)T)z^{-2}}v'[k]\ , \quad (4)$$

in which $v'[k] = \omega\sigma L_s i_{ds}[k] + v_{ds}[k]$. It should be noted that ω_r is not included in (4) because back EMF(Electro-Magnetic Force) never appear in the direction of rotor flux (*d* axis). Consequently, this paper deals with this equation as identification model of the induction motor, whose parameters *a*, *e* and *g* should be identified.

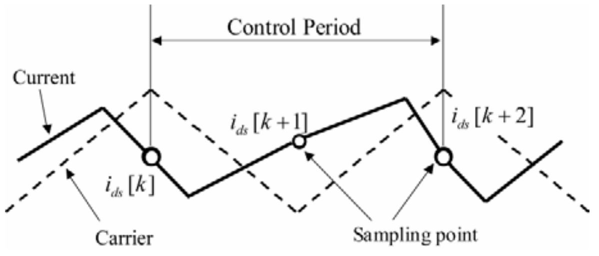

Fig. 1: Output inter-sampling approach in consideration of PWM carrier

III. PARAMETER IDENTIFICATION USING OUTPUT INTER-SAMPLING APPROACH

As previously mentioned, it is impossible to identify all parameter of sensorless vector controlled induction motor under steady state. Hence, some high frequency signals or 'Maximum-length linear shift register sequence signal' injection are required. It should be noted that these signals to identify some parameters would deteriorate performance of controlled motor and require larger capacity of PWM inverter. Hence, it can be concluded that smaller amplitude of injected signal would be desirable. Few approaches to reduce this injected signal amplitude, however, have not been proposed so far. This section describes a novel identification method using output inter-sampling approach [6].

Output inter-sampling [6] means to detect outputs of controlled object at smaller detection period T_d than the control-sampling period T_c $(T_d < T_c)$. The detail time chart in this paper is shown in Fig.1. In general, inter-sampling rate $p = T_c / T_d$ can be arbitrarily determined [6]. It should be noted that, in the case of AC drives, the control period and the detection one are usually synchronized with the PWM carrier in order to reduce the influence of the PWM carrier harmonics, which is often superimposed on detected stator current. Hence, the same consideration is required even when carrying out the output inter-sampling for the identification accuracy improvement. As a result, it is thought out that the current should be detected at the point as shown in Fig.1. Therefore, inter-sampling rate p is set to p=2. In this paper, the control period is set to 200 μs and the detection period is made into 100 μs since carrier frequency is 5kHz. All sampling operations are synchronized.

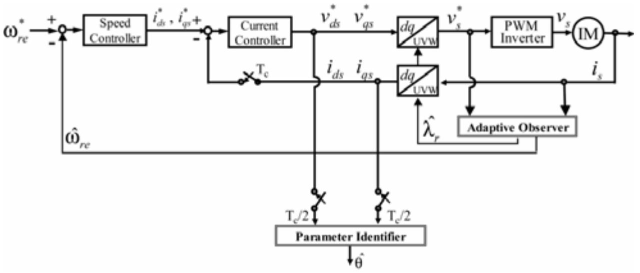

Fig. 2: Speed senssorless vector control system using adaptive observer with parameter identifier based on output inter-sampling approach

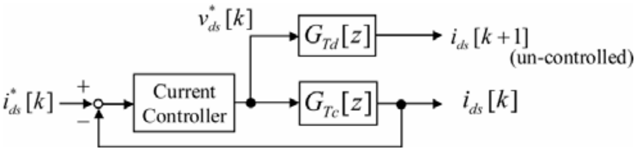

Fig. 3: Representation of single-input multi-out put model structure

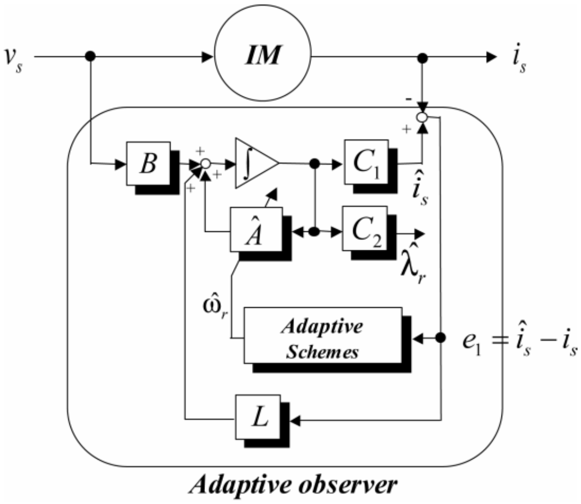

Fig. 4: configuration of adaptive observer

Fig. 2 shows speed sensorless vector control system using an adaptive observer with proposed identifier based on inter-sampling approach, in which the proposed parameter identifier is constructed on *d-q* axis because the identification model structure is also expressed in this coordinate as shown in (4).

Fig.3 represents the single-input multi-output model structure of inter-sampled system, in which $G_{Tc}[z]$ and $G_{Td}[z]$ mean the pulse transfer functions from the reference voltage $v_{ds}^*[k]$ to $i_{ds}[k]$ and $i_{ds}[k+1]$, respectively. It should be noted from this figure that $i_{ds}[k]$ is forced to be its reference $i_{ds}^*[k]$, but $i_{ds}[k+1]$ is not controlled. Hence, this inter-sampled system partly constructs the open-loop system, the design of vector controller is not affected by applying output inter-sampling approach. It should be noted that the inter-sampled data $i_{ds}[k+1]$ would perturb due to influence of parameter mismatches because this inter-sampled current is not regulated by the current controller. This implies that $i_{ds}[k+1]$ possesses more knowledge on induction motor parameters. Therefore, it can be expected that the amplitude of the injected signal is reduced for accurate parameter identification. In other words, identifiability condition can be extremely relaxed by using this inter-sampling approach [6], and identification accuracy will be improved if this input-output signal possesses enough degree in terms of PE property.

In this paper, three parameters, a, e and g are identified based on ARMAX (Auto-Regressive Moving Average eXogenous) model in Matlab/System Identification Toolbox.

IV. ROBUST ADAPTIVE OBSERVER DESIGN WITH LESS PHASE ERROR

The proposed identification requires that the direction of the actual rotor flux is assumed to be aligned with that of the estimated flux by using an adaptive observer. In adaptive observers with speed adaptation, the flux estimation error theoretically converge to zero in steady state despite there exists parameter mismatches in a, e and g, while the steady state error of the speed adaptation would be induced. In reality, however, rotor flux cannot be perfectly estimated at steady state as well as transient state due to detuned parameter used in the adaptive observer. Hence it is so necessary to the design the adaptive observer, which can estimate the direction of rotor flux (d axis) for precise parameter identification. This section describes the design strategy of observer gain to reduce phase estimation error of rotational reference frame (d-q axis) [9].

A. Configuration of adaptive observer

In this subsection, the adaptive observer with the speed identifier is briefly outlined.

The state equation of the induction motor in a rectangular coordinate fixed to the stator is expressed by

$$\frac{d}{dt}\boldsymbol{x} = \boldsymbol{A}\boldsymbol{x} + \boldsymbol{B}\boldsymbol{v}_s, \tag{5}$$

$$\boldsymbol{i}_s = [\boldsymbol{I} \quad \boldsymbol{o}_{2\times 2}]\,\boldsymbol{x} = \boldsymbol{C}_1\boldsymbol{x}\ , \tag{6}$$

in which

$$A = \begin{bmatrix} a\boldsymbol{I} & c\boldsymbol{I} - \frac{\omega_r M}{\sigma L_s L_r}\boldsymbol{J} \\ b\boldsymbol{I} & e\boldsymbol{I} + \omega_r \boldsymbol{J} \end{bmatrix},\ B = \begin{bmatrix} g\boldsymbol{I} & 0_{2\times 2}\end{bmatrix}^T\ ,$$

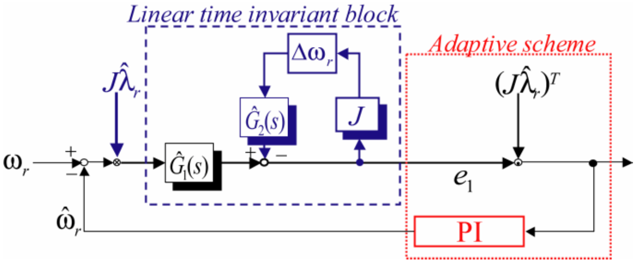

Fig. 5: Block diagram of speed identification system

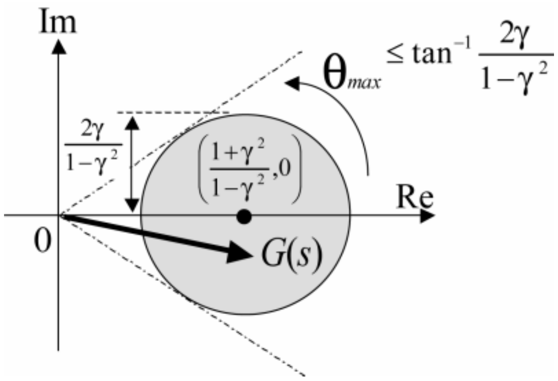

Fig. 6: γ -Positive realness

Where, I and J are the unit matrix and the skew symmetric matrix of 2x2, respectively.

For the rotor flux estimation and the speed identification, the adaptive full-order observer is constructed as follows:

$$\frac{d}{dt}\hat{\boldsymbol{x}} = \hat{\boldsymbol{A}}\hat{\boldsymbol{x}} + \boldsymbol{B}\boldsymbol{v}_s + \boldsymbol{L}\boldsymbol{e}_1, \tag{7}$$

$$\hat{\boldsymbol{i}}_s = \boldsymbol{C}_1\hat{\boldsymbol{x}}\ , \tag{8}$$

$$\hat{\boldsymbol{\lambda}}_r = [\boldsymbol{o}_{2\times 2} \quad \boldsymbol{I}]\,\hat{\boldsymbol{x}}\ = \boldsymbol{C}_2\hat{\boldsymbol{x}}\ , \tag{9}$$

$$\hat{\omega}_r = \left(K_p + \frac{K_I}{s}\right)\left((\boldsymbol{J}\hat{\boldsymbol{\lambda}}_r)^T\boldsymbol{e}_1\right)\ , \tag{10}$$

where $\boldsymbol{e}_1 = \hat{\boldsymbol{i}}_s - \boldsymbol{i}_s$ and L means an observer gain. Fig.4 shows the configuration of the adaptive observer, in which adaptive scheme stands for equation (10). In this paper, ω_r is regarded as a time invariant parameter due to the difference between the time constant of mechanical system and that of electrical system.

B. Error system of speed identification

Subtracting (5) and (6) from (7) and (8), the influence of current estimation error e_1 on speed identification error $\Delta\omega_r = \hat{\omega}_r - \omega_r$ can be described as follow:

$$\begin{aligned} \boldsymbol{e}_1 &= \boldsymbol{C}_1(s\boldsymbol{I} - \hat{\boldsymbol{A}} - \boldsymbol{L}\boldsymbol{C}_1)^{-1}\boldsymbol{B}_{\omega_r}(-\Delta\omega_r\boldsymbol{J}\boldsymbol{\lambda}_r) \\ &= \hat{\boldsymbol{G}}_1(s)\boldsymbol{J}\boldsymbol{\lambda}_r(\omega_r - \hat{\omega}_r)\ \ , \end{aligned} \tag{11}$$

in which

$$\hat{\boldsymbol{G}}_1(s) = \boldsymbol{C}_1(s\boldsymbol{I} - \hat{\boldsymbol{A}} - \boldsymbol{L}\boldsymbol{C}_1)^{-1}\boldsymbol{B}_{\omega_r}\ , \tag{12}$$

$$\boldsymbol{B}_{\omega_r} = [\boldsymbol{I}/\varepsilon \quad -\boldsymbol{I}]^T. \tag{13}$$

In addition, the influence of flux estimation error $\boldsymbol{e}_2 = \hat{\boldsymbol{\lambda}}_r - \boldsymbol{\lambda}_r$ on $\Delta\omega_r$ is given by

$$\begin{aligned} \boldsymbol{e}_2 &= \boldsymbol{C}_2(s\boldsymbol{I} - \hat{\boldsymbol{A}} - \boldsymbol{L}\boldsymbol{C}_1)^{-1}\boldsymbol{B}_{\omega_r}(-\Delta\omega_r\boldsymbol{J}\boldsymbol{\lambda}_r) \\ &= \hat{\boldsymbol{G}}_2(s)(-\Delta\omega_r\boldsymbol{J}\boldsymbol{\lambda}_r) \end{aligned} \tag{14}$$

in which

$$\hat{\boldsymbol{G}}_2(s) = \boldsymbol{C}_2(s\boldsymbol{I} - \hat{\boldsymbol{A}} - \boldsymbol{L}\boldsymbol{C}_1)^{-1}\boldsymbol{B}_{\omega_r}\ . \tag{15}$$

Hence, the transfer function from the actual rotor flux to the estimated one in consideration of $\Delta\omega_r$ can be formulated as

$$\hat{\boldsymbol{\lambda}}_r = \boldsymbol{\lambda}_r + \boldsymbol{e}_2 = (\boldsymbol{I} + \boldsymbol{G}_2(s)\Delta\omega_r\boldsymbol{J})\,\boldsymbol{\lambda}_r\ , \tag{16}$$

and substituting (16) into (11),

$$\boldsymbol{e}_1 = \left(\boldsymbol{I} + \hat{\boldsymbol{G}}_2(s)\Delta\omega_r\boldsymbol{J}\right)^{-1}\left(\hat{\boldsymbol{G}}_1(s)\boldsymbol{J}\hat{\boldsymbol{\lambda}}_r(\omega_r - \hat{\omega}_r)\right) \tag{17}$$

can be obtained. From (10) and (17), the nonlinear feedback loop of the speed identification is constructed as shown in Fig.5.

To reduce the phase estimation error, the phase characteristics of the transfer function in (16) needs to be manipulated as small as possible. In the following, the design, which can reduce phase estimation error, is described.

C. γ –Positive realness for robust flux phase estimation

In this subsection, a notion of γ -positive realness [10] is introduced for the phase specification of a transfer function, since the notion of γ -positive realness enables us to solve the phase specification.

Given a transfer function $G(s)$ in general, $G(s)$ is γ -positive real [10] if and only if, in case of single-input single-output system $G(s)$, the Nyquist diagram of $G(s)$ exists in the circle (see Fig.6) of which center and radius are $\left(\frac{1+\gamma^2}{1-\gamma^2},\ 0\right)$ and $\frac{2\gamma}{1-\gamma^2}$, respectively. It turns out from Fig.6 that the maximum of $|\angle G(s)|$ can be bounded by

$$\theta_{\max} = \tan^{-1}\frac{2\gamma}{1-\gamma^2}\ . \tag{18}$$

It can be seen from this equation that the smaller γ is found, the smaller $\theta_{\max}$ is achieved. Based on γ -positive realness, it is possible that the phase characteristics of

$G(s)$ are manipulated. The design strategy to find $G(s)$ γ-positive real is called as γ-positive real problem.

In this observer gain design, $\boldsymbol{I}+\hat{\boldsymbol{G}}_2(s)\Delta\omega_r\boldsymbol{J}$ should be γ-positive real for small positive scalar γ. In this paper, this design strategy is introduced for the phase characteristics shaping of certain transfer function.

To solve directly the aforementioned design problem is difficult, but [10] has also shown that the problem can be solved as H_∞ control problem by using Cayley transformation:

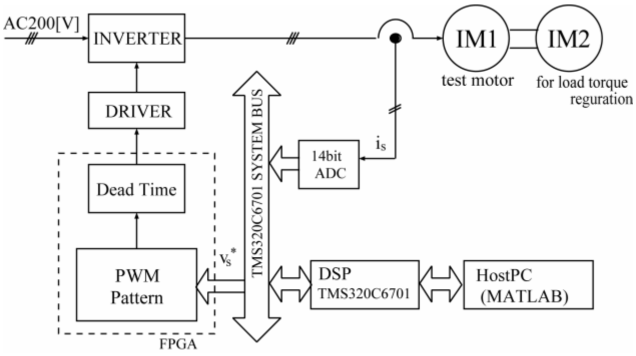

Fig. 7: Experimental setup

$$H(s)=(G(s)-I)(G(s)+I)^{-1}\,. \tag{19}$$

Then, $|\angle G(s)|$ can be reduced by applying H_∞ control problem for $H(s)$.

D. Observer gain design based on γ-positive real problem

The transfer function from actual rotor flux to estimated one is given by (16), and this phase characteristics should be reduced. Using γ-positive realness, necessary condition for stable speed identification is that $\boldsymbol{I}+\hat{\boldsymbol{G}}_2(s)\Delta\omega_r\boldsymbol{J}$ is γ-positive real for small positive scalar γ under given $\Delta\omega_r$, because to achieve positive real $\hat{G}_1(s)$ is almost equivalent to the reduction of flux phase estimation error as previously described [9].

According to our design strategy [9], $\boldsymbol{I}+\hat{\boldsymbol{G}}_2(s)\Delta\omega_r\boldsymbol{J}$ is γ-positive real for small positive scalar γ if and only if there exists $X=X^T>0$, and K such that

$$\begin{bmatrix} \boldsymbol{X\Gamma}+\boldsymbol{KC}_1+\boldsymbol{\Gamma}^T\boldsymbol{X}+\boldsymbol{C}_1^T\boldsymbol{K}^T & \boldsymbol{XB}_{\omega_r}\Delta\omega_r\boldsymbol{J}/\sqrt{2} & \boldsymbol{C}_2^T/\sqrt{2} \\ (\boldsymbol{B}_{\omega_r}\Delta\omega_r\boldsymbol{J})^T\boldsymbol{X}/\sqrt{2} & -\gamma\boldsymbol{I} & \boldsymbol{o}_{2\times2} \\ \boldsymbol{C}_2/\sqrt{2} & \boldsymbol{o}_{2\times2} & -\gamma\boldsymbol{I} \end{bmatrix} < 0\ , \tag{20}$$

in which

$$\boldsymbol{\Gamma}=\hat{\boldsymbol{A}}-\frac{\boldsymbol{B}_{\omega_r}\Delta\omega_r\boldsymbol{JC}_2}{2}.$$

Next, in consideration of implementation, the pole of the observer is restricted by the following LMIs [11]:

$$\begin{bmatrix} -r\boldsymbol{X} & \boldsymbol{X}\hat{\boldsymbol{A}}+\boldsymbol{KC}_1 \\ \boldsymbol{C}_1^T\boldsymbol{K}^T+\hat{\boldsymbol{A}}^T\boldsymbol{X} & -r\boldsymbol{X} \end{bmatrix} < 0, \tag{21}$$

and

$$\boldsymbol{X}\hat{\boldsymbol{A}}+\boldsymbol{KC}_1+\hat{\boldsymbol{A}}^T\boldsymbol{X}+\boldsymbol{C}_1^T\boldsymbol{K}^T+2h\boldsymbol{X}<0\ , \tag{22}$$

for some *r*>0 and *h*>0. By minimizing γ under constraints (20) - (22) with Matlab/LMI Toolbox, X and K can be obtained. As a result, the robust observer gain is determined as

$$L=X^{-1}K\quad. \tag{23}$$

V. EXPERIMENTS

A. Experimental setup

Some experiments were carried out to confirm feasibility and effectiveness of the proposed system shown in Fig.2. The experimental setup shown in Fig. 7 consists of a tested induction motor (1.5kW) fed by a voltage source PWM inverter, regulated by speed control mode, and another induction motor (2.2kW) for the load torque regulation. In addition, the stator current was detected by 14bit ADC. On the other hand, the stator voltage on *d-q* axis, which is utilized for parameter identification, were substituted for voltage reference v_{ds}^*, v_{qs}^*, which can be obtained from output of current controller shown in Fig.2.

The tested induction motor parameters are shown in Table 1. Theses parameters of the tested motor were measured by the no-load test and the locked test using sinusoidal power source.

The adaptive observer (which was constructed on $\alpha-\beta$ coordinate), the speed controller, the current controller, and the coordinate transformer were executed by DSP(TI:TMS320C6701), and the pulse width modulation of the stator voltage reference was made by FPGA(Altera:EPF10K20TC144-4), where the DC link voltage and the carrier frequency of the PWM inverter were set to 200V and 5kHz, respectively.

TABLE 1 PARAMETER OF TESTED MOTOR

Rated power	1.5kW
Rated speed	1710min^{-1}
Rated stator voltage	200V
Rated stator current	6.2 A
Stator resistance	0.9Ω
Rotor resistance	0.784Ω
Stator inductance	110 mH
Rotor inductance	98.0 mH
Mutual inductance	98.0 mH

B. Identification results at standstill

First, the tested induction motor was kept at standstill for simplification. In this parameter identification experiments, M sequence signal was injected into the *d*-axis current reference as the exogenous signal, in which the amplitude of M sequence signal changed from 0.1A to 0.5A, and voltage reference data and measured current ones were detected for 5 seconds, respectively. Based on (4), parameter identification was performed in off-line by ARMAX model [8] in MATLAB/System Identification Toolbox, and Fig.8 shows average for 5 times data of same identification experiments. For evaluation of parameter identification results $\hat{\theta}=[\hat{a}\ \ \hat{e}\ \ \hat{g}]^T$,this paper utilizes the following equation as 2-norm of each parameter identification error:

$$Identification\ Error\ =\sqrt{\left(\frac{a-\hat{a}}{a}\right)^2+\left(\frac{e-\hat{e}}{e}\right)^2+\left(\frac{l-\hat{l}}{l}\right)^2}\ , \qquad (24)$$

where $l=g^{-1}$ is the leakage inductance. $\theta=[a\ \ e\ \ g]^T$ is a nominal value vector, which is obtained from motor parameter by no-load test and the locked-test in advance.

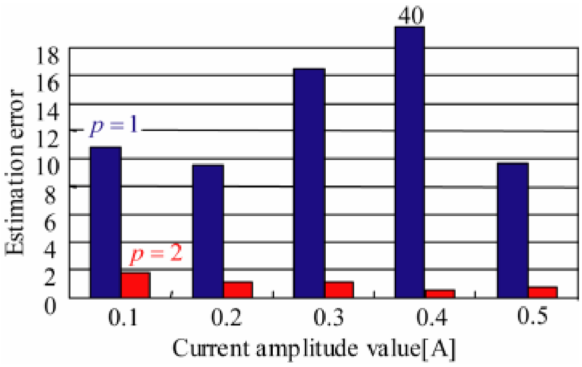

Fig. 8: Identification estimation error of standstill

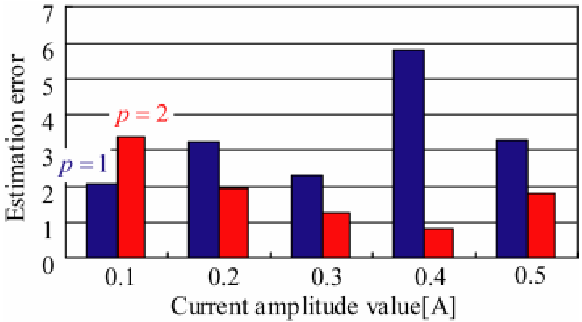

Fig. 9: Identification estimation error of no-load (180min^{-1})

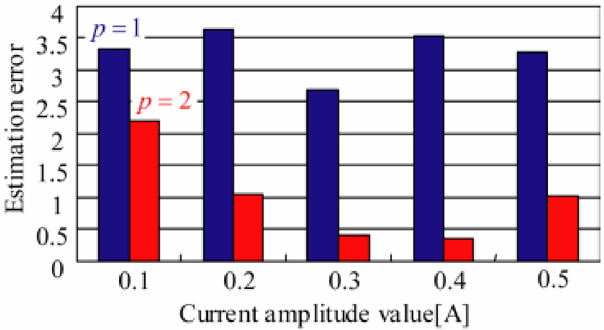

Fig. 10: Identification estimation error of half-load (180min^{-1})

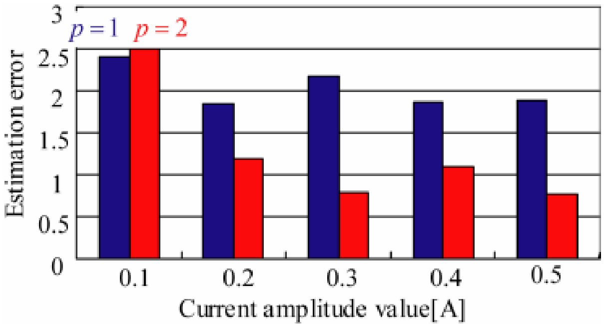

Fig. 11: Identification estimation error of full-load (180min^{-1})

It can be seen from Fig.8 that the parameter identification accuracy using output inter-sampling approach (*p*=2) is dramatically superior to conventional method (*p*=1) as previously expected. In addition, it is revealed from this figure that parameter identification was becoming more precise as M sequence signal enlarged. In other words, the output inter-sampling approach makes it possible to realize a certain accuracy of parameter identification with less amplitude of injected signal for parameter identifiability.

C. Identification results at 180 min^{-1} *under various load conditions*

Next, identification experiments were carried out when the tested induction motor was operated at 180 min^{-1}. Figs. 9,10 and 11 show the identification error when induction motor was operated at 180 min^{-1}\$ under no-load, 50%, and 100% load, respectively. The results of parameter identification were also evaluated by (24). It can be seen from these figures that the parameter identification error decreased by about 50% in average, which concludes that identification based on output inter-sampling approach is effective.

According to the literature [7], this is because the identifiability condition of the parameter can be relaxed so much, and the amount of input data and output ones increase twice in comparison with p=1. In addition, since PE condition for identification is satisfied by M sequence signal in input and output, it is thought that the accuracy of parameter identification can be improved.

As described above, to apply of output inter-sampling approach to parameter identification would be effective for identification accuracy at 180min-1 as well as at standstill. However, identification results of output inter-sampling approach at 180min-1 were inferior to that at standstill. This is because the phase estimation error of rotor flux, which is estimated by the adaptive observer, would slightly affect to parameter identification despite the proposed identification model (4) requires the assumption that the phase estimation error does not exist.

Although many literatures have already been described rotor flux estimation of induction motors [2] and a few parameter identification (only speed, stator resistance and rotor one) using high frequency signal injection [3][4], few literature deals with to decrease amplitude of the injected signal by parameter identification strategy, where the injected signal would cause losses and acoustic noise. Hence, general comparison of the proposed method with these methods would be difficult, but the proposed method is said to be superior in terms that this paper tackles simultaneous identification of all parameter of induction motors, and deals with amplitude minimization of the injected signal injection, which is necessary for parameter identification, but is not necessary for control the motor.

D. Influences of thermal variation on parameter identification characteristics

In this subsection, influences of thermal variation on parameter identification characteristics were surveyed, whose results are shown in Fig.12. In these experiments, amplitude of M sequence signal was 0.4A, and parameter identification was carried out every 10 minutes after half load was applied. Temperature of the tested motor surface was measured by a thermal sensor (IT-550 by HORIBA) at the same time.

It turns out from this figure that error of parameter identification using conventional method (p=1) was fluctuated regardless of temperature variation. On the other hand, it can be seen that identification error of proposed method (p=2) enlarged in relation with increase of motor surface temperature. This implies that the proposed method would catch up resistive parameter variation of the test motor, which is caused by temperature variation, because identification error was calculated with constant nominal parameters. From these results, it can be concluded that the proposed method becomes effective of parameter identification strategy.

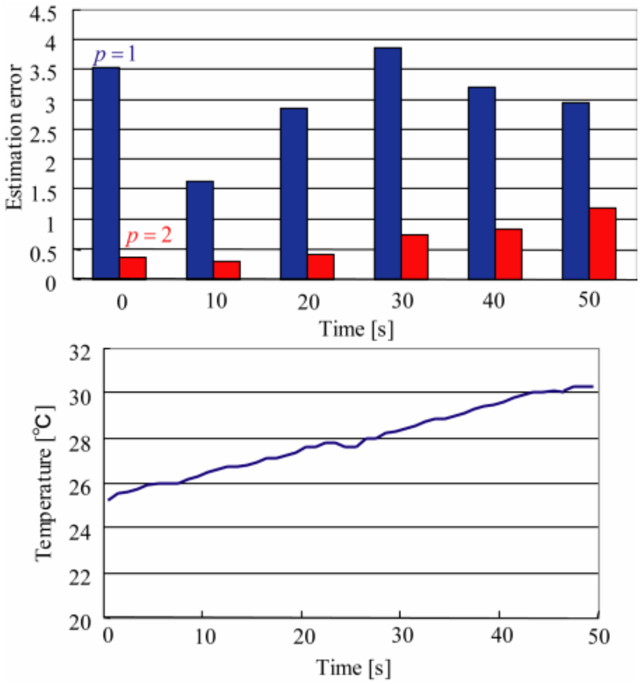

Fig. 12: Influences of thermal variation on parameter identification characters

E. Discussions using singular values of data matrix

Finally, this subsection quantitatively evaluates effectiveness of the proposed method. Identification model (4) can be formulated without any generality by

$$i_{ds}[k]=\frac{b_1 z^{-1}+b_2 z^{-2}}{1+a_1 z^{-1}+a_2 z^{-2}} v'[k] \tag{25}$$

and, this is manipulated by the following:

$$\begin{bmatrix} i_{ds}[2] \\ \vdots \\ i_{ds}[n] \end{bmatrix} = \left[\begin{matrix} -i_{ds}[1] & -i_{ds}[0] \\ \vdots & \vdots \\ -i_{ds}[n-1] & -i_{ds}[n-2] \end{matrix} \right. * $$

$$ * \left. \begin{matrix} v'[1] & v'[0] \\ \vdots & \vdots \\ v'[n-1] & v'[n-2] \end{matrix} \right] \begin{bmatrix} a_1 \\ a_2 \\ b_1 \\ b_2 \end{bmatrix}.$$

For simple notation,

$$Y=\Omega\Theta\ . \tag{26}$$

This equation describes that output data Y will be sensitive to identified parameter Θ when a norm of data matrix Ω enlarges. In this case, singular value is well known as evaluation of this norm of Ω. Pseudo-inverse matrix of Ω tends to be numerically stable if the products of all singular values of Ω, which makes it possible to realize accurate parameter identification.

Fig.13 shows the products of all singular values characteristics with respect to amplitude of injected M sequence signal. This figure demonstrates that the products of all singular values of Ω with respect to amplitude of M sequence signal under half load condition. These plots mention that the norm of Ω in the proposed method becomes considerable larger than the other, one can conclude from these singular values that this is why the proposed method becomes effective for parameter identification.

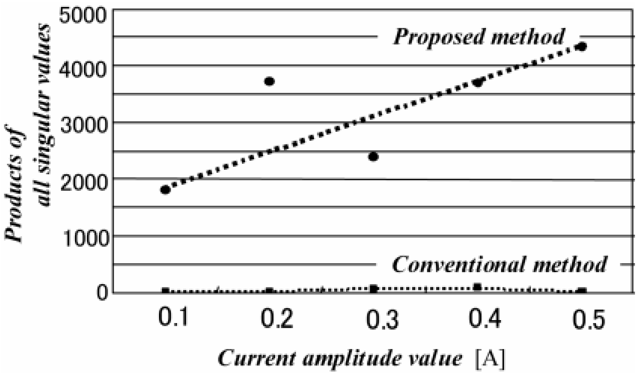

Fig. 13: Singular values of data matrix (half load condition)

IV. CONCLUSION

This paper has shown how to apply parameter identification based on output inter-sampling approach to speed sensorless vector controlled induction motor. Both identification results at standstill and that at 180min^{-1} under three-load conditions with output inter-sampling approach show that the accuracy of the parameter identification can be improved. In addition, this paper has revealed why the proposed identification method becomes effective using singular matrix of data matrix. As a result, the proposed approach is concluded to be effective for vector controlled induction motor.

ACKNOWLEDGMENT

This work was partly supported by The High-Tech Research Center Establishment Project from the Ministry of Education, Culture, Sports, Science and Technology in Japan.

REFERENCES

[1] S.Shinnaka: 'A Unified Analysis on Simultaneous Identification of Velocity and Rotor Resistance of Induction motors', JapanIEE Transactions, 113-D, No.12, 1993, pp.1483–1484 (in Japanese).

[2] K.Ide, J.I.Ha, *M.* Sawamura, H. Iura, Y.Yamamoto, 'High Frequency Injection Method Improved by Flux Observer for Sensorless Control of an Induction Motor', Proceedings of the, Power Conversion Conference, PCC Osaka 2002. Volume 2, 2-5 April 2002, pp. 516 – 521.

[3] T.Noguchi, S. Kondo, I. Takahashi, “Field-Oriented Control of an Induction Motor with Robust On-Line Tuning of Its Parameters”, IEEE Trans Industry Applications, Vol.33, No.1, 1997, pp.35-42.

[4] Y.Kinpara and M.Koyama: “Speed Sensorless Vector Control Method of Induction Motor Using Dual Adaptive Flux Observer for Resistance Identification”, JapanIEE Transactions, Vol.120-D, No.8/9, 2000, pp.1061–1067. (in Japanese)

[5] K.Akatsu and A.Kawamura: 'Sensorless speed estimation of induction motor based on the secondary and primary resistance on-line identification without any signal injection', Power Electronics Specialists Conference 1998, pp.1575–1580.

[6] L.Sun and A.Sano: “Output Inter-Sampling Approach to Closed-Loop Identification”, Vol.35, No.8, 1999, pp.1069–1077. (in Japanese)

[7] L.Sun, H.Ohmori and A.Sano: “Direct Closed-Loop Identification Approach to Unstable Plant”, Proceedings of the 39th IEEE Conference on Decision and Control, Vol. 2, 12-15 Dec. 2000, pp. 1148 – 1153.

[8] S.Adachi: “System identification for control using Matlab”, Tokyo Denki Publishing, 1997 (in Japanese)

[9] M.Hasegawa, ”Robust-Adaptive-Observer Design Based on γ -Positive Real Problem for Sensorless Induction-Motor Drives”, IEEE Trans. Industrial Electronics, Vol. 53, No. 1, 2006, pp.76-85.

[10] N.Sakamoto and M.Suzuki, “γ -Passive System and Its Phase Property and Synthesis”, IEEE Trans Automatic Control, Vol. 41, No.6, June 1996, pp. 859-865.

[11] P.Gahinet and M.Chilali, “H_∞ Design with Pole Placement Constraints: An LMI approach”, IEEE Trans Automatic Control, Vol.45, No.3, Mar 1996, pp.358-367.

BIOGRAPHIES

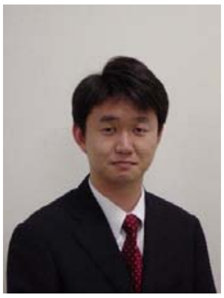

Masaru Hasegawa was born in Gifu Prefecture, Japan, on August 25, 1972. He received the B.Eng., M. Eng., and Dr. Eng. degrees in electrical engineering from Nagoya University, Japan, in 1996, 1998, and 2001, respectively. He is currently an Associate Professor at Chubu University, Japan. His research interests are in the area of control theory and application to motor drives and renewable energy. Dr. Hasegawa is a member of the IEEE and the Society of Instrument and Control Engineers of Japan. He received the Paper Award of Fanuc FA Robot Foundation and IEEE-IECON'03 Presentation Award.

Daisuke Ogawa was born in Aichi Prefecture,Japan, on June 3, 1981. He received the B.Eng., and M.Eng. degrees in electrical engineering from Chubu University, Aichi, Japan, in 2004 and 2006, respectively. He studied parameter identification of induction motors.

Keiju Matsui was born in Ehime Prefecture, Japan, on September 20, 1942. He received the B.Eng. degree in electrical engineering from Ehime University, Matsuyama, Japan, in 1965, and the Dr. Eng. degree from the Tokyo Institute of Technology, Tokyo, in 1982. Since 1965, he has been with the Department of Electrical Engineering, Chubu University, Kasugai, Japan, where he is currently a professor and is engaged in research on static power converter. Dr. Matsui received the Prize Award from the Institute of Electrical Installation Engineers of Japan in 1997 and the Outstanding Book Award from the Institute of Electrical Engineers of Japan in 1999. He is a member of the IEEE and the Society of Instrument and Control Engineers of Japan.

Zigzag Autotransformer Based Full-Wave AC-DC Converters

Bhim Singh[1] and Sanjay Gairola[1]

Abstract – In this paper, a new class of zigzag autotransformer based full-wave AC-DC converters is designed, modeled and simulated to feed non-isolated DC varying loads. The proposed AC-DC converters are suitable in applications such as drives, battery charging, process industries, field excitation systems, etc., where isolation is not essentially required. It is considered as an alternative to the popular bridge configuration having one diode in the path of load current with improved power quality.

Keywords – AC-DC Converters, Power Quality, Zigzag Autotransformer

I. INTRODUCTION

An ANSI 45 configuration of 6-pulse full-wave AC-DC converter shown in Fig. 1, is popularly used for low-voltage and high-current applications that require minimum voltage drop due to source impedance, leakage reactance and in devices used in the path of load current. These full-wave converters generally have star or zigzag secondary. The full-wave rectifiers (not the bridge rectifiers) have only one device in the path of load current and preferred in industrial applications such as electro-chemical, induction heating processes, etc. The six-phase full-wave rectifier of Fig. 1 employs a delta/ double-star transformer (ANSI 45 configuration) and an interphase reactor (IPR). A diode is connected in each output phase for rectification and the technology is well established. Two three-phase output groups are connected so that one is of opposite instantaneous polarity of the other. This mutual disposition of 180° would give six-phase diametric vector if no interphase reactor (IPR) or interphase transformer (IPT) is present and two neutrals are directly connected [1].

It is a usual practice to employ multiple 12-pulse or 18-pulse AC-DC converters fed from such phase–staggered transformers to meet IEEE-519 standard [2] requirements as the total harmonic distortion (THD) of input line currents of single unit is high and may not qualify as clean power at high loads. The isolation transformers used for high currents can have different winding arrangements such as star, delta, fork, zig-zag, polygon etc. The isolation transformers used for full-wave rectifiers have generally delta or star primary winding (sometime polygon winding also) and star or zigzag or fork secondary windings [3-5]. The star, zigzag and fork windings provide neutral point for full-wave rectifiers, however, two secondary windings have interphase reactors between neutral points as shown in Fig. 1 for full utilization of devices. But a six-phase full-wave AC-DC converter affects the voltage at the point of common coupling (PCC) due to current distortion. Multipulse AC-DC converters are effective in improving power quality where transformers (auto-wound and separately-wound) are employed to generate more phases [6-7] and increase the pulse number in AC-DC converters. ANSI 45 and ANSI 46 transformers are employed together [8] to make the full-wave 12-pulse AC-DC converter. Maslin et. al. [9] have reported a 12-phase full-wave AC-DC converter based on zigzag transformers for electrical induction apparatus. This twelve-pulse converter uses two three-phase transformers having star and delta primary windings but identical zigzag secondary windings [3-5]. This rectifier configuration is reported to use seven interphase reactors. But it is observed that the total harmonic distortion (THD) of input current is not within the IEEE-519 Standard permissible limits in all cases and tuned passive filters are extensively used along with it

ANSI 45 and ANSI 46 rectifier combinations are also described by Brown [10] for copper electro-winning industry. Miyari et. al. [11] have explained a method of pulse multiplication in 6-pulse full-wave rectifiers but it adds one more semiconductor device in the path of load current. An 18-pulse diode bridge based front end AC-DC converter for electrolytic application is explained by Wiechmann et. al. [12]. This topology also have two devices in the path of load current and hence additional voltage drop and losses that is not desired on secondary side as the load current is very large.

The problem with full-wave AC-DC converter in isolated configurations is that the transformer size is nearly 125-145% [5] of the power transferred as only 50% of the windings are effectively used at any instant. But the isolation is very much required in such low-voltage applications for stepping down the voltage and thus these are used extensively. However, full-wave autotransformer based converters that have reduced magnetic rating are not

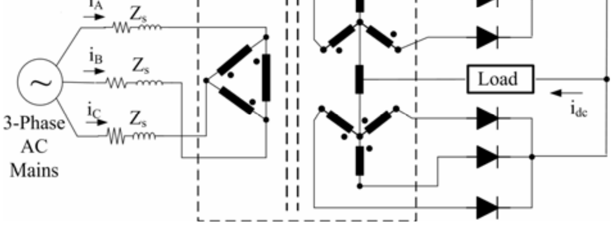

Fig. 1: A 6-phase full-wave AC-DC converter using delta/double-star transformer (ANSI 45 rectifier).

The paper first received 12 Jun 2007 and in revised form 13 Mar 2008.
Digital ref: AI70201166

[1] Department of Electrical Engineering, Indian Institute of Technology, Delhi New-Delhi, India, E-mail: bhimsinghr@gmail.com, sanjaygairola@gmail.com

seen in literature.

The non-isolated full-wave AC-DC converters are not known, mainly due to popularity of AC-DC converters employing bridge configurations and the m.m.f. (magneto-motive-force) balance provided by it. However, it is worth noting that the number of devices required in six-pulse AC-DC converter employing full-wave configuration is same as that employed by a six-pulse bridge arrangement, while the forward voltage drop due to the diodes/ thyristors, is reduced. Moreover, the output voltage is reduced to about 57% of that of isolated case. In this paper, a class of non-isolated full-wave AC-DC converters is proposed for applications such as magnet power supplies, battery charging, electrolytic process, motor control, etc. The proposed 6-pulse, 12-pulse, 18-pulse and 24-pulse full-wave AC-DC converters are fed from zigzag-connected autotransformers. Detailed design of the transformer and resulting full-wave diode rectifier systems are carried out to study the behavior of the AC-DC converters. The designed converter systems are modeled and simulated in MATLAB to demonstrate power quality improvement at AC mains. The laboratory prototypes are also developed to validate the design and model of these proposed converters. In higher number of pulse configurations of these converters, power quality at AC mains is improved and qualify IEEE-519 standard requirements.

II. PROPOSED FULL-WAVE AC-DC CONVERTER

Fig. 2 shows the proposed 6-pulse full-wave AC-DC converter. In this configuration zigzag connected autotransformer is used. The design is described as follows.

A. Design of Zigzag Autotransformer Suitable for 6-Pulse Full-Wave AC-DC Converter

Fig. 2 shows the schematic of the proposed zigzag connected autotransformer winding arrangement and its connection to two full-wave converters, FW1 and FW2. Two full-wave converters FW1 and FW2 are connected to two sets of three-phases at (A_1, B_1, C_1) and (A_2, B_2, C_2) respectively. Fig. 3 depicts the graphical representation of the autotransformer windings and angular position of various voltage phasors. Two sets of three phase voltages are (V_{A1}, V_{B1}, V_{C1}) and (V_{A2}, V_{B2}, V_{C2}). These sets are displaced by 60° from each other and at +30° and -30° respectively from AC mains voltage V_A. The number of turns for every winding are determined as a function of the phase voltage, V_A(=V). These voltages, as marked in Fig. 3, are expressed by following relationships.

Consider the set of three phase supply voltages as:

$$V_A = V\angle 0°,\ V_B = V\angle -120°, V_C = V\angle 120° \tag{1}$$

$$|V_A| = V_R = 1.1547V_A \tag{2}$$

The required voltages for the converters I (FW1) are:

$$V_{A1} = V_R\angle 30°,\ V_{B1} = V_R\angle -90°, V_{C1} = V_R\angle 150° \tag{3}$$

The required voltages for the converters II (FW2) are:

$$V_{A2} = V_R\angle -30°,\ V_{B2} = V_R\angle -150°, V_{C2} = V_R\angle 90° \tag{4}$$

The values of constants K_1 to K_3 marked in Fig. 3, determine the winding voltages as a fraction of phase windings turns. The value of output voltage phasors can also be expressed in terms of input phase and line voltages as:

$$V_{A1} = K_1V_{AB} - K_1V_{CA} - K_2V_{BC} \tag{5}$$

$$V_{A2} = K_1V_{AB} - K_1V_{CA} + K_2V_{BC} \tag{6}$$

$$V_{C2} = V_C + K_2V_{AB} \tag{7}$$

Eqns. (5-7) give the values of constants K_1 and K_2 for desired phase shift as

$$K_1 = 0.5773,\ K_2 = 0.5773 \tag{8}$$

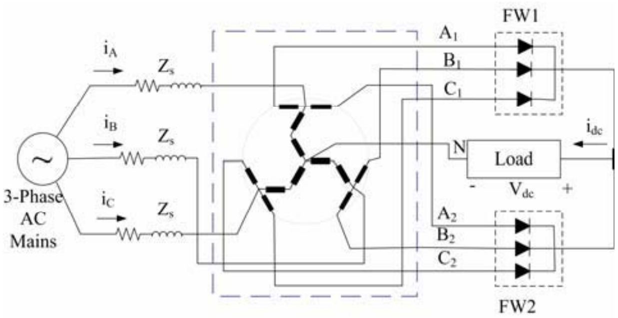

Fig. 2: Proposed zigzag autotransformer based 6-pulse full-wave AC-DC converter.

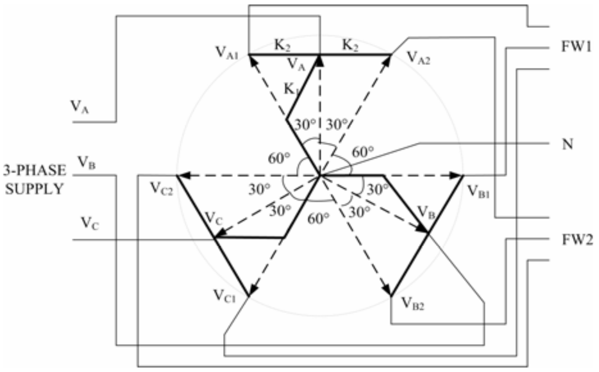

Fig. 3: Winding arrangement and phasor diagram of transformer for 6-pulse non-isolated full-wave AC-DC converter.

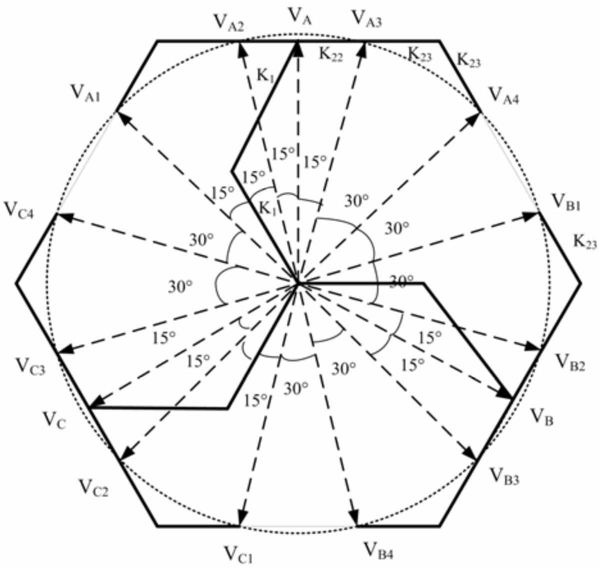

Fig. 4: Winding arrangement and phasor diagram of autotransformer for 12-pulse non-isolated full-wave AC-DC converter converter.

This full-wave converter autotransformer configuration approach has been further modified to get the designs of zigzag autotransformers for 12-pulse, 18-pulse and 24-pulse AC-DC converter configurations. Fig. 4 shows autotransformer winding arrangement for 12-pulse AC-DC converter along with its phasor diagram. The winding arrangement and phasor diagrams for autotransformer employed in 18-pulse and 24-pulse AC-DC converters are shown in Fig. 5a and Fig. 5b respectively. The values of constants (as marked in Figs. 4-5) giving winding voltage as the fraction of input phase voltage for these configurations can be determined in a similar way and these are found as:

12-pulse converter:

K_{22}=0.2699; K_{23}=0.3094; K_{24}=0.5358; (9)

18-pulse converter:

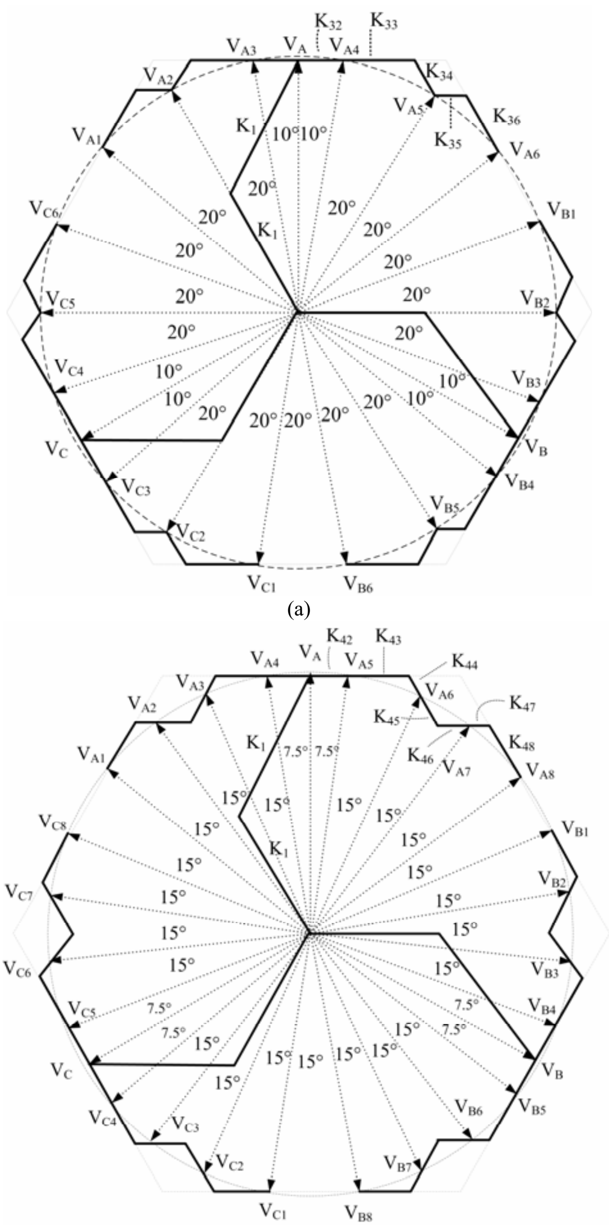

(a)

(b)

Fig. 5: Winding arrangement and phasor diagram of transformer for (a) 18-pulse and (b) 24-pulse non-isolated full-wave AC-DC converter.

K_{32}=0.1763; K_{33}=0.2577; K_{34}=0.1376; K_{35}=0.1376; K_{36}=0.2577. (10)

24-pulse converter:

K_{42}=0.1316; K_{43}=0.2149; K_{44}=0.0787; K_{45}=0.1520; K_{46}=0.1520; K_{47}=0.0787; K_{48}=0.2149. (11)

The VA rating of these autotransformers is calculated as [6]:

$$\text{VA rating} = 0.5 \sum (V_{\text{winding}}\, I_{\text{winding}}) \qquad (12)$$

III. MATLAB BASED SIMULATION

The proposed 6–pulse, 12-pulse, 18-pulse and 24-pulse non-isolated full-wave AC-DC converters are modeled and simulated in MATLAB environment along with SIMULINK and Power System Blockset (PSB) toolboxes. These full-wave AC-DC converter systems are fed from 415V, 50Hz AC supply. The load connected to the converter is considered of rating of a 5kW, 280V DC load. The value of source impedance used in these simulations is considered a practical value of 3%. The specifications of these converters are given in Appendix. Fig. 6 shows the MATLAB model of the 12-pulse full-wave AC-DC converter to improve various power-quality indices and Fig. 7 shows the model of the autotransformer winding arrangement used. The simulations of the 6-pulse, 18-pulse and 24-pulse full-wave AC-DC converters are also carried out in similar way for same supply and load conditions for comparing their performance.

IV. RESULTS AND DISCUSSION

The power quality indices obtained from simulations of 6-pulse, 12-pulse, 18-pulse and 24-pulse AC-DC converters at varying load are given in Table 1 The waveforms of input current along with supply voltage and output DC voltage and current are shown in Figs. 8-11.

Fig. 8: (a) shows the input AC waveforms with the output DC voltage and current waveforms of six-pulse converter configuration. The current is highly non-sinusoidal and the (6k±1) harmonics are prevalent which can be seen in Fig. 8(b) that shows input current waveform and its harmonic spectrum. The total harmonic distortion (THD) of AC mains current at full-load for this six-pulse converter is observed to be 25.9% which is much away

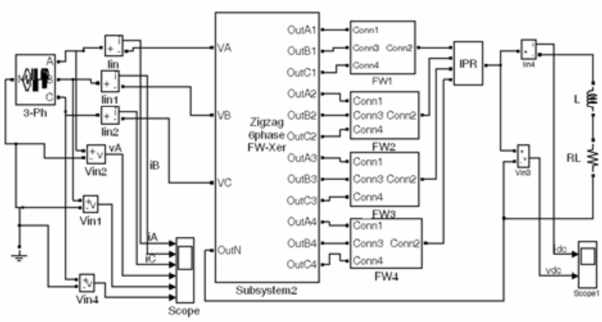

Fig. 6: MATLAB model of the 12-pulse full-wave AC-DC converter employing zigzag-autotransformer.

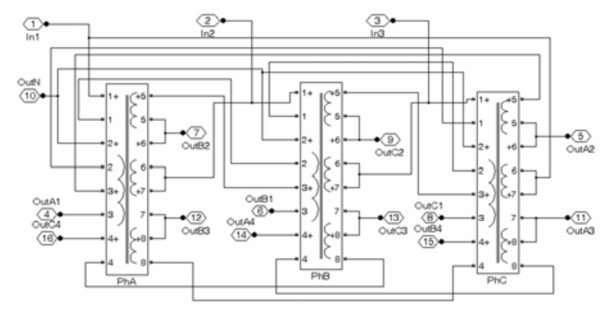

Fig. 7: MATLAB model of the proposed zigzag-Autotransformer for 12-pulse full-wave AC-DC converter.

from power quality standard (IEEE-519) requirements of 8%, like the other six-pulse AC-DC converters. However, it may be useful if it used with a passive or active filter to meet power quality requirement.

Fig. 9(b) shows the input current waveform and its harmonic spectrum for 12-pulse AC-DC converter. The THD of AC mains current is observed to be 10.96% and it has dominant 11th and 13th harmonics. Fig. 10(a) shows the input current waveform along with the supply phase voltage for 18-pulse AC-DC converter and 18-steps in a cycle can be clearly seen in these current waveforms. The input current has become close to sinusoidal and power factor (PF) has also improved. Moreover, the output DC voltage has 18 ripples of low peak-to-peak value. The THD of AC mains current is observed to be 6.01% at full-load as shown in Fig. 10(b). Table 1 shows that the value of THD varies in range 6.01% to 6.55% with varying load for this converter configuration and it meets IEEE-519 Standard requirements of power quality.

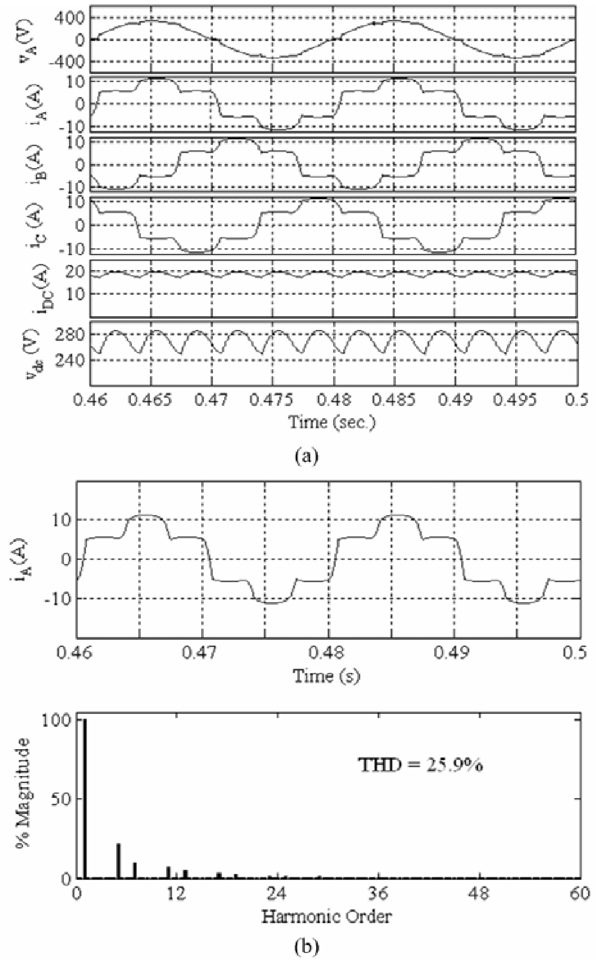

(a)

(b)

Fig. 8: Six-pulse full-wave AC-DC converter at full-load - (a) Input and output voltage and current waveform (b) Input current waveform and its harmonic spectrum.

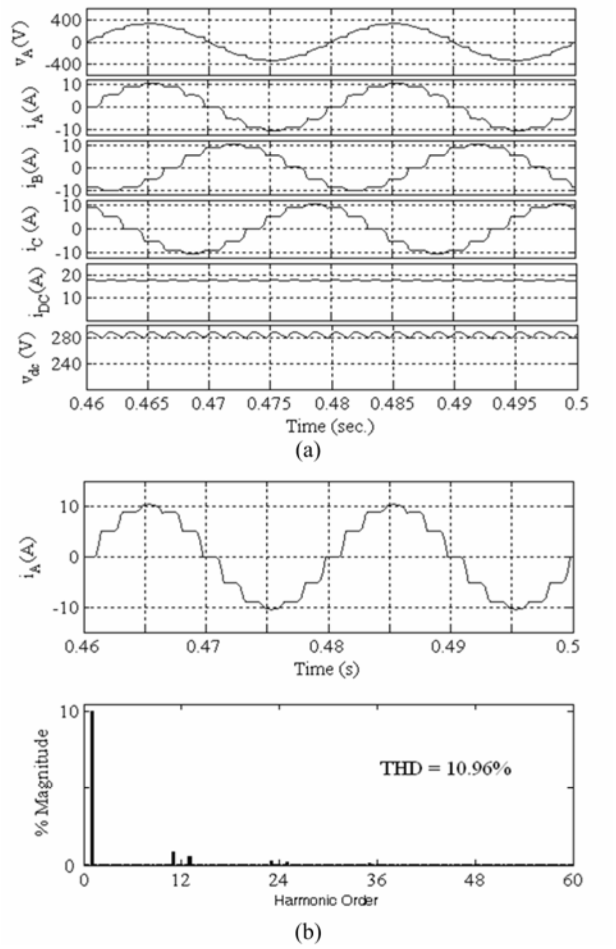

(a)

(b)

Fig. 9: Twelve-pulse full-wave AC-DC converter at full-load - (a) Input and output voltage and current waveform (b) Input current waveform and its harmonic spectrum.

Fig. 11(a) shows the input voltage and current waveforms along with output DC voltage and current waveforms of 24-pulse AC-DC converter. The waveforms of input current as well as output voltage has improved remarkably without employing any filter at front end. The input AC mains current waveform is almost sinusoidal and has dominant 23rd and 25th harmonics as shown in Fig. 11(b). Table 1 depicts that the THD variation of input current is 4.6% to 5.8% with the load and power factor is observed of order of 0.99.

The variation of THD of AC mains current and power factor with the load for these 6-pulse, 12-pulse, 18-pulse and 24-pulse full-wave non-isolated converter configurations are shown in Figs. 12 and 13 respectively. It clearly shows a remarkable improvement in power quality in the case of 24-pulse AC-DC converter.

Table 1 Comparison of power quality parameters of the different full-wave AC-DC converters

Sr. No.	Topology	% Load	%THD of V_A	AC Mains Current I_A (A)	% THD of I_A,	Distortion Factor	Displacement Factor	Power Factor	DC Voltage V_{dc}(V)	Load Current I_{dc} (A)	Ripple Factor %
1	6-pulse	20	1.982	1.587	28.19	0.9623	0.9973	0.9597	278.4	3.819	4.622
		40	3.265	3.111	27.6	0.9634	0.9953	0.9589	276.6	7.588	4.728
		60	4.379	4.609	27.0	0.9645	0.9934	0.9581	274.8	11.31	4.673
		80	5.359	6.08	26.44	0.9645	0.9915	0.9572	272.9	14.98	4.51
		100	6.274	7.529	25.9	0.9660	0.9898	0.9562	271.2	18.6	4.29
2	12-pulse	20	1.623	1.515	12.58	0.9921	0.9977	0.9898	289.1	3.559	1.221
		40	2.668	2.951	12.23	0.9922	0.9975	0.9898	288.1	7.094	1.248
		60	3.541	4.375	11.79	0.9925	0.9968	0.9893	287.1	10.6	1.20
		80	4.304	5.788	11.36	0.9927	0.9960	0.9887	286.1	14.09	1.12
		100	4.997	7.189	10.96	0.9928	0.9954	0.9882	285.2	17.55	1.031
3	18-pulse	20	1.303	1.558	6.522	0.9978	0.9910	0.9889	283.4	3.615	0.5575
		40	2.168	2.976	6.50	0.9977	0.9911	0.9888	282.5	7.205	0.5275
		60	2.902	4.39	6.384	0.9975	0.9933	0.9908	281.6	10.78	0.4655
		80	3.552	5.795	6.21	0.9974	0.9941	0.9915	280.8	14.32	0.4047
		100	4.123	7.192	6.015	0.9974	0.9944	0.9918	279.9	17.85	0.3538
4	24-pulse	20	1.363	1.531	5.797	0.9982	0.9991	0.9974	282.2	3.344	0.3344
		40	2.199	2.944	5.504	0.9982	0.9939	0.9989	281.8	7.189	0.3429
		60	2.875	4.352	5.176	0.9983	0.9987	0.9969	281.4	10.77	0.3245
		80	3.457	5.756	4.872	0.9982	0.9985	0.9967	281.0	14.34	0.2971
		100	3.97	7.155	4.593	0.9982	0.9984	0.9965	280.6	17.89	0.2694

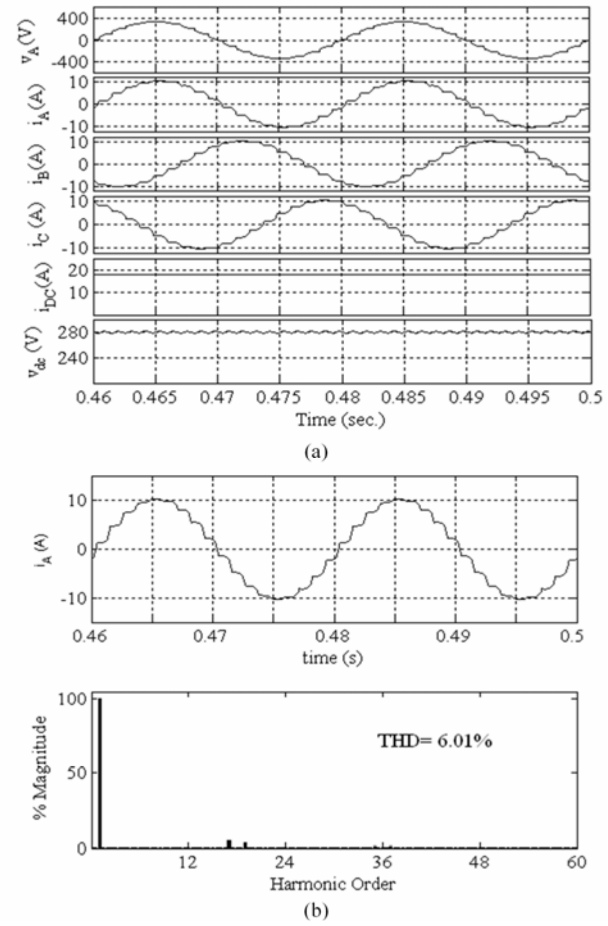

Fig. 10: Eighteen-pulse full-wave AC-DC converter at full-load - (a) Input and output voltage and current waveform (b) Input current waveform and its harmonic spectrum.

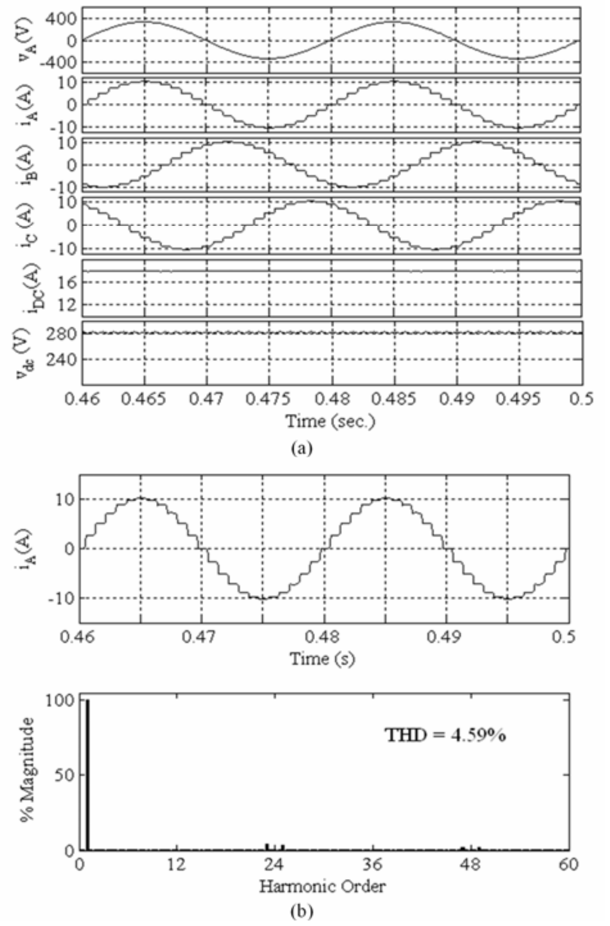

Fig. 11: Twenty four-pulse full-wave AC-DC converter at full load – (a) Input and output voltage and current waveform (b) Input current waveform and its harmonic spectrum.

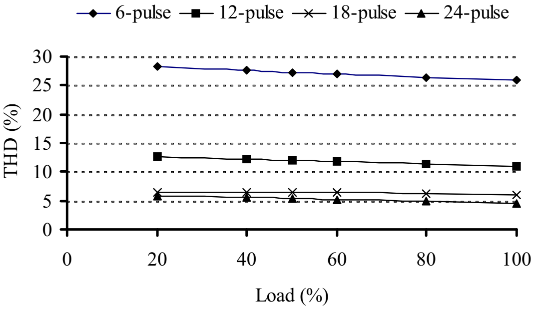

Fig. 12: Variation of input current total harmonic distortion with load.

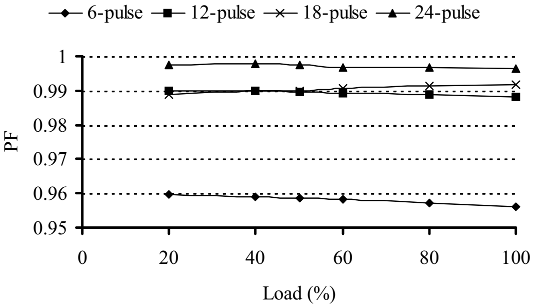

Fig. 13: Variation of power factor with load

The rating of these autotransformers for 6, 12, 18 and 24-pulse AC-DC converter configurations is estimated as 86.8%, 107.6%, 93.5% and 92.8% of the DC load rating respectively, which is much less than that of isolated topologies of full-wave AC-DC converters.

V. EXPERIMENTAL VALIDATION

To validate the design and modeling of these converters, a non-isolated full-wave 12-pulse AC-DC converter is developed in the laboratory for 7.5kW, 270V DC load. The same converter autotransformer is also employed for validating 6-pulse AC-DC converter configuration. The autotransformer design details of this developed autotransformer are given in Appendix. The number of turns and gauge of wire used for developed prototype are also given. Extensive tests are conducted on the prototype at varying loads and the power quality indices are recorded using power analyzer. The results for varying loads are given in Table 2. These recorded waveforms at full-load for 6-pulse and 12-pulse AC-DC converter configurations are shown in Figs. 14 and 15 respectively. The variation of THD of input current in simulation results in 6-pulse AC-DC converter is 25.9% to 28.19% similar to test results having input current THD variation in range of 27.0% to 28.3%. Similarly, in 12-pulse full-wave AC-DC converter the input current THD is observed from simulation and test results to vary from 10.96% to 12.58% and 11.3 to 12.6%, respectively. These hardware results are in line with the simulation results of these converters and validate the proposed design and model of this new class of full-wave non-isolated AC-DC converters.

The zigzag autotransformers used for these 6, 12, 18 and 24-pulse full-wave AC-DC converter systems have

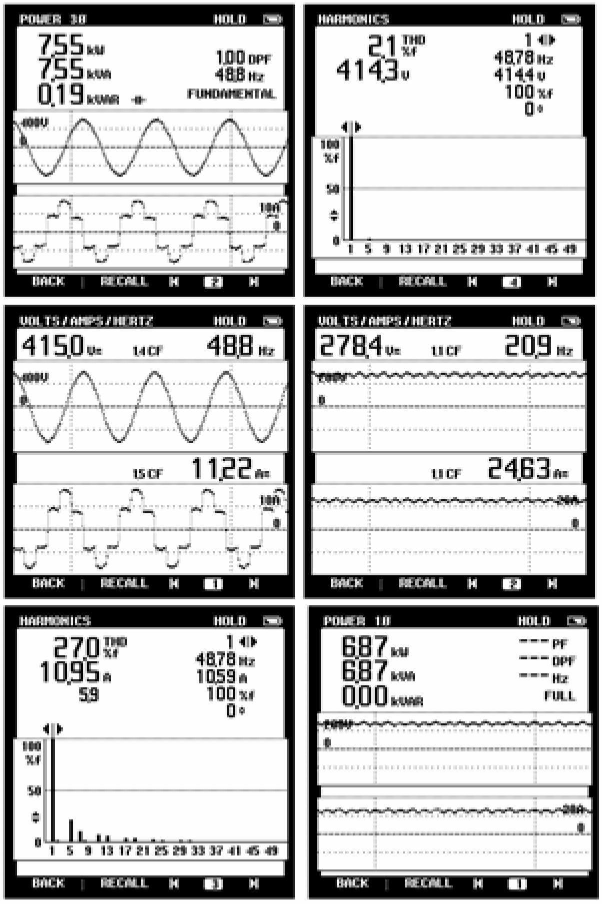

Fig. 14: Test results showing input and output waveforms and harmonic spectrum of input current/ voltage waveforms of proposed six-pulse AC-DC converter at full-load.

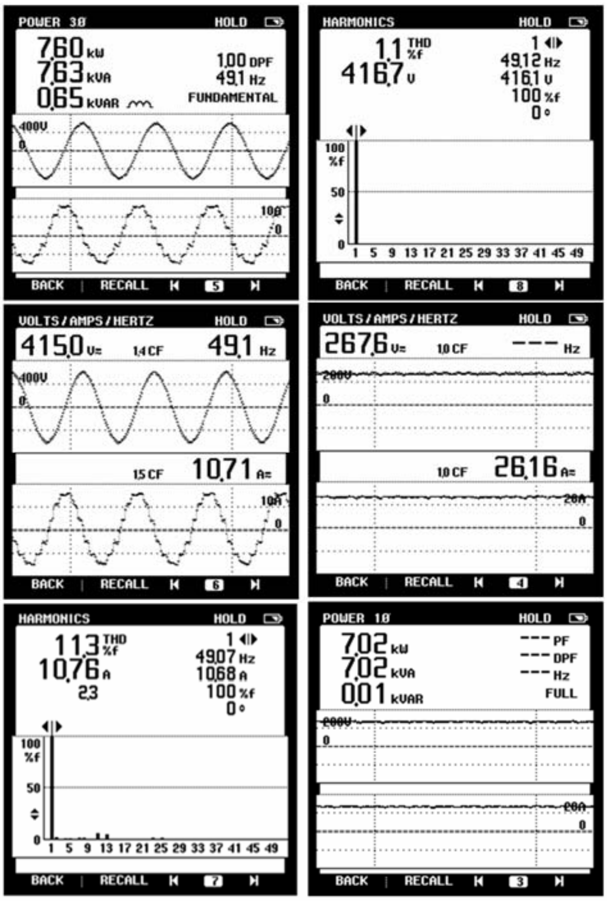

Fig. 15: Test results showing input and output waveforms and harmonic spectrum of input current/ voltage waveforms of proposed twelve-pulse AC-DC converter at full-load.

provided balanced outputs voltages for rectification and low voltage applications. Obtained results have demonstrated that the proposed 18 and 24-pulse full-wave AC-DC converters exhibit a high level performance with clean power characteristics.

The total harmonic distortion of input current is observed to be less than 8% at varying loads and meets IEEE-519 Standard power quality requirements. The output voltage ripple is of order less than 0.4% and input power factor is improved at varying loads thereby improving power quality at AC mains and output load.

Table 2 Test results for Comparison of power quality parameters of different AC-DC converters

Topology	Input Power (kW)	%THD of V_A	AC Mains Current I_A (A)	% THD of I_A,	Power Factor	DC Voltage (V_{dc})	Load Current I_{dc} (A)
6-pulse	1.13	2.0	1.64	28.3	0.9585	318.7	3.21
	1.95	2.0	2.85	27.9	0.9535	311.2	6.15
	4.01	2.0	6.09	27.4	0.9160	298.9	12.91
	5.91	1.8	8.79	27.3	0.9349	283.5	19.61
	7.55	2.1	11.22	27.0	0.9361	278.4	24.63
12-pulse	1.07	1.0	1.52	12.6	0.9793	296.7	3.51
	2.06	1.1	2.93	12.5	0.9781	290.5	6.95
	3.18	1.2	4.47	12.3	0.9897	285.8	10.98
	4.04	1.2	5.73	12.0	0.9808	280.1	14.07
	6.00	1.2	8.40	11.4	0.9878	275.7	20.56
	7.60	1.1	10.71	11.3	0.9872	267.6	26.16

VI. CONCLUSION

The zigzag autotransformers used for these 6, 12, 18 and 24-pulse full-wave AC-DC converter systems have formed a new class of AC-DC converters. These converters provide balanced outputs voltages for rectification and suits for lower secondary voltage applications. Obtained results have demonstrated that the proposed 18 and 24-pulse full-wave AC-DC converters exhibit a high level performance with clean power characteristics. The total harmonic distortion of input current is observed to be less than 8% at varying loads and meets IEEE-519 Standard power quality requirements. The output voltage ripple is of order less than 0.4% and input power factor is improved at varying loads thereby improving power quality at AC mains and output load.

APPENDIX

Converter Specifications:

AC Supply: 415V, 50Hz.
Source impedance: Z_s= j1.036ohms (=3%)
DC Load: 5kW, 280 V DC, L_{dc} =0.1mH

Transformer design details:

Flux Density: 0.8Tesla, Current Density: 2.3A/mm^2,
Core size: No. 7B
E-Laminations: Length=190mm, Width=124mm
I-Laminations: Length=190mm, Width= 32mm
Area of cross-section of core=48.76cm^2(6.40 cm X 7.62cm)

Autotransformer winding details-

Winding Number of turns Gauge of wire (SWG)

Winding	Number of	Gauge of wire
K_1*V_A	155	18
K_{22} *V_A	72	18
K_{23}* V_A	83	20
K_{24} *V_A	144	24

REFERENCES

[1] R. Wells, Static Power Converters, Robert Cunningham and Sons Ltd., Scotland, Great Britain, 1962.

[2] IEEE Standard 519-1992, IEEE Recommended Practices and Requirements for Harmonic Control in Electrical Power Systems, IEEE Inc., New York, 1992.

[3] J. Schaeffer, Rectifier Circuits: Theory and Design, New York: Wiley-Interscience, 1965.

[4] G. Seguier, Power Electronic Converters: AC/DC Conversion, New York: McGraw Hill, New York, 1986.

[5] R. W. Lye (Editor), Power Converter Hand Book-Theory, Design, Applications, Power Delivery Department, GE Canada, Ontario, March 1990.

[6] D. A. Paice, Power Electronic Converter Harmonics: Multipulse Methods for Clean Power, IEEE Press, 1996.

[7] Bin Wu, High-Power Converters and AC Drives, IEEE Press, Wiley-Interscience, 2006.

[8] R. Fuentes and L. Ternicien, “Harmonics Mitigation in High Current Multipulse controlled transformer Rectifiers”, in Proc. of Tenth IEEE Int. Conf. on Harmonics and Quality of Power, Vol. 1, 2002, pp. 189-195.

[9] A. J. Maslin, Sharon, G. F. Jones and Irwin “Electrical Induction Apparatus”, US Patent 2,307,527, Jan. 5, 1943.

[10] R. R. Brown, “Rectifier and DC Bus System Design for the Copper Electrowinning Industry”, IEEE Trans. on Ind. Appl., Vol. 26, No. 6, Nov./Dec., 1990, pp. 1116-1119.

[11] S. Miyairi, S. Iida, K. Nakata and S. Masubawa, “New method for reducing harmonics involved in input and output of rectifier with interphase transformer”, IEEE Trans. on Ind. Appl., Vol. 22 No. 5, Sep.- Oct., 1986, pp. 790-797.

[12] E. P. Wiechmann and P. E. Aqueveque, “Filterless high current rectifier for electrolytic applications”, in Proc. of IEEE conf. IAS 2005, Vol. 1, 2-6 Oct. 2005, pp. 198-203.

BIOGRAPHIES

Bhim Singh received his B. E. (Electrical) degree from the University of Roorkee, India in 1977 and his M. Tech. and Ph. D. degrees from the Indian Institute of Technology (IIT), New-Delhi, in 1979 and 1983, respectively. In 1983, He is a Professor in the Department of Electrical Engineering, IIT Delhi. His fields of interest include power electronics, electrical machines and drives, active filters and power quality. Prof. Singh is a Fellow of the Indian National Academy of Engineering (INAE), the Institution of Engineers (India) (IE (I)) and the Institution of Electronics and Telecommunication Engineers (IETE), a Life Member of the Indian Society for Technical Education (ISTE), the System Society of India (SSI) and the National Institution of Quality and Reliability (NIQR) and a Senior Member IEEE (Institute of Electrical and Electronics Engineers).

Sanjay Gairola received his B.E. degree in Electrical Engineering from Motilal Nehru National Institute of Technology, Allahabad in 1991 and his M. Tech. degree from Indian Institute of Technology (IIT), New Delhi, in 2001. He is presently working in the Department of Electrical Engineering, GCET, Greater Noida, India. He is a Life Member of the Indian Society for Technical Education (ISTE). His fields of interest include power quality, power electronics, electric machines and drives.

Asian Power Electronics Journal, Vol. 2, No. 1, Apr 2008

Application of Linear Switched Reluctance Motors to Precision Position Control

Wai-Chuen Gan[1], G. P. Widdowson[1], Michael S. W. Tam[1] and Norbert C. Cheung[2]

Abstract—This paper presents the application of linear switched reluctance motors (LSRMs) to precision position control. In general, a typical AC industrial servo system consists of a motion controller for torque, velocity and position loop control, a current tracking amplifier with a standard three phase output bridge and two current feedback sensors only, the motor to be controlled and a position feedback encoder. An LSRM is developed for the above typical AC servo system without any modifications on the hardware setup. The magnet free and possible high-temperature operation features allow LSRMs to replace linear permanent magnet (PM) motors in some special applications such as conveyor systems in an oven. On the other hand, the micrometer precision position control of LSRMs addressed in this paper is also new to literature.

Keywords – Switched Reluctance Motors, Linear Motor, Position Control

I. INTRODUCTION

[1]Linear switched reluctance motors (LSRMs) have never been a popular choice for direct-drive linear motion control systems; because they are difficult to control and their outputs have high force ripples. It is also due to the fact that the characteristic of the LSRM is highly dependent on its complex magnetic circuit, which is difficult to model, simulate, and control. There is not much in recent literature concerning high performance motion control of switched reluctance linear drive systems. It was only during recent years where we see a general surge of interest in the switched reluctance motor [1], [10]. This was mostly due to the advancement of power electronics and digital signal processing, and the continuous trend of simplifying the mechanics through advance control strategy.

In comparison to the linear AC permanent magnet (PM) motor or the linear AC induction motor, LSRMs possess many advantages that other actuators did not have. Firstly, manufacturing of the LSRM is simple, and it is very suitable for high precision travel over long distances. Secondly, unlike other types of motion actuators, mechanical couplings, lead/ball screws, magnets, and brushes are not required in LSRMs. Special mechanical adjustments or alignments are also not necessary either. Finally, in comparison to PM linear motors, the proposed actuator has a much simpler structure and is less expensive. It is also more robust, more fault tolerant, and has less overheating problems. Therefore, LSRMs are potential candidates for high performance linear motion drives.

Fig. 1 shows a general-purpose three-phase motor controller. The main component of the motion control system is a motion controller which performs the profile generation, as well as the torque, velocity and position loop control. The standard current-tracking amplifier consists of a three-phase output bridge (six IGBTs) and two current feedback sensors. Two Digital-to-Analog Converter (DAC) commands are received from the motion controller. On the other hand, the position encoder installed on the actuator feeds the incremental A, B and the index Z signals to the motion controller for the commutation and position control purposes. With the structure shown in Fig. 1, both three-phase linear/rotary PM/induction motors can be driven by only changing a proper control algorithm in the host controller but without any hardware reconfiguration. However, a hardware change is needed in order to drive a three-phase rotary/linear SRM. For example, the driving stage may be reconfigured as three asymmetric bridges [1] using three current sensors, requiring three DAC commands from the motion controller. This loss in generality for a three-phase LSRM drive is an obstacle to promote its popularity in industrial applications.

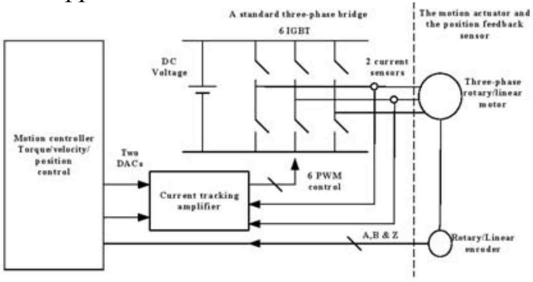

Fig. 1: Block diagram of a general-purpose three-phase motor controller.

In general, the applications of LSRMs are mainly focused on speed output control [1] such as transportation systems [10]. Researchers did not pay much attention to precision position control of LSRMs until [2], [3], [4]. To achieve high-precision position control using LSRMs, the key point is to apply a sophisticated force linearization scheme so that the control of a highly nonlinear LSRM can be as easy as that of a DC motor. In addition, the inner current loop and the outer velocity and position loops are also required to be properly designed so as to provide an accurate position tracking response.

An LSRM control system for high-precision position accuracy was developed by the authors and the results can be found in [2], [3], [4]. In this paper, a sophisticated force linearization algorithm is first proposed for the LSRM. Then with a proper reconfiguration of the three-phase

---

The paper first received 18 Jun 2007 and in revised form 13 Mar. 2008
Digital ref. AI70201168

[1]Motion Group, ASM Assembly Automation Hong Kong Ltd., Kwai Chung, NT, Hong Kong SAR, China. Email: wcgan@asmpt.com
[2]Department of Electrical Engineering, The Hong Kong Polytechnic University, Hung Hom, Kowloon, Hong Kong SAR, China. Email: eencheun@polyu.edu.hk

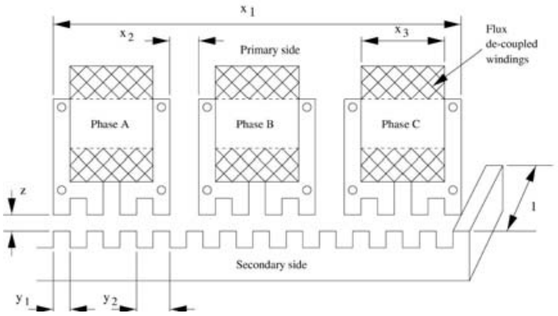

Fig. 2: LSRM design schematic.

motor windings and the insertion of three diodes, the LSRM can be driven by a standard three-phase bridge inverter with two current feedback sensors only. Therefore, an LSRM system, with direct compatibility to existing AC servo motors, can be developed with the proposed force linearization and novel driving schemes. The only change for the proposed system is the easily reconfigurable control software inside the motion controller.

The paper is organized as follows. Section II gives a brief review on the construction and development of the LSRM. In Section III, the proposed force linearization algorithm for the LSRM is addressed. In Section IV, the three-phase motor winding reconfiguration and the novel winding excitation scheme are described, so that the proposed LSRM can be driven by a standard three-phase bridge inverter. The system integration and experimental results are shown in Section V to validate the proposed LSRM system. Some concluding remarks are given in Section VI.

II. REVIEW ON THE CONSTRUCTION AND MODELING OF THE LSRM

The novel actuator design is based on switched reluctance technology [3]. The magnet-free structure makes this actuator particularly suitable for harsh environments such as high temperature and high pressure. The flux de-coupled rotor arrangement leads a more simple motor model because there are no mutual inductances between windings. Fig. 2 shows the design schematic of the LSRM system.

The motor is integrated on a precision linear motion guide. The tracking guide and the core of the windings are laminated with 0.5mm silicon-steel plates. Table 1 shows the design parameters of the proposed LSRM. The switched reluctance linear drive system has a highly nonlinear characteristic due to its nonlinear flux behavior. The following is the nonlinear mathematical model of the LSRM:

$$\upsilon_j = R_j i_j + \frac{\partial \lambda_j\left(x, i_j\right)}{\partial x}\frac{dx}{dt} + \frac{\partial \lambda_j\left(x, i_j\right)}{\partial i_j}\frac{di_j}{dt} \qquad (1)$$

$$f_e = \sum_{j=1}^{3} \frac{\partial \int_0^{i_j} \lambda_j\left(x, i_j\right) di_j}{\partial x} \qquad (2)$$

$$f_e = M\frac{d^2x}{dt^2} + B\frac{dx}{dt} + f_l \qquad (3)$$

where v_j , i_j , R_j and λ_j are the phase voltage, phase current, phase resistance and phase flux linkage respectively, x is the travel distance, f_e is the generated electromechanical force, f_l is the external load force, M and B are the mass and the friction constant respectively.

Table 1: Design parameters of the LSRM.

Power output	100W
Traveling distance	300mm
Maximum load	5kg
Pole width	5mm(y_1)
Pole pitch	10mm(y_2)
Coil separation	8.333mm(x_2)
Winding width	15mm(x_3)
Track width	25mm(l)
Air gap width	0.4mm(z)
Aligned phase inductance	19.8mH
Unaligned phase inductance	11.4mH

III. FORCE LINEARIZATION SCHEME FOR LRM

The most difficult part in controlling an LSRM is how to compensate the nonlinear force generation function so that the input command current is directly proportional to the output force. There are many different methods to perform the force linearization algorithm [1], [10-11] and the most common way is to employ the force-position-current look-up table scheme. However, the databases of the look-up tables need to be remeasured for different LSRMs, a procedure that may not be acceptable to mass production of LSRM systems with different dimensions and force constant requirements. Recently, exact force linearization for LSRMs was developed such that a closed form solution can be given for different LSRMs [11]. The required parameters are only the change of the inductance values from unaligned to aligned position and some mechanical dimensions, which are easy to obtained in comparison to the creation of a three-dimensional look-up table. The exact force linearization scheme will be implemented in this proposed LSRM system.

Basically, the exact force linearization scheme can be further divided into two stages as shown in Fig. 3. The first stage is to determine which phase or two phases can be excited at different locations and force input within a pole pitch. The two phase excitation algorithm can definitely smooth the force ripples during the transition

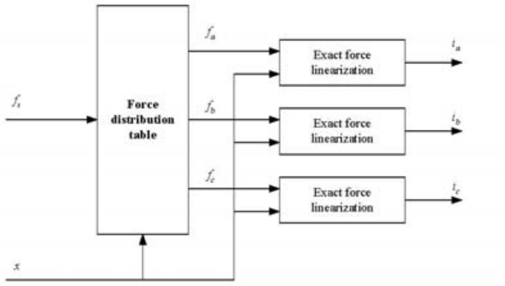

Fig. 3: Two-stage force linearization scheme.

Table 2: Current excitation table for a single pole pitch

Region	Range(mm)	For +ve force	For –ve force
1	0-1.667	I_b	I_c, I_a
2	1.667-3.333	I_b, I_c	I_a
3	3.333-5	I_c	I_a, I_b
4	5-6.667	I_c, I_a	I_b
5	6.667-8.333	I_a	I_b, I_c
6	8.333-10	I_a, I_b	I_c

period form one region to another [10]. Table 2 shows the current excitation table for the proposed LSRM.

After the phase excitation sequence is found, the next stage is to perform the force linearization algorithm. The basic idea of the proposed algorithm is to evaluate the required current according to the input position and the force command. The exact force-position-current inverse functions for single-phase and two-phase excitation are given as follows [11].

For single-phase excitation:

$$I_a = \sqrt{\frac{-k_t f_a}{\sin\left(\frac{2\pi x}{y_2}\right)}}\,,$$

$$I_b = \sqrt{\frac{-k_t f_b}{\sin\left(\frac{2\pi x}{y_2}-\frac{2\pi}{3}\right)}}\,,$$

$$I_c = \sqrt{\frac{-k_t f_c}{\sin\left(\frac{2\pi x}{y_2}+\frac{2\pi}{3}\right)}}$$

For two-phase excitation:

$$I_a = \sqrt{\frac{-k_t f_a \sin\left(\frac{2\pi x}{y_2}\right)}{\sin^2\left(\frac{2\pi x}{y_2}\right)+\sin^2\left(\frac{2\pi x}{y_2}+\frac{2\pi}{3}\right)}}$$

or

$$I_a = \sqrt{\frac{-k_t f_a \sin\left(\frac{2\pi x}{y_2}\right)}{\sin^2\left(\frac{2\pi x}{y_2}\right)+\sin^2\left(\frac{2\pi x}{y_2}-\frac{2\pi}{3}\right)}}\,,$$

$$I_b = \sqrt{\frac{-k_t f_b \sin\left(\frac{2\pi x}{y_2}-\frac{2\pi}{3}\right)}{\sin^2\left(\frac{2\pi x}{y_2}-\frac{2\pi}{3}\right)+\sin^2\left(\frac{2\pi x}{y_2}\right)}}$$

or

$$I_b = \sqrt{\frac{-k_t f_b \sin\left(\frac{2\pi x}{y_2}-\frac{2\pi}{3}\right)}{\sin^2\left(\frac{2\pi x}{y_2}-\frac{2\pi}{3}\right)+\sin^2\left(\frac{2\pi x}{y_2}+\frac{2\pi}{3}\right)}}\,,$$

$$I_c = \sqrt{\frac{-k_t f_c \sin\left(\frac{2\pi x}{y_2}+\frac{2\pi}{3}\right)}{\sin^2\left(\frac{2\pi x}{y_2}+\frac{2\pi}{3}\right)+\sin^2\left(\frac{2\pi x}{y_2}\right)}}$$

Or

$$I_c = \sqrt{\frac{-k_t f_c \sin\left(\frac{2\pi x}{y_2}+\frac{2\pi}{3}\right)}{\sin^2\left(\frac{2\pi x}{y_2}+\frac{2\pi}{3}\right)+\sin^2\left(\frac{2\pi x}{y_2}-\frac{2\pi}{3}\right)}}\,,$$

where f_a , f_b and f_c are the three-phase force inputs, x is the current position, y_2 is the pole pitch, and k_t is the force constant that can be calculated from the change of inductance value from unaligned to aligned position and the mechanical dimensions of the LSRM [3].

Traditionally, three independent current commands i_a , i_b and i_c defined in (4) will be tracked using three asymmetric bridge amplifiers. However, in this paper, another novel driving scheme is proposed such that the three independent phase commands can still be tracked using a standard three-phase bridge with only two current feedback sensors and two input commands.

IV. THREE-PHASE BRIDGE INVERTER FOR LSRM

In general, SRMs are driven by special inverters such as an asymmetric bridge, a unipolar converter and a C-Dump converter [1], [6], [7]. There was previously no interest in designing a SRM driver using a standard three-phase bridge [8], [9]. The advantages of using a standard three-phase bridge are the reduction in the size and cost of the motor driver, the reduction in stray inductance and EMI problem, and the direct compatibility to other three-phase motors. The dwell angle limitation in [8] is not suitable for the current tracking control in an accurate position control system. The inverter topology and the motor winding configuration employed in this paper are based on [9] with modifications on the phase current excitation sequence for the proposed LSRM.

Fig 4 shows a general three-phase bridge inverter for a three-phase linear/rotary PM/induction motor. The current loop controllers such as PI compensators are assumed to be appropriately designed or well-tuned so that the closed loop bandwidth is adequate for an accurate current command tracking. As the summation current of a three phase system is equal to zero, i.e. $I_r + I_s + I_t = 0$, the control of three phase current is equivalent to the control of two phase currents, I_r and I_s , and the third current is slave to the other two as $I_t = -I_r - I_s$. Hence, only two current sensors are required for feedback purposes. However, the zero current summation assumption is not valid for SRM in general.

Electromechanical force generation in the LSRM is a function of the current magnitude only. By making use of this unipolar current driven feature, the LSRM can still be driven by the standard three-phase bridge inverter as shown in Fig. 4 with a proper motor winding reconfiguration. Firstly, the diode insertion in each phase is to guarantee unipolar current flowing, i.e. $I_a > 0$, $I_b > 0$ and $I_c > 0$. Secondly, the delta connection of the three-phase windings is to guarantee $I_r + I_s + I_t = 0$ with the current relations shown below:

$$I_r = I_a - I_c, I_s = I_b - I_a, I_t = I_c - I_b. \qquad (5)$$

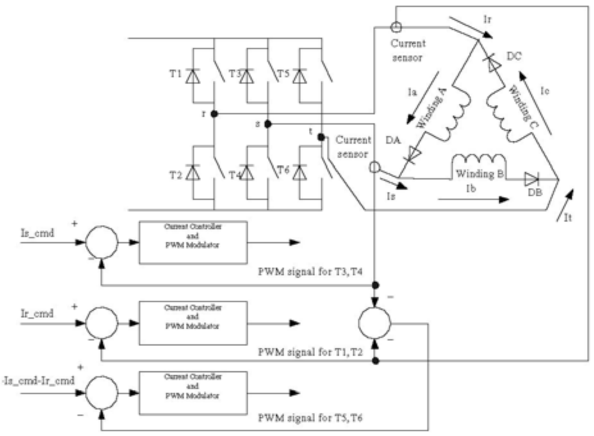

Fig. 4: Three-phase bridge inverter for LSRM.

Table 3: Current excitation table by using I_r and I_s only

Region	For +ve force	For –ve force
1	I_r=0, I_s= I_b	I_r= I_a - I_c, I_s= - I_a
2	I_r= - I_c, I_s= I_b	I_r= I_a, I_s= - I_a
3	I_r= - I_c, I_s= 0	I_r= I_a, I_s= I_b - I_a
4	I_r= I_a - I_c, I_s= - I_a	I_r=0, I_s= I_b
5	I_r= I_a, I_s= - I_a	I_r= - I_c, I_s= I_b
6	I_r= I_a, I_s= I_b - I_a	I_r= - I_c, I_s= 0

Finally, with (5), the magnitude of I_a, I_b and I_c can be independently controlled by two phase current I_r and I_s. The detailed excitation table is shown in Table 3.

In summary, with the help of the delta motor windings reconfiguration, the insertion of the diodes and the two phase command current excitation table, the LSRM can be driven by a standard three-phase bridge with only two current sensors for feedback purposes. Hence, the proposed LSRM is now ready for connection to any general-purpose three-phase motor driver without any hardware change.

V. SYSTEM INTEGRATION AND EXPERIMENTAL RESULTS

The proposed LSRM system was tested using a standard AC servo system with a commercial motion controller, a current-tracking amplifier and a linear optical encoder. Fig. 6 and Fig. 5 show the block diagram of the whole LSRM system. In Fig. 6, the commercial motion controller is from ACS-Tech80 Inc. [12], and was responsible for the profile generation, standard velocity and position loop control with velocity and acceleration feed-forward. In addition, the motion controller was defined as a DC servo control axis with one DAC output and position encoder input. The proposed force linearization scheme defined in Table 2, Table 3 and (4) was implemented by a dSPACE 1102 fast control prototyping system [13]. The inputs are the force command from the motion controller and the current position, while the outputs are two current commands for the current-tracking amplifier. It should be emphasized that there is no need to implement the force linearization algorithm for LSRMs by a separate DSP. If the low level DSP program of the motion controller can be accessed, the proposed algorithm can always be embedded within the same DSP, using look-up tables for the complex mathematical functions. The above experimental setup was just for the verification of the proposed algorithm.

Fig. 5 shows the experimental setup for the current-tracking amplifier, the LSRM and the linear optical encoder. The commercial current-tracking amplifier is from Copley Control Inc. [14] which accepts two input commands and provides three-phase output currents with the constraint $I_r + I_s + I_t = 0$. As described in Section IV, the LSRM is connected as a delta connection with three diodes insertion; therefore, a standard three phase bridge can still drive the proposed LSRM without any constraints.

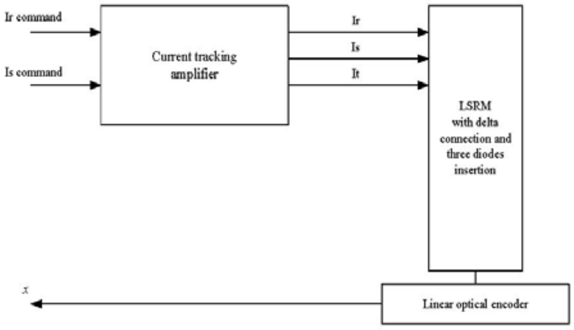

Fig. 5: Amplifier and LSRM setup.

To test the performance of the proposed system, a typical 20mm third order position profile with maximum acceleration = 0.4g and maximum velocity = 0.3m/s, was used as the test signal. Fig. 7 and 8 show the position error responses. Fig. 7 shows the position error for two cycles of profile tracking; it can be observed that the maximum dynamic error is around 200 counts = 100μm (the resolution of the encoder used is 0.5μm = 1 count). Furthermore, Fig. 8 shows the maximum steady state error of the position profile tracking, which is equal to 2 counts = 1μm. The accurate position tracking response demonstrates the effectiveness of the proposed force linearization scheme.

The current tracking signals are also examined to verify the proposed driving scheme introduced in Section IV. Fig. 9 and Fig. 10 show respectively the current signals present at the amplifier phase terminal and the motor phase winding. A bipolar current signal can be found at the driver phase terminal as shown in Fig. 9 while a unipolar current is present at the motor winding due to the diode insertion.

The captured waveforms show that the proposed driving scheme can drive an LSRM with a standard three-phase bridge and two current feedback sensors only. In summary, the promising experimental results show that the proposed LSRM system can be used as an accurate position tracking system.

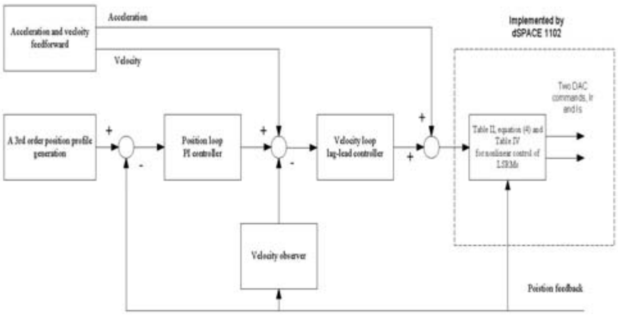

Fig. 6: Motion controller for the proposed system.

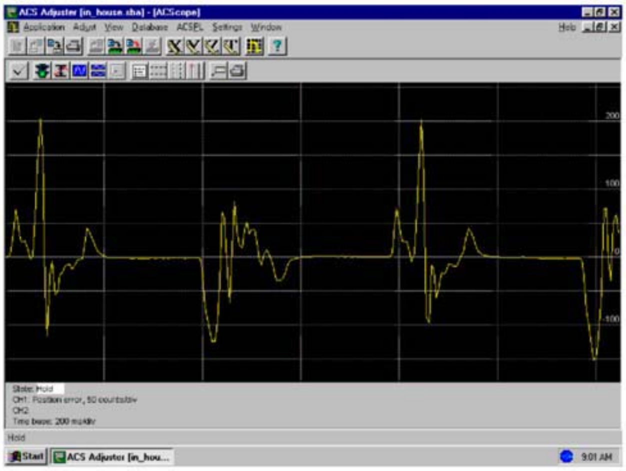

State: Hold
CH1: Position error, 50 counts/div
CH2
Time base: 200 ms/div
Hold

Fig. 7: Dynamic error position
(y-axis: 50 counts per division).

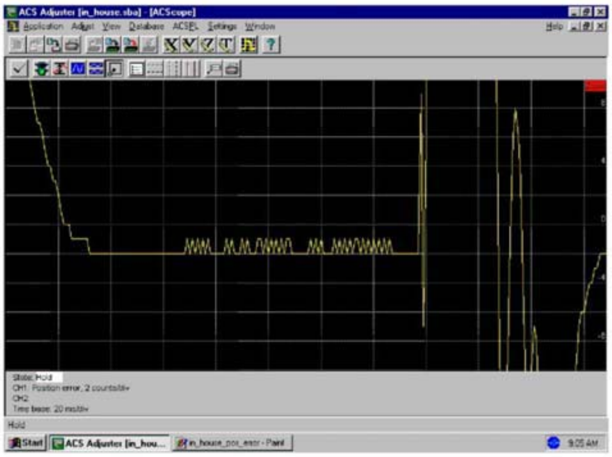

State: Hold
CH1: Position error, 2 counts/div
CH2
Time base: 20 ms/div
Hold

Fig. 8: Steady state error position
(y-axis: 2 counts per division).

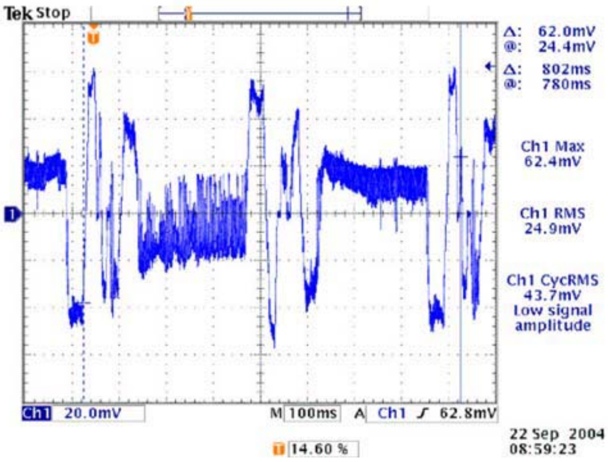

Fig. 9: Bipolar current signal at the driver phase terminal, I_r (10mv=1A).

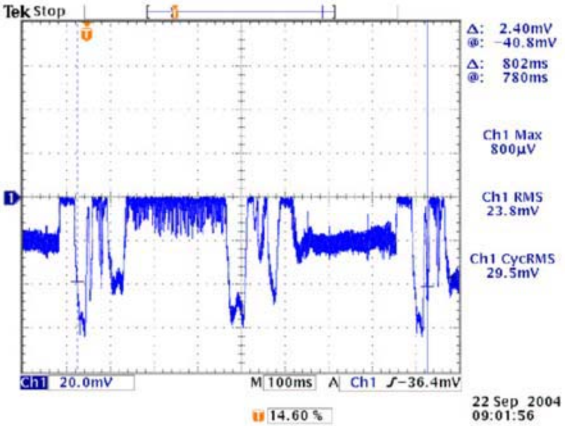

Fig. 10: Uniploar current signal at the motor phase winding, I_a (10mv=1A).

VI. CONCLUSIONS

In this paper, a low-cost LSRM for position control application is designed, manufactured and verified. The developed LSRM can be driven by a standard three-phase bridge inverter with the proposed driving scheme introduced in Section IV; therefore, the size of the overall driver can be reduced, the EMI problem can be alleviated and the cost of the whole system can be minimized. The feasibility and the effectiveness of the proposed position sensor and the inverter are supported by the experimental results shown in Section V.

In conclusion, the LSRM described in this paper is robust, reliable and low-cost. The proposed LSRM can work with the general-purpose three-phase motor controller without any hardware change. Therefore, this LSRM is a potential candidate for the replacement of linear three-phase PM/induction motors in special applications that require the features of magnet-free and high temperature operation. The popularity of applying LSRMs in industrial

ACKNOWLEDGMENT

The authors would like to thank ASM Assembly Automation Hong Kong Ltd. for the support on this investigation.

REFERENCES

[1] T. J. E. Miller, "Switched reluctance motors and their control", Clarendon Press, 1993.

[2] N. C. Cheung, "A robust and low-cost linear motion system for precision manufacturing automation, Vol. 1, Oct. 2000, pp. 40-45.

[3] W. C. Gan and N. C. Cheung, "Design of a linear switched reluctance motor for high precision applications," IEEE International Electric Machines and Drives Conference, Jun. 2001, pp. 701-704.

[4] W. C. Gan and N. C. Cheung, "Development and control of a low-cost linear variable-reluctance motor for precision manufacturing automation, Vol. 8, No. 3, Sep. 2003, pp. 326-333.

[5] J. Corda and E. Skopljak, "Linear switched reluctance actuator," Proc. of the Sixth International Conference on Electrical Machines and Drives, Saint Nazaire, Sep. 1993, pp. 535-539.

[6] C. Pollock and B. W. Williams, "A unipolar converter for a switched reluctance motor," IEEE Trans. on Industrial Electronics, Vol. 26, No. 2, 1990, pp. 222-228.

[7] A. M. Hava, V. Blasko and T. A. Lipo, "A modified C-dump converter for variable-reluctance machines," IEEE Trans. on Industrial Electronics, Vol. 28, No. 5, 1992, pp. 1017-1022.

[8] L. Xu and J. Bu, "Analysis of a novel converter topology for switched reluctance machine drives," Proc. of the IEEE International Conference on Power Electronics, Drives & Energy Systems for Industrial Growth, Vol. 2, 1998, pp. 640-645.

[9] A. C. Clothier and B. C. Mecrow, "The use of three phase bridge inverters with switched reluctance drives," Eighth International Conference on Electrical Machines and Drives, 1997, pp. 351-355.

[10] R. Krishnan, Switched Reluctance Motor Drives: Modeling, Simulation, Analysis, Design, and Applications, CRC Press, 2001.

[11] F. Horrami, P. Krishnamurthy and H. Melkote, Modeling and Adaptive Nonlinear Control of Electric Motors, Springer Verlag, 2003.

[12] ACS-Tech80 website: http://www.acs-tech80.com/

[13] dSPACE website: http://www.dspace.com/

[14] Copley website: http://www.copleycontrols.com/

BIOGRAPHIES

Wai-Chuen Gan received the B.Eng. degree (with first-class honors and the academic achievement award) in electronic engineering, and the M.Phil. and Ph.D. degrees in electrical and electronic engineering from Hong Kong University of Science and Technology. Clear Water Bay. Hong Kong, in 1995. 1997. and 2001. respectively. Form 1997 to 1999. he was a Motion Control Application Engineer at ASM Assembly Automation, Ltd.. Hong Kong. He rejoined the same company in 2002 and is now a Staff Engineer in the R&D Motion group. He is a senior IEEE member and his current research interests include robust control of AC machines, power electronics, design and control of linear switched reluctance motors and linear permanent magnet motors.

G. P. Widdowson is a Chief Engineer at ASM Assembly Automation. He received his PhD in Electrical engineering from the Machines and Drives Group. University of Sheffield, UK, in 1992. He has authored and co-authored over 30 technical paper for journals and has 13 US patents in various fields of engineering. His academic interests include, motor design, sensor design, mechatronics and precision engineering.

Michael S. W. Tam obtained his B.Eng degree from the Sunderland University in 1991. After his graduation, he worked in the High Power Manufacturer as an electronic engineer for two vears and was responsible for the design of electronic ballast and UPS. He then joins the R&D motion group of ASM Assembly Automation company and is now a Principle Engineer and leading the motor driver group. He also got a master degree from The Hong Kong Polytechnic University in 2005. His research interests include DSP motion control systems and power drives.

Norbert C. Cheung received his BSc, MSc, and PhD from the University of London, University of Hong Kong, and University of New South Wales in 1981. 1987. and 1995 respectively. His research interests are motion control, actuators design, and power electronic drives. He is now an Assistant Professor in the Department of Electrical Engineering of the Hong Kong Polytechnic University.

Asian Power Electronics Journal, Vol. 2, No. 1, Apr 2008

Voltage and Frequency Controller for a Small Scale Wind Power Generation

Bhim Singh[1] and Gaurav Kumar Kasal[1]

Abstract – This paper deals with the control of voltage and frequency of a wind turbine driven isolated asynchronous generator (IAG). The proposed voltage and frequency controller consists of an IGBT (Insulated Gate Bipolar Junction Transistor) based voltage source converter along-with a battery energy storage system at its DC bus. The controller is having bidirectional flow capability of active and reactive powers by which it controls the system voltage and frequency with variation of consumer loads and the speed of a wind turbine. For a constant frequency operation, the asynchronous generator operates at almost constant speed (small range of slip). In addition to voltage and frequency control it is also having capability of harmonic elimination and load balancing. The proposed electro-mechanical system with its controller is modeled and simulated in MATLAB using Simulink and PSB (Power System Block-set) toolboxes.

Key-words – Isolated Asynchronous Generator, Wind Energy Conversion System, Battery Energy Storage System, Voltage and Frequency Controller.

I. INTRODUCTION

There has been an exponential increase in the energy demand during the last few decades, which has accelerated the depletion of the world fossil fuels. Environmental concerns and international policies are supporting new interests and developments of small scale renewable power generation [1, 2]. It is reported in the literature that in small scale wind and hydro power generation, a capacitor excited squirrel cage asynchronous generator (CEAG) which is also known as a self excited induction generator (SEIG) is a most suitable candidate because of its low cost, robustness, less maintenance and high power density (W/kg) and can be used for single phase and three phase power distribution [3, 4]. However the magnitude and frequency of the generated voltage depends upon the rotor speed, the amount of excitation and the load (magnitude and power factor).

As a renewable energy source the wind power is one of the prominent energy sources and various types of electrical generators such as synchronous generator, asynchronous generators in squirrel cage and slip ring rotor construction [3-6], reluctance generators [7] have been reported in stand alone applications. However, because of simplicity of the squirrel cage asynchronous generator it is widely used and recommended for wind power generation. In the literature, various attempts have also been made to develop the mathematical models in steady state, dynamic and during the period of transient for isolated wind energy conversion system using capacitor excited asynchronous generators [8-10].

In this paper, a voltage and frequency (VF) control scheme is proposed for an isolated capacitor excited asynchronous generator (CEAG) driven by wind turbine. The proposed control scheme presented in this paper optimized the cost of the system by requiring reduced number of current sensors along with giving the faster response of the controller compared to scheme presented in ref [10]. The performance of the controller is investigated in different dynamic conditions such as wind speed variation and application of balanced/unbalanced non-linear loads in MATLAB using Simulink and PSB toolboxes. The proposed voltage and frequency controller is realized using IGBT (Insulated Gate Bipolar Junction Transistor) based voltage source converter (VSC) along with battery energy storage system (BESS) [11-13] at its DC bus and functioning as a load balancer and a harmonic eliminator.

II. SYSTEM CONFIGURATION AND PRINCIPLE OF OPERATION

Fig. 1 shows the schematic diagram of the proposed CEAG system driven by wind turbine along-with its controller, excitation capacitor and consumer loads. The proposed controller consists of an IGBT based voltage.

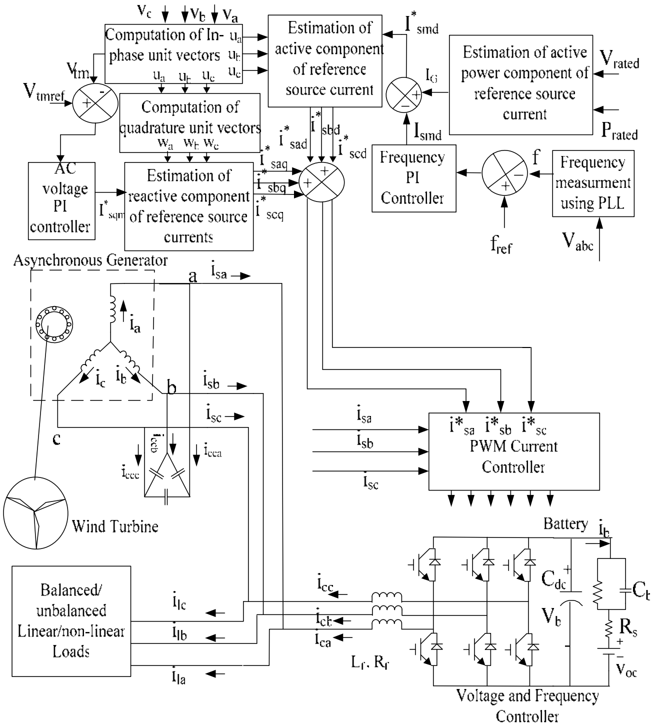

Fig.1:Schematic diagram of VF controller for an isolated asynchronous generator driven by wind turbine

---

The paper first received 23 Oct 2007 and in revised form 31 Mar 2008.
Digital ref: AI70201180

[1] Department of Electrical Engineering, Indian Institute of Technology, New Delhi-110016, India. E-mail:bhimsinghr@gmail.com, gauravkasal@gmail.com

There is a source converter along-with a battery energy storage system at its DC bus. The delta connected capacitor bank is used to generate the rated voltage at no load while additional demand of the reactive power is met by the controller. The proposed controller is having bidirectional flow capability of active and reactive powers and it controls the voltage by controlling the reactive power while the frequency is controlled by the active power control.

The basic principle of its operation is that at high wind speeds the generated power is also high and accordingly for frequency regulation the total generated power should be consumed otherwise difference of mechanical and electrical power is stored in the revolving components of the generator and by which the speed of the generator and in turn it increases the output frequency. Therefore this additional generated power is used to charge the battery to avoid the frequency variation as stated above. During deficiency of the generated power, when there is an insufficient wind power to meet the consumer demand an additional required active power is supplied by the battery to the consumer loads. In this manner, the battery energy storage system based voltage and frequency controller also provides load leveling and frequency regulation.

III. CONTROL STRATEGY

As shown in Fig. 1, the control strategy of the proposed voltage and frequency controller is based on the generation of reference source currents. Three-phase reference source currents are having two components one is in phase or active power component (i^*_{sad}, i^*_{sbd}, i^*_{scd}) for regulating the frequency while other one is in quadrature or reactive power component (i^*_{saq}, i^*_{sbq}, i^*_{scq}) for regulating the voltage. For generating the active power component of reference source current, the output of the frequency PI (Proportional-Integral) controller (I_{smd}) is compared with the rated generator current (I_G) and the difference in these two currents is considered as an amplitude of in-phase component of reference current (I^*_{smd}). The multiplication of I^*_{smd} with in-phase unit amplitude templates (u_a, u_b and u_c) yields the in-phase component of reference source currents. These templates (u_a, u_b and u_c) are three-phase sinusoidal functions, which are derived by dividing the filtered AC voltages v_a, v_b and v_c using band pass filter by their amplitude V_t. To generate the quadrature component of reference source currents another set of sinusoidal quadrature unity amplitude templates (w_a, w_b, w_c) is obtained from in-phase unit templates (u_a, u_b and u_c). The multiplication of these components with output of AC voltage PI controller (I^*_{smq}) gives the quadrature or reactive power component of reference source currents. The sum of instantaneous quadrature and in-phase component of source currents is the reference source currents (i^*_{sa}, i^*_{sb} and i^*_{sc}), and these are compared with the sensed source currents (i_{sa}, i_{sb}, i_{sc}). These current error signals are amplified and amplified signals are compared with fixed frequency triangular carrier wave to generate the PWM signals for switching of the devices of the voltage source converter used in the controller.

Basic equations of the control scheme for BESS based voltage and frequency controller is given as follows.

A. In Phase Component of Reference Source Currents

In-phase component of reference source current is calculated by taking the difference of rated generator current (I_G) and output of the frequency PI controller (I_{smd}). The frequency error is defined as

$$fer(n) = fref(n) - f(n) \tag{1}$$

where f_{ref} is reference frequency (50Hz in present system) and f is the frequency of the voltage of an asynchronous generator. The instantaneous value of 'f' is estimated using PLL (Phase Locked Loop) on the terminal voltage.

At the nth sampling instant, the output of the frequency PI controller (I_{smd}) is as

$$I_{smd(n)} = I_{smd(n-1)} + K_{pf}\{f_{er(n)} - f_{er(n-1)}\} + K_{if} f_{er(n)} \tag{2}$$

The rated current of the generator is calculated as

$$I_G = \sqrt{2}\,(P_{rated})/(\sqrt{3}\,V_{rated}) \tag{3}$$

where P_{rated} and V_{rated} are rated power and rated line voltage of the asynchronous generator.

By eqs. (2) and (3) at the nth sampling instant, the amplitude of active current component is

$$I^*_{smd} = I_{G(n)} - I_{smd(n)} \tag{4}$$

The instantaneous line voltages at the asynchronous generators terminals (v_a, v_b and v_c) are filtered using band pass filter (BPF) which has resulted in sinusoidal voltages and their amplitude is computed as

$$V_t = \{(2/3)\,(v_a^2 + v_b^2 + v_c^2)\}^{1/2} \tag{5}$$

The unity amplitude templates are having instantaneous value in phase with instantaneous voltage (v_a, v_b and v_c), which are derived as

$$u_a = v_a/V_t;\; u_b = v_b/V_t;\; u_c = v_c/V_t \tag{6}$$

Instantaneous values of in-phase components of reference source currents are estimated as

$$i^*_{sad} = I^*_{smd}\, u_a; \quad i^*_{sbd} = I^*_{smd}\, u_b;\; i^*_{scd} = I^*_{smd}\, u_c \tag{7}$$

B. Quadrature Component of Reference Source Currents

The AC voltage error V_{er} at the nth sampling instant is as

$$V_{er(n)} = V_{tref(n)} - V_{t(n)} \tag{8}$$

where $V_{tref(n)}$ is the amplitude of reference AC terminal voltage and $V_{t(n)}$ is the amplitude of the sensed three-phase AC voltage at the terminals of an asynchronous generator at nth instant.

The output of the PI controller ($I^*_{smq(n)}$) for regulating constant AC terminal voltage at the nth sampling instant is expressed as

$$I^*_{smq(n)} = I^*_{smq(n-1)} + K_{pa}\{V_{er(n)} - V_{er(n-1)}\} + K_{ia} V_{er(n)} \tag{9}$$

where K_{pa} and K_{ia} are the proportional and integral gain constants of the proportional integral (PI) controller (values are given in Appendix). $V_{er\,(n)}$ and $V_{er(n-1)}$ are the voltage errors in nth and (n-1)th instant and $I^*_{smq(n-1)}$ is the amplitude of quadrature component of the reference source current at (n-1)th instant.

The instantaneous quadrature components of reference source currents are estimated as

$$i^*_{saq} = I^*_{smq}\, w_a;\; i^*_{sbq} = I^*_{smq}\, w_b;\; i^*_{scq} = I^*_{smq}\, w_c \qquad (10)$$

where w_a, w_b and w_c are another set of unit templates having a phase shift of 90° leading with the corresponding unit templates u_a, u_b and u_c which are computed as follows

$$w_a = -u_b / \sqrt{3} + u_c / \sqrt{3} \qquad (11)$$
$$w_b = \sqrt{3}\, u_a / 2 + (u_b - u_c) / 2\sqrt{3} \qquad (12)$$
$$w_c = -\sqrt{3}\, u_a / 2 + (u_b - u_c) / 2\sqrt{3} \qquad (13)$$

C. Reference Source Currents

Total reference source currents are the sum of in-phase and quadrature components of reference source currents as

$$i^*_{sa} = i^*_{saq} + i^*_{sad} \qquad (14)$$
$$i^*_{sb} = i^*_{sbq} + i^*_{sbd} \qquad (15)$$
$$i^*_{sc} = i^*_{scq} + i^*_{scd} \qquad (16)$$

D. PWM Current Controller

Reference source currents (i^*_{sa}, i^*_{sb} and i^*_{sc}) are compared with sensed source currents (i_{sa}, i_{sb} and i_{sc}). The current errors are computed as:

$$i_{saerr} = i^*_{sa} - i_{sa} \qquad (17)$$
$$i_{sberr} = i^*_{sb} - i_{sb} \qquad (18)$$
$$i_{scerr} = i^*_{sc} - i_{sc} \qquad (19)$$

These current errors are amplified and the amplified signals are compared with fixed frequency (10 kHz) triangular carrier wave to generate gating signals for IGBTs of VSC of the controller.

IV. MODELING OF THE PROPOSED SYSTEM

Fig 2 shows the complete MATLAB based simulation model for the proposed isolated electrical power generating system. This model consists of a mechanical system, an electrical system, proposed voltage and frequency controller and consumer loads. Modeling and simulation are carried in MATLAB version 7.1 using Power System Block-set (PSB) toolbox. The detailed modeling description of each part is given in the following sections.

A. Modeling of Mechanical System

The mechanical system consists of a wind turbine along-with gear system. The gear ratio (N) is selected such that the IAG generates the rated voltage at rated frequency and a rated wind speed of 9m/s to extract the maximum power from the wind turbine. The aerodynamic power generated by the wind turbine can be expressed as

$$P = 0.5\, \rho A C_p \upsilon_w^3 \qquad (20)$$

where the aerodynamic power is expressed as a function of the specific density (ρ) of the air, The swept area of the blades (A) and the wind speed (υ_w).

To generate the constant frequency, the additional generated power with increased wind speed is stored into the battery and the speed of the generator is maintained almost constant. Fig. 3 shows the curve between the power coefficient (C_p) and the tip speed ratio (λ) at zero degree pitch angle(β) which shows that C_p reaches a maximum value (0.48) for a maximum tip speed ratio (8.1). It yields the maximum mechanical power available in the wind turbine for a given wind speed. The tip speed ratio (TSR) is defined as the ratio of the linear speed at the tip of the blade ($\omega_T R$) and the wind speed (ν_w), where ω_T being the rotational speed of the wind turbine. The polynomial relation between C_p and λ at particular pitch angle for considered wind turbine [2] is represented as

$$C_p = C_1 \{(C_2/\lambda i) - C_3 \beta - C_4\}\, e^{-(C_5/\lambda i)} + C_6 \lambda \qquad (21)$$

where $1/\lambda i = \{1/(\lambda + C_7 \beta)\} - \{C_8 / (\beta^3 + 1)\}$ and $\beta = 0°$ and values of all coefficients are given in Appendix.

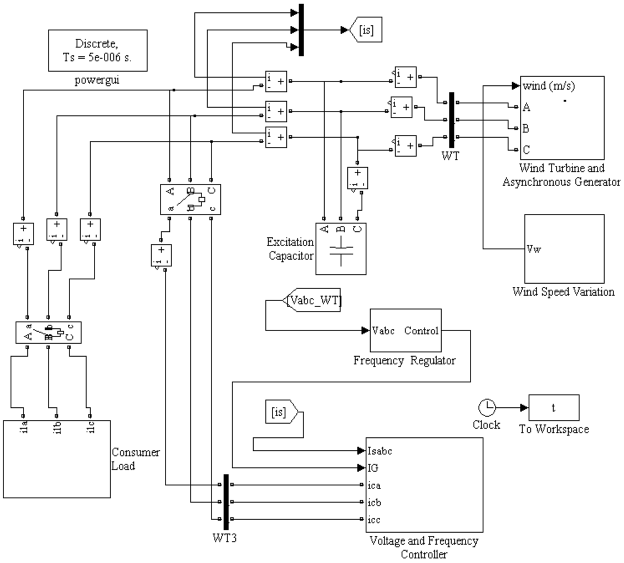

Fig. 2: MATLAB based simulation model of proposed system

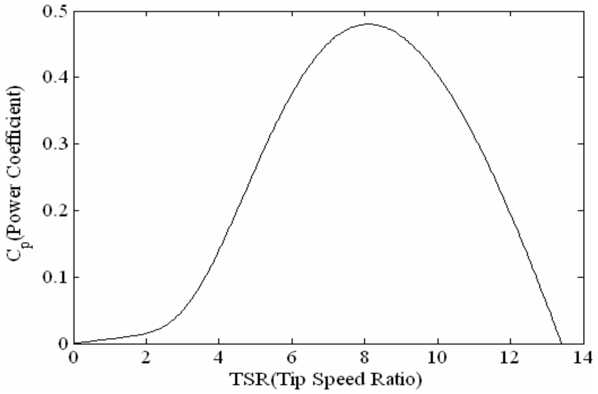

Fig. 3: Curve between power coefficients (C_p) and TSR (λ)

B. Modeling of Electrical System

The electrical system consists of an asynchronous generator with the excitation capacitor. An available model of an asynchronous machine including the saturation characteristics, which is determined by conducting the synchronous speed test on the machine, is considered into the model of the isolated asynchronous generator. A bank of fixed value delta connected excitation capacitor is selected to generate the rated voltage at no-load while additional demand of the reactive power is met by the controller.

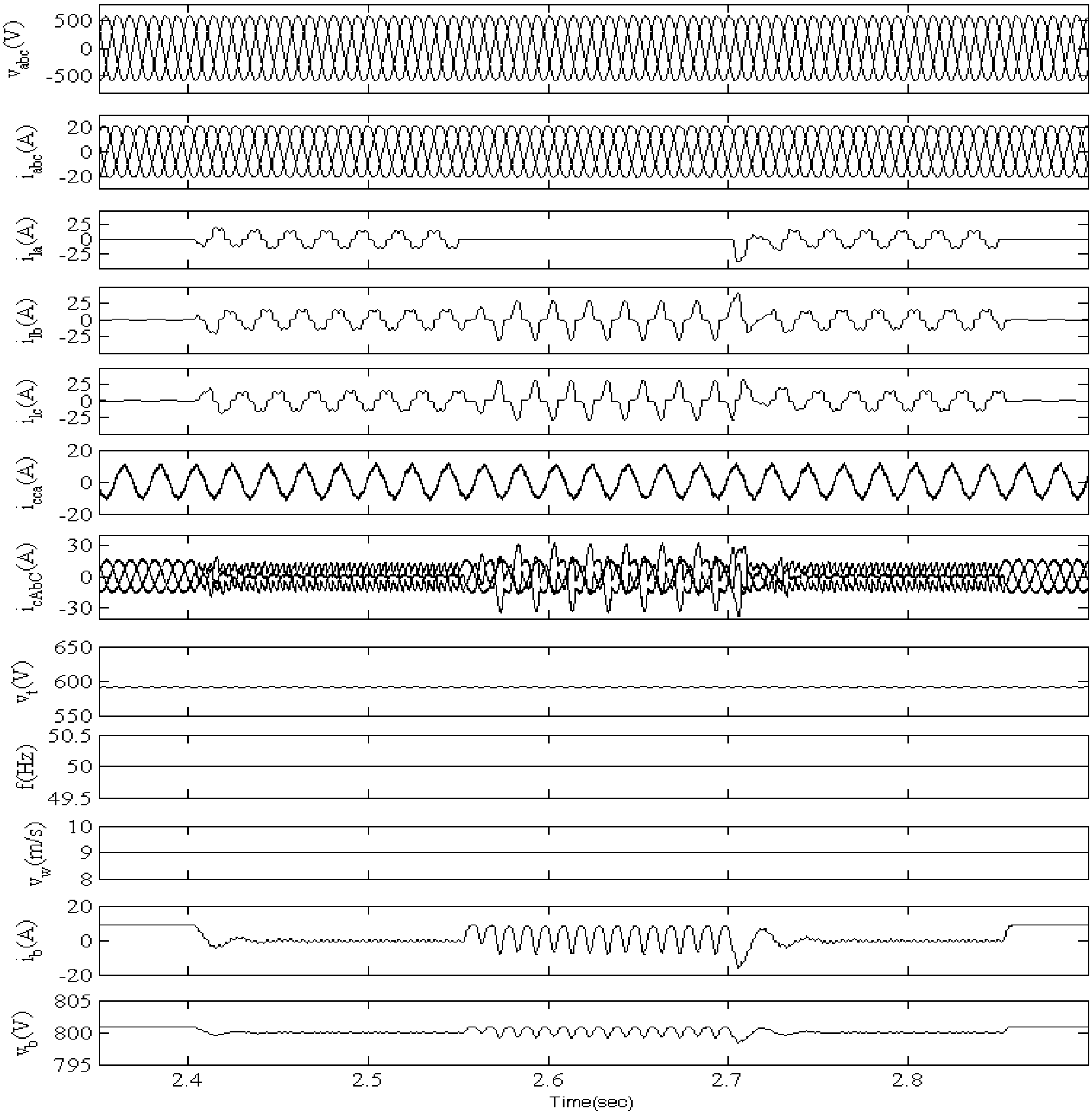

Fig. 4: Transient waveforms under varying balanced/unbalanced non-linear loads at wind speed of 9m/s.

C. Modeling of the Controller

The proposed VF controller consists of CC-VSC with a battery at its DC bus. In Fig 1, Thevenin's equivalent circuit of battery based model [11,12] is shown at DC bus of controller. The terminal voltage of the equivalent battery (V_b) is obtained as follows

$$V_b > (2\sqrt{2}/\sqrt{3})\, V_{LL} \qquad (22)$$

where V_{LL} is the line rms voltage.

Since the battery is an energy storage unit, its energy is represented in kWh when a capacitor is used to model the battery unit, the capacitance can be determined from

$$C_b = \frac{\text{kWh} * 3600 * 10^3}{0.5(V_{ocmax}^2 - V_{ocmin}^2)} \qquad (23)$$

In the Thevenin's equivalent model of the battery, where R_s is the equivalent resistance (external + internal) of parallel/series combination of a battery, which is usually a small value. The parallel circuit of R_b and C_b is used to describe the stored energy and voltage during charging or discharging. R_b in parallel with C_b, represents self discharging of the battery, since the self discharging current of a battery is small, the resistance R_b is large. Here the battery is considered of having 6 kW for 8 Hrs peaking capacity, and with the variation in the voltage of order of 795V-805V.

D. Modeling of the Consumer Loads

Linear and non-linear loads are modeled using resistive element and three phase diode rectifier with resistive element at it DC bus respectively.

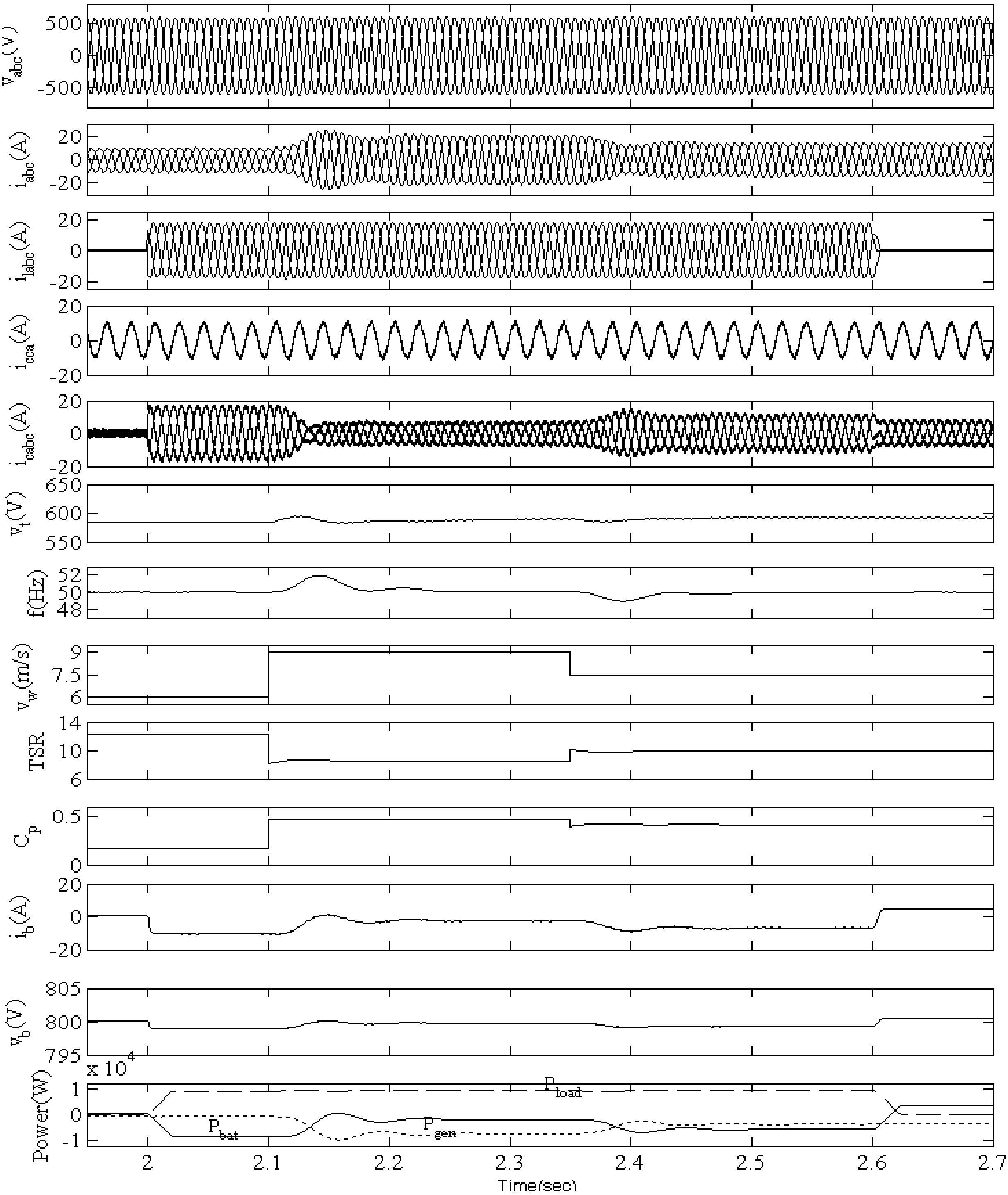

Fig. 4: Transient waveforms under varying balanced/unbalanced non-linear loads at wind speed of 9m/s.

IV. RESULTS AND DISCUSSION

The performance of the proposed controller for a wind turbine driven isolated asynchronous generator system feeding non-linear balanced/unbalanced loads under varying wind speeds are shown in Figs 4-5. The waveforms of the generator voltage (v_{abc}), generator current (i_{abc}), load current (i_{labc}), capacitor current (i_{cca}), controller current (i_{cabc}), terminal voltage (v_t), frequency (f), speed of the wind turbine(υ_w), tip speed ratio (TSR), power coefficient (C_p), battery current (i_b), battery voltage (v_b), and the variation in power (P_{load}, $P_{bat,}$ P_{gen}) are shown during different dynamic conditions.

A. Performance of the Controller with Balance/ Unbalanced Non-linear Loads

The performance of the controller with balanced-unbalanced non-linear loads is demonstrated in Fig. 4 at wind speed of 9m/s. A three phase diode bridge rectifier with L-C filter based non-linear load is applied at 2.4 s and after opening of one phase of the load at 2.55 s the load becomes unbalanced. In both of these cases it is observed that the voltage and frequency of the system remain constant.

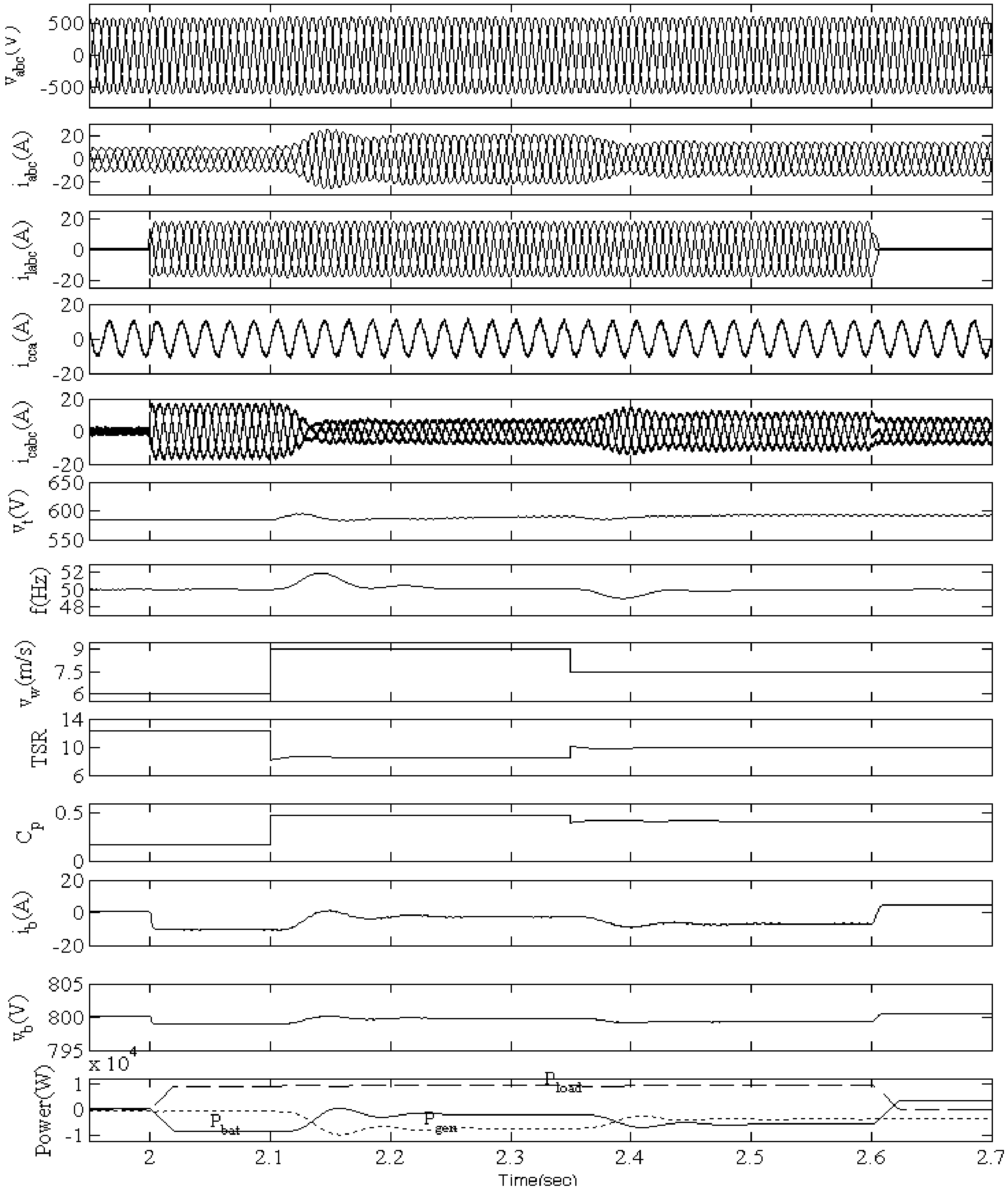

Fig. 5: Transient waveforms during variation of wind speed at particular consumer load.

At 2.7 s, open phase of the load is reconnected and later on at 2.85 s, the load is fully removed from the system and it is observed that the controller responds in desirable manner to regulate the voltage and frequency along-with additional mentioned features of the load balancing and harmonic elimination. Harmonic spectra of the generator voltage (v_a), generator current (i_a) and load current (i_{lb}) are also given in Figs. 6 for balanced non-linear load conditions respectively to demonstrate the harmonic elimination capability of the controller. Total harmonic distortion (THD) of the generator voltage, current is obtained to be an order of 1.87% and 3.99% for the THD of load current of 25.76% under the balanced non-linear load condition. These THD values are well within 5% limit imposed by IEEE-519 standard. In this way it is demonstrated that the proposed voltage and frequency controller is also functioning as a harmonic eliminator.

B. Performance of the Controller with Variation of Wind Speed

Fig. 5 shows the performance of the controller with varying wind speeds at constant applied consumer load. At 2 s when wind speed is 6m/s, a consumer load (9kW) is applied at the generator terminals. It is observed that due to insufficient power generation at low wind speed an additional load power is supplied by the battery to regulate the frequency. At 2.1 s as the wind speed is increased from 6m/s to 9m/s, an output power of the generator (P_{gen}) is increased so that at particular load now the power supplied by the battery (P_{bat}) is reduced because now demand is met by the generator itself and having the availability of enough wind power. For maintaining the constant speed of the generator for constant frequency operation it is shown that tip speed ratio (TSR) is also reduced in same proportion as the wind speed is increased. At 2.35 s, the wind speed is reduced from 9m/s to 7.5m/sec then it is observed that the battery again starts discharging to meet the demand of the consumer loads. At 2.6 s when the load is fully removed it is shown that the battery starts charging to store the total generated power. In this manner, the controller provides the load leveling and regulation of the frequency. Here an interesting observation is also made that the response of the controller under electrical dynamic conditions (load variation) is faster than the mechanical dynamic conditions (wind speed variation) and the frequency regulation under electrical dynamic condition is much faster than the mechanical dynamic condition. It is mainly because mechanical time constant is higher than the electrical time constant of the system.

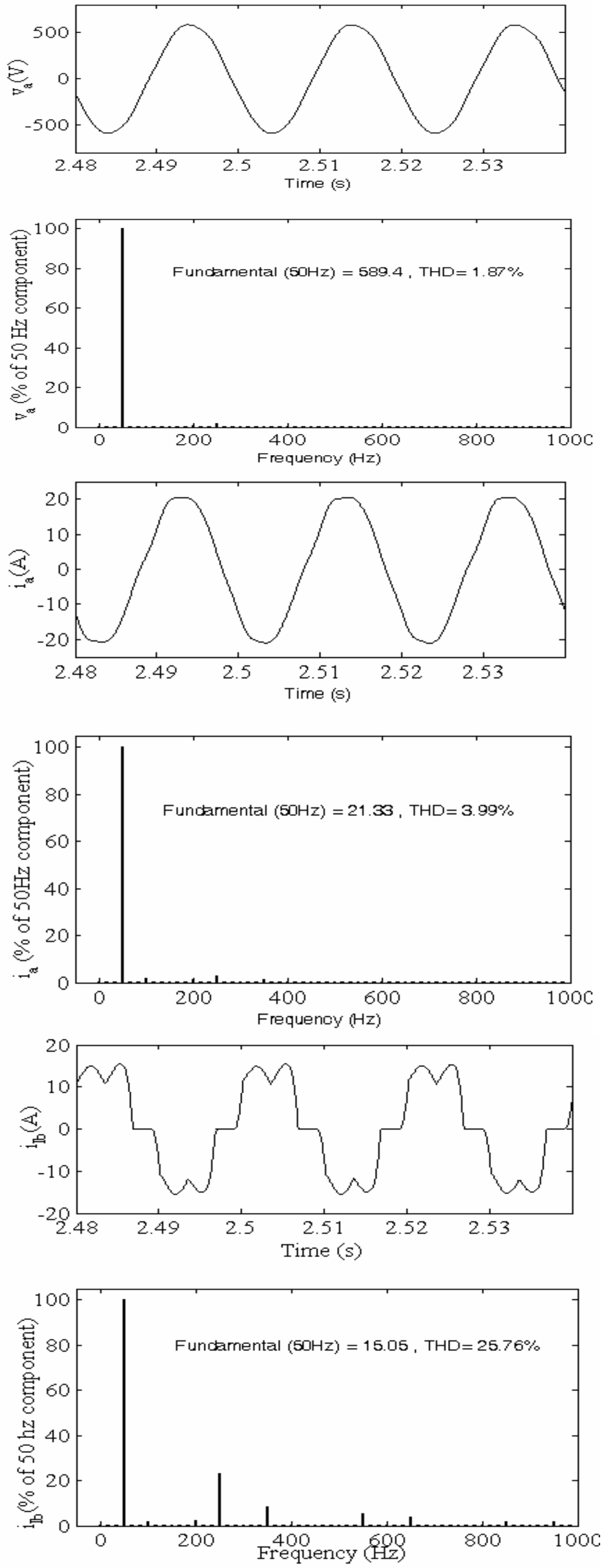

Fig. 6: Harmonic spectra of (a) generator voltage (v_a) (b) generator current (i_a) (c) load current (i_{lb}) under balanced non-linear load condition.

VI. CONCLUSIONS

The performance of the proposed voltage and frequency controller has been demonstrated for an isolated asynchronous generator driven by fixed pitch wind turbine. The proposed controller has been found suitable with simple control strategy to regulate the voltage and frequency with variation of the load and under varying wind speeds. The performance of the controller has been investigated with balanced and un-balanced non-linear loads and it has been found that total harmonic distortion of terminal voltage and the generator current in such type of worst load condition is well within the limit of IEEE-519 standard. Therefore it is concluded that proposed voltage and frequency controller is also functioning as a harmonic eliminator, a load balancer and a load leveler.

APPENDIX

A. Parameters of 7.5kW, 415V, 50Hz, Y-Connected 4-pole Asynchronous Machine are given below.

$R_s = 1\Omega$, $R_r = 0.77\Omega$, $X_{lr} = X_{ls} = 1.5\Omega$, $J = 0.1384$ kg-m^2, $C_2 = 5$ kVAR

$L_m = 0.134$ ($I_m<3.16$)

$L_m = 9e\text{-}5I_m^2 - 0.0087I_m + 0.1643$ ($3.16<I_m<12.72$)

$L_m = 0.068$ ($I_m>12.72$)

B. Battery Specification

$C_b = 21500$F, $R_b = 10\text{k}\Omega$, $R_s = 0.01\Omega$, $V_{oc} = 800$V

C. Controller Pararameters

$L_f = 3$mH, $R_f = 0.1\Omega$, and $C_{dc} = 8000\mu$F

$K_{pa} = 0.13$, $K_{ia} = 0.012$; $K_{pf} = 6.13$, $K_{if} = 140$

D. Wind Turbine Specification

Rating 7.5kW, Gear ratio (N) = 11, Radius of wind urbine (R) = 5m, $C_{pmax} = 0.48$,

$\lambda_m = 8.1$, $C_1 = 0.5176$, $C_2 = 116$, $C_3 = 0.4$, $C_4 = 5$, $C_5 = 21$, $C_6 = 0.0068$, $C_7 = 0.08$, $C_8 = 0.035$.

REFERENCES

[1] Bhim Singh and Gaurav Kumar Kasal, "Analysis and Design of Voltage and Frequency Controllers in a Constant Power Applications", in Proc of IEEE International Conf on Power Electronics Drives and Energy Systems (PEDES'06), New Delhi, India, Dec 12-15, 2006.

[2] Siegfried Heier, "Grid Integration of Wind Energy Conversion Systems", IEEE Trans. on Energy Conversion, Vol. 19, No. 1, March 2004, pp.136-143.

[3] T.F. Chan and L.L Lai, “A novel excitation scheme for a stand-alone three-phase induction generator supplying single-phase loads”, IEEE Trans. on Energy Conversion, Vol. 19, No. 1, March 2004, pp.136-143.

[4] T.F. Chan, and L.L. Lai, “Single-phase operation of a three-phase induction generator using a novel current-injection method”, IEEE Trans. on Energy Conversion, Vol. 20, No. 2, June 2005, pp. 308-315.

[5] M Ermis, H. B Ertan, M Demirekler, “Various induction generator schemes for wind electricity- generation”, Electric Power Systems Research, Vol. 23, No.1, Jan1992, pp 71-83.

[6] T.F. Chan, K.A. Nigim, L.L. Lai, “Voltage and frequency control of self-excited slip-ring induction generators”, IEEE Trans. on Energy Conv, Vol. 19 1No.1, Mar 2004, pp 81-87.

[7] Y.S. Wang, L Wang, “Minimum Loading resistance and its effects on performance of an isolated self-excited reluctance generator”, IEE Proc.Gen. Trans. and Dist. Vol. 148, No.3, May 2001, pp 251-256.

[8] D Sutanto, C. Grantham, F. Rahman, “A regulated self-excited induction generator for use in a remote area power supply”, Sixth International Conference on Electrical Machines and Drives, 1993, pp 3234-239.

[9] Dawit Seyoum, Colin Grantham and Fazlur Rahaman, “The dynamic characteristics of an isolated self excited induction generator driven by a wind turbine”, IEEE Trans on Industry Applications, Vol. 39, No. 4, July/Aug 2003, pp 936-944.

[10] Bhim Singh and Gaurav Kumar Kasal, “Battery energy storage system based controller for a wind turbine driven isolated asynchronous generator”, Journal of Power Electronics, Vol. 23, No.1, Jan. 2008, pp 81-90.

[11] Z. M. Salameh, M. A. Casacca and W.A. Lynch, “A mathematical model for lead-acid batteries”, IEEE Trans. Energy Conversion, Vol. 7, No.1, March 1992, pp.93-97.

[12] M.D. Aderson and D.S Carr., “Battery energy storage technology”, IEEE Proc, Vol. 81, March 1993, pp 475-479.

[13] R.S Bhatia., D.K Jain., B. Singh and S.P. Jain, “Battery energy storage system for power conditioning of renewable energy sources”, in Proc. of IEEE Conference on Power Electronics and Drive Systems, Dec. 2005, pp.501-506.

BIOGRAPHIES

Bhim Singh was born in Rahamapur, India, in 1956. He received the B.E (Electrical) degree from the University of Roorkee, Roorkee, India, in 1977 and the M.Tech and Ph.D. degree from the Indian Institute of Technology (IIT) Delhi, New Delhi, India, in 1979 and 1983, respectively. In 1983, he joined the Department of Electrical Engineering, University of Roorkee, as a lecturer, and in 1988 became a Reader. In December 1990, he joined the Department of Electrical Engineering , IIT Delhi, as an Assistant Professor. He became an Associate Professor in 1994 and Professor in 1997. His area of interest includes power electronics, electrical machines and drives, active filters, FACTS, HVDC and power quality

Dr. Singh is a fellow of Indian National Academy of Engineering (INAE), the Institution of Engineers (India) (IE (I)), and the Institution of Electronics and Telecommunication Engineers (IETE), a life member of the Indian Society for Technical Education (ISTE), the System Society of India (SSI), and the National Institution of Quality and Reliability (NIQR) and Senior Member of Institute of Electrical and Electronics Engineers (IEEE).

Gaurav Kumar Kasal was born in Bhopal, India, in Nov, 1978. He received the B.E (Electrical) and M.Tech degree from the National Institute of Technology (NIT) Allahabad and National Institute of Technology (NIT) Bhopal, India respectively in 2002 and 2004. Since Dec 2004, he has been pursuing the Ph. D. degree with the Department of Electrical Engineering, Indian Institute of Technology (IIT) Delhi, New Delhi, India. His field of interest includes power electronics and drives, renewable energy generation and applications, flexible AC transmission system.

Asian Power Electronics Journal, Vol. 2, No. 1, Apr 2008

Speeds Estimation of Series-Connected Five-Phase Two-Motor Drive System using Adaptive Flux Observers

M. Rizwan Khan[1] and Atif Iqbal[2]

Abstract— Utilization of multi-phase machines in variable speed drives is nowadays extensively considered for electric ship propulsion, 'more-electric aircraft' and traction applications, including EVs and HEVs. In addition to well-known advantages, use of multi-phase machines enables independent control of a certain number of machines that are connected in series in an appropriate manner, with the supply coming from a single voltage source inverter (VSI). The concept was initially proposed for a five-phase series-connected two-motor drive, but is applicable to any system phase number greater than or equal to five. The number of connectable machines is a function of the VSI phase number and detailed theoretical and simulation studies have already been reported for various multi-phase multi-motor drive configurations of this type. Variable speed induction motor drives without mechanical speed sensors at the motor shaft have the attractions of low cost and high reliability. To replace the sensor, information of the rotor speed is extracted from measured stator currents and voltages at motor terminals. Open-loop estimators or closed-loop observers are used for this purpose. They differ with respect to accuracy, robustness, and sensitivity against model parameter variations. This paper analyses operation of an adaptive flux observer-based sensorless control of vector controlled series connected two motor five-phase drive system with current control in the stationary reference frame. Performance, obtainable with hysteresis current control, is illustrated for a number of operating conditions on the basis of simulation results. The purpose of this paper is to present, for the first time, simulation results on a sensorless control of a five-phase two-motor series-connected drive system. A brief overview of the operating principles is provided first. This is followed by a description of the sensorless technique.

Keywords — Multi-motor drives, Multi-phase machines, Five-phase, Vector control.

I. INTRODUCTION

Concept of multi-phase motor drives is rather mature, with the origins traceable back to 1969. However, an upsurge in the interest in multi-phase motor drive applications has occurred during the last few years. The main driving forces behind this accelerated development are three application areas: railway traction and EV/HEV applications, 'more-electric aircraft' and 'more-electric ship'. The reasons for employing multi-phase drives vary from application to application and range from reduction of the inverter per-phase rating in high power drives (ship propulsion, traction) to improved efficiency (low power drives and integrated drives) [1] and to significantly improved fault tolerance ('more-electric aircraft') [2,3].

An additional possibility, opened up by the use of multi-phase machines, is independent control of a set of series-connected motors, supplied from a single VSI. The origins of the idea can be traced to [4], where a five-phase two-motor drive was analyzed. The idea stems from the fact that any n-phase machine requires only two currents for independent flux and torque control. Thus, in a multi-phase machine there are additional degrees of freedom, which can be used to control other machines, provided that an appropriate phase transposition is introduced when connecting the machines in series. The concept is applicable to all supply system phase numbers greater than or equal to five. Generalizations to all possible even and odd phase numbers have been reported in [5-7], where appropriate winding connections and the number of connectable machines as a function of the system phase number were investigated. Studies of [4-7] apply to series connection of symmetrical multi-phase machines (spatial displacement between any two consecutive phases is $2\pi/n$, where n is the number of phases) with sinusoidal flux spatial distribution. However, the concept of series connection can be extended to the asymmetrical machines as well, where stator winding consists of two or more three-phase windings shifted in space by an appropriate angle. A two-motor drive of this type, using asymmetrical six-phase machines (with two three-phase windings spatially shifted by 30º) has been considered in [8,9].

From the practical point of view it is only the five-phase or six-phase two-motor drives that hold potential for industrial applications. This is so since in the series connection flux/torque producing currents of one machine flow through the other machines in the group. Thus stator winding loss increases, causing a reduction in the efficiency. Most of the available work on series-connected drive systems therefore discusses either five-phase or one of the two possible six-phase (with asymmetrical or symmetrical six-phase machines) configurations. An investigation of the operating principles of the two-motor series-connected five-phase drive has been reported in [10-12], while a *d-q* model for this drive structure can be found in [13]. Inverter current control can be realized by using either synchronous current controllers or by means of phase current control in the stationary reference frame. A comparison of these two possibilities [14] has shown that phase current control in the stationary reference frame is advantageous for series-connected multi-motor drive systems, since synchronous current control leads to an increase in the parameter variation sensitivity in the decoupling circuit equations. This current control method is utilized here.

The available experimental results that illustrate dynamics of a vector-controlled series-connected multi-motor drive are those for a two-motor six-phase drive [9,15],

---

The paper first received 5 Nov 2007 and in revised form 30 Dec 2007
Digital ref: AI70201181

[1] Department of Electrical Engineering, Aligarh Muslim University, Aligarh, (U.P.)-India, E-mail: rizwan_eed@rediffmail.com

[2] Department of Electrical Engineering, Aligarh Muslim University, Aligarh, (U.P.)-India, E-mail: atif_iqbal1@rediffmail.com

comprising a symmetrical six-phase machine connected in series with a three-phase machine.

Additionally, [8] illustrates performance of a six-phase drive consisting of two series-connected asymmetrical six-phase machines under V/f control. This paper therefore concentrates on presentation of simulation results, collected from a vector-controlled series-connected five-phase two-motor drive system, which provide an ultimate proof of the decoupled dynamics within the system. A brief overview of the operating principles is provided first. A series of simulation test result, for various transients (acceleration, deceleration, speed reversal) is then presented. These prove that the coupling of control of the two machines is practically negligible, although they are connected in series and the supply is provided from a single five-phase VSI.

The two-motor drive structure elaborated here is believed to hold a good prospect for industrial applications related to winders. In such an application use of two series-connected five-phase machines can not only save one inverter leg (when compared to an equivalent two-motor three-phase system) but also reduce the total installed inverter rating, thus reducing the capital outlay. The best results would be achievable with permanent magnet synchronous machines, since no machine de-rating would be needed to compensate for the increased stator winding losses.

Sensorless operation of a vector controlled three-phase induction machine drive is extensively discussed in the literature [16,17], but the same is not true for multi-phase induction machine. Only few application specific sensorless operation of multi-phase machine is elaborated in the literature The problem of using the position sensor in ‘more-electric’ aircraft fuel pump fault tolerant drive is highlighted in [18]. The drive utilises a 16 kW, 13000 rpm six-phase permanent magnet motor with six independent single-phase inverters supplying each of the six-phases. The authors proposed an alternative sensorless drive scheme. The proposed technique makes use of flux linkage-current-angle model to estimate the rotor position. Although several schemes are available for sensorless operation of a vector controlled drive, but the most popular is the MRAS because of ease of their implementation[17,18].

An observer can be classified according to the type of representation used for the plant to be observed. If the plant is considered to be deterministic, then the observer is a deterministic observer; otherwise it is a stochastic observer. The most commonly used observers are *Luenberger* and *Kalman* types. The *Luenberger* observer (LO) is of the deterministic type and the Kalman filter (KF) is of the stochastic type. The basic Kalman filter is only applicable to linear stochastic systems, and for non-linear systems the extended Kalman filter (EKF) can be used, which can provide estimates of the states of a system or of both the states and parameters (joint state and parameter estimation). The EKF is a recursive filter, which can be applied to a non-linear time-varying stochastic system. The basic Luenberger observer is only applicable to a linear, time-invariant deterministic system. The extended Luenberger observer (ELO) is applicable to a non-linear, time-varying deterministic system.

In summary it can be seen that both the EKF and ELO are non-linear estimators and the EKF is applicable to stochastic systems and the ELO to deterministic systems. The extended Luenberger observer (ELO) is an alternative solution for real-time implementation in industrial drive systems. The simple algorithm and the ease of tuning of the ELO may give some advantages over the conventional EKF.

A full-order (fourth-order) adaptive state observer (Luenberger observer) which is constructed by using the equations of the induction machine in the stationary reference frame by adding an error compensator. In the full-order adaptive state observer the rotor speed is considered as a parameter, but in the EKF and ELO the rotor speed is considered as a state variable. It is shown that [21-22] when the appropriate observers are used in high-performance speed sensorless torque controlled induction motor drive (vector controlled drives, direct controlled drives), stable operation can be obtained over a wide speed range, including very low speeds.

A simulation study is performed for speed mode of operation, for a number of transients, and the results are reported in the paper.

II. FIVE-PHASE TWO-MOTOR DRIVE SYSTEM

A principal block-diagram of the series-connected five-phase two-motor drive system is shown in Fig. 1. Stator windings of the two five-phase machines (which can be of any type, i.e. induction, synchronous reluctance, or permanent magnet synchronous) are connected in series, in such a way that flux/torque producing currents of one machine appear as non-flux/torque producing currents in the other machine, and vice-versa [4,6,7,10]. It is assumed that the spatial flux distribution in both machines is perfectly sinusoidal. The supply is a five-phase VSI, whose outputs are identified with capital letters A, B, C, D, E, while lower case letters (a, b, c, d, e) identify phases of the two machines according to the spatial distribution of the stator windings (spatial displacement between any two consecutive phases is $\alpha = 2\pi/5 = 72°$).

According to the connection diagram of Fig. 1, inverter phase-to-neutral voltages are related to individual machine phase voltages through

$$\begin{array}{ll} v_A = v_{a1} + v_{a2} & v_B = v_{b1} + v_{c2} \\ v_C = v_{c1} + v_{e2} & v_D = v_{d1} + v_{b2} \\ \multicolumn{2}{c}{v_E = v_{e1} + v_{d2}} \end{array} \tag{1}$$

while the correlation between inverter output currents and machine phase currents is given with

$$\begin{array}{ll} i_A = i_{a1} = i_{a2} & i_B = i_{b1} = i_{c2} \\ i_C = i_{c1} = i_{e2} & i_D = i_{d1} = i_{b2} \\ \multicolumn{2}{c}{i_E = i_{e1} = i_{d2}} \end{array} \tag{2}$$

The simplest form of indirect rotor flux oriented control is considered. Vector controller’s form depends on the type of the machine and is illustrated in Fig. 2 for an induction machine, as well as for a synchronous reluctance and a permanent magnet synchronous machine. Using the indirect vector controllers of Fig. 2, phase current references for the two machines are created by means of ($k=\sqrt{2/5}$):

$$\begin{aligned}
i_{a1}^{*} &= k[i_{ds1}^{*}\cos\phi_{r1} - i_{qs1}^{*}\sin\phi_{r1}] \\
i_{b1}^{*} &= k[i_{ds1}^{*}\cos(\phi_{r1}-\alpha) - i_{qs1}^{*}\sin(\phi_{r1}-\alpha)] \\
i_{c1}^{*} &= k[i_{ds1}^{*}\cos(\phi_{r1}-2\alpha) - i_{qs1}^{*}\sin(\phi_{r1}-2\alpha)] \\
i_{d1}^{*} &= k[i_{ds1}^{*}\cos(\phi_{r1}-3\alpha) - i_{qs1}^{*}\sin(\phi_{r1}-3\alpha)] \\
i_{e1}^{*} &= k[i_{ds1}^{*}\cos(\phi_{r1}-4\alpha) - i_{qs1}^{*}\sin(\phi_{r1}-4\alpha)]
\end{aligned} \tag{3}$$

$$\begin{aligned}
i_{a2}^{*} &= k[i_{ds2}^{*}\cos\phi_{r2} - i_{qs2}^{*}\sin\phi_{r2}] \\
i_{b2}^{*} &= k[i_{ds2}^{*}\cos(\phi_{r2}-\alpha) - i_{qs2}^{*}\sin(\phi_{r2}-\alpha)] \\
i_{c2}^{*} &= k[i_{ds2}^{*}\cos(\phi_{r2}-2\alpha) - i_{qs2}^{*}\sin(\phi_{r2}-2\alpha)] \\
i_{d2}^{*} &= k[i_{ds2}^{*}\cos(\phi_{r2}-3\alpha) - i_{qs2}^{*}\sin(\phi_{r2}-3\alpha)] \\
i_{e2}^{*} &= k[i_{ds2}^{*}\cos(\phi_{r2}-4\alpha) - i_{qs2}^{*}\sin(\phi_{r2}-4\alpha)]
\end{aligned}$$

The inverter phase current references are further created by summing the individual machine phase current references, according to the connection diagram of Fig. 1,

$$\begin{aligned}
i_A^{*} &= i_{a1}^{*} + i_{a2}^{*} & i_B^{*} &= i_{b1}^{*} + i_{c2}^{*} \\
i_C^{*} &= i_{c1}^{*} + i_{e2}^{*} & i_D^{*} &= i_{d1}^{*} + i_{b2}^{*} \\
& & i_E^{*} &= i_{e1}^{*} + i_{d2}^{*}
\end{aligned} \tag{4}$$

Assuming ideal inverter current control in the stationary reference frame, inverter reference currents of (4) equal inverter actual currents of (2). Thus each phase of each machine carries flux/torque producing currents of both machines. However, the specific connection of Fig. 1 means that the set of flux/torque producing currents of one machine produces rotating field in that machine only, while in the other machine the resultant field sums to zero at any instant in time [4,10]. Hence the two machines can be controlled independently, although they are connected in series and supplied from a single five-phase VSI.

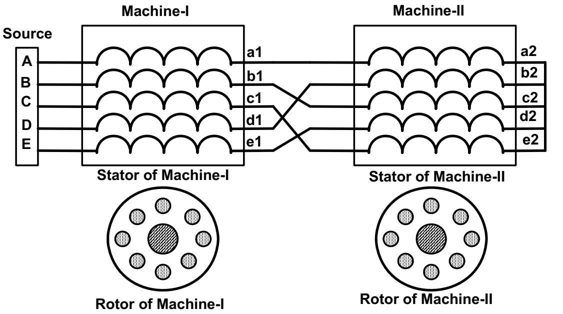

Fig. 1: Series connection of two five-phase machines.

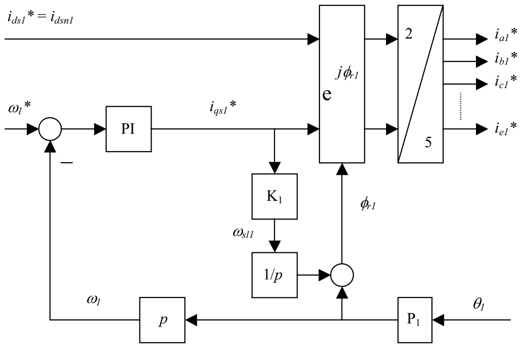

Fig. 2: Indirect rotor flux oriented controller for a five-phase induction machine ($K_1 = 1/(T_{r1}^{*} i_{ds1}^{*})$, $p \equiv d/dt$).

III. MODELLING OF THE SERIES-CONNECTED FIVE-PHASE TWO-MOTOR DRIVE

Phase variable model of two five-phase induction machines connected in series according to Fig. 1 is developed in state space form as follows:

$$\begin{aligned}
v_A &= v_{as1} + v_{as2} & i_A &= i_{as1} = i_{as2} \\
v_B &= v_{bs1} + v_{cs2} & i_B &= i_{bs1} = i_{cs2} \\
v_C &= v_{cs1} + v_{es2} \quad \text{and} & i_C &= i_{cs1} = i_{es2} \\
v_D &= v_{ds1} + v_{bs2} & i_D &= i_{ds1} = i_{bs2} \\
v_E &= v_{es1} + v_{ds2} & i_E &= i_{es1} = i_{ds2}
\end{aligned} \tag{5}$$

In a general case the two machines, although both five-phase, may be different and therefore may be with different parameters. Let the index '1' denote induction machine directly connected to the five-phase inverter and let the index '2' stand for the second induction machine, connected after the first machine through phase transposition.

Voltage equation for the complete system can be written in a compact matrix form as

$$\underline{v} = \underline{R}\,\underline{i} + \frac{d(\underline{L}\,\underline{i})}{dt} \tag{6}$$

where the system is of the 15th order and

$$\underline{v} = \begin{bmatrix} \underline{v}^{INV} \\ \underline{0} \\ \underline{0} \end{bmatrix} \qquad \underline{i} = \begin{bmatrix} \underline{i}^{INV} \\ \underline{i}_{r1} \\ \underline{i}_{r2} \end{bmatrix} \tag{7}$$

$$\begin{aligned}
\underline{v}^{INV} &= [v_A \quad v_B \quad v_C \quad v_D \quad v_E]^T \\
\underline{i}^{INV} &= [i_A \quad i_B \quad i_C \quad i_D \quad i_E]^T
\end{aligned} \tag{8}$$

$$\begin{aligned}
\underline{i}_{r1} &= [i_{ar1} \quad i_{br1} \quad i_{cr1} \quad i_{dr1} \quad i_{er1}]^T \\
\underline{i}_{r2} &= [i_{ar2} \quad i_{br2} \quad i_{cr2} \quad i_{dr2} \quad i_{er2}]^T
\end{aligned} \tag{9}$$

The resistance and inductance matrices of (6) can be written as

$$\underline{R} = \begin{bmatrix} \underline{R}_{s1} + \underline{R}_{s2} & \underline{0} & \underline{0} \\ \underline{0} & \underline{R}_{r1} & \underline{0} \\ \underline{0} & \underline{0} & \underline{R}_{r2} \end{bmatrix} \tag{10}$$

$$\underline{L} = \begin{bmatrix} \underline{L}_{s1} + \underline{L}_{s2}{}' & \underline{L}_{sr1} & \underline{L}_{sr2}{}' \\ \underline{L}_{rs1} & \underline{L}_{r1} & \underline{0} \\ \underline{L}_{rs2}{}' & \underline{0} & \underline{L}_{r2} \end{bmatrix} \tag{11}$$

Superscript ' in (11) denotes sub-matrices of machine 2 that have been modified through the phase transposition operation, compared to their original form. The sub-matrices of (10)-(11) are all five by five matrices and are given with the following expressions $(\alpha = 2\pi/5)$:

$$\begin{aligned}
\underline{R}_{s1} &= diag\left(R_{s1} \quad R_{s1} \quad R_{s1} \quad R_{s1} \quad R_{s1}\right)\\
\underline{R}_{s2} &= diag\left(R_{s2} \quad R_{s2} \quad R_{s2} \quad R_{s2} \quad R_{s2}\right)\\
\underline{R}_{r1} &= diag\left(R_{r1} \quad R_{r1} \quad R_{r1} \quad R_{r1} \quad R_{r1}\right)\\
\underline{R}_{r2} &= diag\left(R_{r2} \quad R_{r2} \quad R_{r2} \quad R_{r2} \quad R_{r2}\right)
\end{aligned} \tag{12}$$

$$\underline{L}_{s1} = \begin{bmatrix} L_{ls1}+M_1 & M_1\cos\alpha & M_1\cos 2\alpha & M_1\cos 2\alpha & M_1\cos\alpha \\ M_1\cos\alpha & L_{ls1}+M_1 & M_1\cos\alpha & M_1\cos 2\alpha & M_1\cos 2\alpha \\ M_1\cos 2\alpha & M_1\cos\alpha & L_{ls1}+M_1 & M_1\cos\alpha & M_1\cos 2\alpha \\ M_1\cos 2\alpha & M_1\cos 2\alpha & M_1\cos\alpha & L_{ls1}+M_1 & M_1\cos\alpha \\ M_1\cos\alpha & M_1\cos 2\alpha & M_1\cos 2\alpha & M_1\cos\alpha & L_{ls1}+M_1 \end{bmatrix} \tag{13}$$

$$\underline{L}_{s2}' = \begin{bmatrix} L_{ls2}+M_2 & M_2\cos 2\alpha & M_2\cos\alpha & M_2\cos\alpha & M_2\cos 2\alpha \\ M_2\cos 2\alpha & L_{ls2}+M_2 & M_2\cos 2\alpha & M_2\cos\alpha & M_2\cos\alpha \\ M_2\cos\alpha & M_2\cos 2\alpha & L_{ls2}+M_2 & M_2\cos 2\alpha & M_2\cos\alpha \\ M_2\cos\alpha & M_2\cos\alpha & M_2\cos 2\alpha & L_{ls2}+M_2 & M_2\cos 2\alpha \\ M_2\cos 2\alpha & M_2\cos\alpha & M_2\cos\alpha & M_2\cos 2\alpha & L_{ls2}+M_2 \end{bmatrix} \tag{14}$$

$$\underline{L}_{r1} = \begin{bmatrix} L_{lr1}+M_1 & M_1\cos\alpha & M_1\cos 2\alpha & M_1\cos 2\alpha & M_1\cos\alpha \\ M_1\cos\alpha & L_{lr1}+M_1 & M_1\cos\alpha & M_1\cos 2\alpha & M_1\cos 2\alpha \\ M_1\cos 2\alpha & M_1\cos\alpha & L_{lr1}+M_1 & M_1\cos\alpha & M_1\cos 2\alpha \\ M_1\cos 2\alpha & M_1\cos 2\alpha & M_1\cos\alpha & L_{lr1}+M_1 & M_1\cos\alpha \\ M_1\cos\alpha & M_1\cos 2\alpha & M_1\cos 2\alpha & M_1\cos\alpha & L_{lr1}+M_1 \end{bmatrix} \tag{15}$$

$$\underline{L}_{r2} = \begin{bmatrix} L_{lr2}+M_2 & M_2\cos\alpha & M_2\cos 2\alpha & M_2\cos 2\alpha & M_2\cos\alpha \\ M_2\cos\alpha & L_{lr2}+M_2 & M_2\cos\alpha & M_2\cos 2\alpha & M_2\cos 2\alpha \\ M_2\cos 2\alpha & M_2\cos\alpha & L_{lr2}+M_2 & M_2\cos\alpha & M_2\cos 2\alpha \\ M_2\cos 2\alpha & M_2\cos 2\alpha & M_2\cos\alpha & L_{lr2}+M_2 & M_2\cos\alpha \\ M_2\cos\alpha & M_2\cos 2\alpha & M_2\cos 2\alpha & M_2\cos\alpha & L_{lr2}+M_2 \end{bmatrix} \tag{16}$$

$$\begin{aligned}
\underline{L}_{sr1} &= M_1 \begin{bmatrix} \cos\theta_1 & \cos(\theta_1+\alpha) & \cos(\theta_1+2\alpha) & \cos(\theta_1-2\alpha) & \cos(\theta_1-\alpha) \\ \cos(\theta_1-\alpha) & \cos\theta_1 & \cos(\theta_1+\alpha) & \cos(\theta_1+2\alpha) & \cos(\theta_1-2\alpha) \\ \cos(\theta_1-2\alpha) & \cos(\theta_1-\alpha) & \cos\theta_1 & \cos(\theta_1+\alpha) & \cos(\theta_1+2\alpha) \\ \cos(\theta_1+2\alpha) & \cos(\theta_1-2\alpha) & \cos(\theta_1-\alpha) & \cos\theta_1 & \cos(\theta_1+\alpha) \\ \cos(\theta_1+\alpha) & \cos(\theta_1+2\alpha) & \cos(\theta_1-2\alpha) & \cos(\theta_1-\alpha) & \cos\theta_1 \end{bmatrix}\\
\underline{L}_{rs1} &= \underline{L}_{sr1}^{T}
\end{aligned} \tag{17}$$

$$\begin{aligned}
\underline{L}_{sr2}' &= M_2 \begin{bmatrix} \cos\theta_2 & \cos(\theta_2+\alpha) & \cos(\theta_2+2\alpha) & \cos(\theta_2-2\alpha) & \cos(\theta_2-\alpha) \\ \cos(\theta_2-2\alpha) & \cos(\theta_2-\alpha) & \cos\theta_2 & \cos(\theta_2+\alpha) & \cos(\theta_2+2\alpha) \\ \cos(\theta_2+\alpha) & \cos(\theta_2+2\alpha) & \cos(\theta_2-2\alpha) & \cos(\theta_2-\alpha) & \cos\theta_2 \\ \cos(\theta_2-\alpha) & \cos\theta_2 & \cos(\theta_2+\alpha) & \cos(\theta_2+2\alpha) & \cos(\theta_2-2\alpha) \\ \cos(\theta_2+2\alpha) & \cos(\theta_2-2\alpha) & \cos(\theta_2-\alpha) & \cos\theta_2 & \cos(\theta_2+\alpha) \end{bmatrix}\\
\underline{L}_{rs2}' &= \underline{L}_{sr2}^{T}{}'
\end{aligned} \tag{18}$$

Expansion of (6) yields

$$\begin{aligned}
\underline{v} &= \begin{bmatrix} \underline{v}^{INV} \\ \underline{0} \\ \underline{0} \end{bmatrix}\\
&= \begin{bmatrix} \underline{R}_{s1}+\underline{R}_{s2} & \underline{0} & \underline{0} \\ \underline{0} & \underline{R}_{r1} & \underline{0} \\ \underline{0} & \underline{0} & \underline{R}_{r2} \end{bmatrix} \begin{bmatrix} \underline{i}^{INV} \\ \underline{i}_{r1} \\ \underline{i}_{r2} \end{bmatrix} + \begin{bmatrix} \underline{L}_{s1}+\underline{L}_{s2}' & \underline{L}_{sr1} & \underline{L}_{sr2}' \\ \underline{L}_{rs1} & \underline{L}_{r1} & \underline{0} \\ \underline{L}_{rs2}' & \underline{0} & \underline{L}_{r2} \end{bmatrix} \frac{d}{dt} \begin{bmatrix} \underline{i}^{INV} \\ \underline{i}_{r1} \\ \underline{i}_{r2} \end{bmatrix} + \begin{bmatrix} \underline{0} & \frac{d}{dt}\underline{L}_{sr1} & \frac{d}{dt}\underline{L}_{sr2}' \\ \frac{d}{dt}\underline{L}_{rs1} & \underline{0} & \underline{0} \\ \frac{d}{dt}\underline{L}_{rs2}' & \underline{0} & \underline{0} \end{bmatrix} \begin{bmatrix} \underline{i}^{INV} \\ \underline{i}_{r1} \\ \underline{i}_{r2} \end{bmatrix}
\end{aligned} \tag{19}$$

Torque equations of the two machines in terms of inverter currents and their respective rotor currents and rotor positions and replacing motor stator currents with corresponding inverter currents of (5):

$$T_{e1} = -P_1 M_1 \begin{Bmatrix} \left(i_A i_{ar1} + i_B i_{br1} + i_C i_{cr1} + i_D i_{dr1} + i_E i_{er1}\right)\sin\theta_1 + \left(i_E i_{ar1} + i_A i_{br1} + i_B i_{cr1} + i_C i_{dr1} + i_D i_{er1}\right)\sin(\theta_1+\alpha) + \\ \left(i_D i_{ar1} + i_E i_{br1} + i_A i_{cr1} + i_B i_{dr1} + i_C i_{er1}\right)\sin(\theta_1+2\alpha) + \left(i_C i_{ar1} + i_D i_{br1} + i_E i_{cr1} + i_A i_{dr1} + i_B i_{er1}\right) \\ \sin(\theta_1-2\alpha) + \left(i_B i_{ar1} + i_C i_{br1} + i_D i_{cr1} + i_E i_{dr1} + i_A i_{er1}\right)\sin(\theta_1-\alpha) \end{Bmatrix}$$

$$T_{e2} = -P_2 M_2 \begin{Bmatrix} \left(i_A i_{ar2} + i_D i_{br2} + i_B i_{cr2} + i_E i_{dr2} + i_C i_{er2}\right)\sin\theta_2 + \left(i_C i_{ar2} + i_A i_{br2} + i_D i_{cr2} + i_B i_{dr2} + i_E i_{er2}\right)\sin(\theta_2+\alpha) + \\ \left(i_E i_{ar2} + i_C i_{br2} + i_A i_{cr2} + i_D i_{dr2} + i_B i_{er2}\right)\sin(\theta_2+2\alpha) + \left(i_B i_{ar2} + i_E i_{br2} + i_C i_{cr2} + i_A i_{dr2} + i_D i_{er2}\right) \\ \sin(\theta_2-2\alpha) + \left(i_D i_{ar2} + i_B i_{br2} + i_E i_{cr2} + i_C i_{dr2} + i_A i_{er2}\right)\sin(\theta_2-\alpha) \end{Bmatrix} \quad (20)$$

In order to simplify the phase-domain model, the decoupling transformation is applied. The new variables are defined as:

$$\underline{v}_{\alpha\beta}^{INV} = \underline{C}\underline{v}^{INV}, \quad \underline{v}_{\alpha\beta}^{r1} = \underline{C}\underline{v}^{r1}, \quad \underline{v}_{\alpha\beta}^{r2} = \underline{C}\underline{v}^{r2} \quad \underline{i}_{\alpha\beta}^{INV} = \underline{C}\underline{i}^{INV}, \quad \underline{i}_{\alpha\beta}^{r1} = \underline{C}\underline{i}_{r1}, \quad \underline{i}_{\alpha\beta}^{r2} = \underline{C}\underline{i}_{r2} \quad (21)$$

The Clark's decoupling transformation matrix in power invarient form is:

$$\underline{C} = \sqrt{\frac{2}{5}} \begin{array}{c} \alpha \\ \beta \\ x \\ y \\ 0 \end{array} \begin{bmatrix} 1 & \cos\alpha & \cos 2\alpha & \cos 3\alpha & \cos 4\alpha \\ 0 & \sin\alpha & \sin 2\alpha & \sin 3\alpha & \sin 4\alpha \\ 1 & \cos 2\alpha & \cos 4\alpha & \cos 6\alpha & \cos 8\alpha \\ 0 & \sin 2\alpha & \sin 4\alpha & \sin 6\alpha & \sin 8\alpha \\ 1/\sqrt{2} & 1/\sqrt{2} & 1/\sqrt{2} & 1/\sqrt{2} & 1/\sqrt{2} \end{bmatrix} \quad (22)$$

The inverter/stator voltage equations are:

$$v_\alpha^{INV} = \left(R_{s1}+R_{s2}\right)i_\alpha^{INV} + \left(L_{ls1}+L_{ls2}+L_{m1}\right)\frac{di_\alpha^{INV}}{dt} + L_{m1}\cos\left(\theta_1\right)\frac{di_{\alpha r1}}{dt} - L_{m1}\sin\left(\theta_1\right)\frac{di_{\beta r1}}{dt} - \omega_1 L_{m1}\left(\sin\left(\theta_1\right)i_{\alpha r1} + \cos\left(\theta_1\right)i_{\beta r1}\right)$$

$$v_\beta^{INV} = \left(R_{s1}+R_{s2}\right)i_\beta^{INV} + \left(L_{ls1}+L_{m1}+L_{ls2}\right)\frac{di_\beta^{INV}}{dt} + L_{m1}\sin\left(\theta_1\right)\frac{di_{\alpha r1}}{dt} + L_{m1}\cos\left(\theta_1\right)\frac{di_{\beta r1}}{dt} + \omega_1 L_{m1}\left(\cos\left(\theta_1\right)i_{\alpha r1} - \sin\left(\theta_1\right)i_{\beta r1}\right)$$

$$v_x^{INV} = \left(R_{s1}+R_{s2}\right)i_x^{INV} + \left(L_{ls1}+L_{ls2}+L_{m2}\right)\frac{di_x^{INV}}{dt} + L_{m2}\cos\left(\theta_2\right)\frac{di_{\alpha r2}}{dt} - L_{m2}\sin\left(\theta_2\right)\frac{di_{\beta r2}}{dt} - \omega_2 L_{m2}\left(\sin\left(\theta_2\right)i_{\alpha r2} + \cos\left(\theta_2\right)i_{\beta r2}\right)$$

$$v_y^{INV} = \left(R_{s1}+R_{s2}\right)i_y^{INV} + \left(L_{ls1}+L_{ls2}+L_{m2}\right)\frac{di_y^{INV}}{dt} + L_{m2}\sin\left(\theta_2\right)\frac{di_{\alpha r2}}{dt} + L_{m2}\cos\left(\theta_2\right)\frac{di_{\beta r2}}{dt} + \omega_2 L_{m2}\left(\cos\left(\theta_2\right)i_{\alpha r2} - \sin\left(\theta_2\right)i_{\beta r2}\right)$$

$$v_0^{INV} = \left(R_{s1}+R_{s2}\right)i_0^{INV} + \left(L_{ls1}+L_{ls2}\right)\frac{di_0^{INV}}{dt} \quad (23)$$

The rotor voltage equations of machine 1:

$$v_{\alpha r1} = 0 = R_{r1}i_{\alpha r1} + L_{m1}\cos\left(\theta_1\right)\frac{di_\alpha^{INV}}{dt} + L_{m1}\sin\left(\theta_1\right)\frac{di_\beta^{INV}}{dt} + \left(L_{lr1}+L_{m1}\right)\frac{di_{\alpha r1}}{dt} - \omega_1 L_{m1}\left(\sin\left(\theta_1\right)i_\alpha^{INV} - \cos\left(\theta_1\right)i_\beta^{INV}\right)$$

$$v_{\beta r1} = 0 = R_{r1}i_{\beta r1} - L_{m1}\sin\left(\theta_1\right)\frac{di_\alpha^{INV}}{dt} + L_{m1}\cos\left(\theta_1\right)\frac{di_\beta^{INV}}{dt} + \left(L_{lr1}+L_{m1}\right)\frac{di_{\beta r1}}{dt} - \omega_1 L_{m1}\left(\cos\left(\theta_1\right)i_\alpha^{INV} + \sin\left(\theta_1\right)i_\beta^{INV}\right)$$

$$v_{xr1} = 0 = R_{r1}i_{xr1} + L_{lr1}\frac{di_{xr1}}{dt}$$

$$v_{yr1} = 0 = R_{r1}i_{yr1} + L_{lr1}\frac{di_{yr1}}{dt} \quad (24)$$

$$v_{0r1} = 0 = R_{r1}i_{0r1} + L_{lr1}\frac{di_{0r1}}{dt}$$

The rotor voltage equations of machine 2:

$$v_{\alpha r2} = 0 = R_{r2}i_{\alpha r2} + L_{m2}\cos\left(\theta_2\right)\frac{di_x^{INV}}{dt} + L_{m2}\sin\left(\theta_2\right)\frac{di_y^{INV}}{dt} + \left(L_{lr2} + L\right.$$

$$v_{\beta r2} = 0 = R_{r2}i_{\beta r2} - L_{m2}\sin\left(\theta_2\right)\frac{di_x^{INV}}{dt} + L_{m2}\cos\left(\theta_2\right)\frac{di_y^{INV}}{dt} + \left(L_{lr2}+L_{m2}\right)\frac{di_{\beta r2}}{dt} - \omega_2 L_{m2}\left(\cos\left(\theta_2\right)i_x^{INV} + \sin\left(\theta_2\right)i_y^{INV}\right)$$

$$v_{xr2} = 0 = R_{r2} i_{xr2} + L_{lr2} \frac{di_{xr2}}{dt} \tag{25}$$

$$v_{yr2} = 0 = R_{r2} i_{yr2} + L_{lr2} \frac{di_{yr2}}{dt}$$

$$v_{0r2} = 0 = R_{r2} i_{0r2} + L_{lr2} \frac{di_{0r2}}{dt}$$

The electromagnetic torque equations:

$$T_{e1} = P_1 L_{m1} \left\{ \cos(\theta_1)\left(i_{\alpha r1} i_{\beta}^{INV} - i_{\beta r1} i_{\alpha}^{INV}\right) - \sin(\theta_1)\left(i_{\alpha r1} i_{\alpha}^{INV} + i_{\beta r1} i_{\beta}^{INV}\right) \right\}$$

$$T_{e2} = P_2 L_{m2} \left\{ \cos(\theta_2)\left(i_{\alpha r2} i_{y}^{INV} - i_{\beta r2} i_{x}^{INV}\right) - \sin(\theta_2)\left(i_{\alpha r2} i_{x}^{INV} + i_{\beta r2} i_{y}^{INV}\right) \right\} \tag{26}$$

IV. SENSORLESS OPERATION OF SERIES-CONNECTED TWO FIVE-PHASE INDUCTION MACHINES

The developed model of a series-connected two five-phase induction machines indicates that an observer used for five-phase machines can be easily extended to multi-phase , multi-motor machines. For multi-phase machines observer -based speed estimator requires only *d* and *q* components of stator voltages and currents for first machine. From the model of a five-phase induction machine , it has been shown that the stator and rotor *d* and *q* axis flux linkages are function of magnetising inductance *Lm* and stator and rotor *d* and *q* axis currents, where as the *x* and *y* axis flux linkages are function of only their respective currents. Therefore in speed estimation for multi-phase multi-motor machine the *x* and *y* components of voltages and currents are required for speed estimation of second machine. Therefore speeds can be estimated using *d-q* and x-y components of stator voltages and currents. A principal block-diagram of the sensorless control of series-connected five-phase two-motor drive system is shown in Fig. 3.

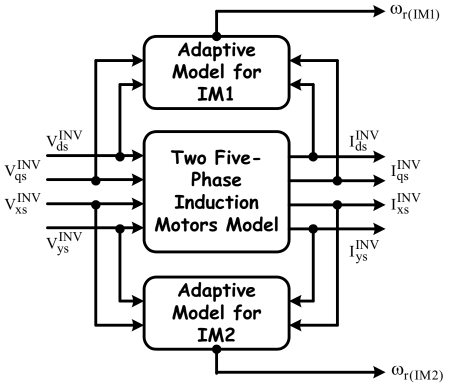

Fig. 3: Sensorless control of Series connected two five-phase machines.

V. OBSERVER-BASED SPEED ESTIMATOR

A state observer is a model-based state estimator which can be used for the state and/or parameter estimation of a non-linear dynamic system in real time. In the calculations, the states are predicted by using a mathematical model , but the predicted states are continuously corrected by using a feed back correction scheme. The actual measured states are denoted by x and the estimated states by $\hat{\mathrm{x}}$. The correction term contains the weighted difference of some of the measured and estimated outputs signals (the difference is multiplied by the observer feedback gain, **G**). The accuracy of the state observer also depends on the model parameters used. The state observer is simpler than the Kalman observer, since no attempt is made to minimize a stochastic cost criterion.

To obtain the full-order non-linear speed observer, first the model of the induction machine is considered in the stationary reference frame, which can be described as follows:

$$\frac{dx}{dt} = Ax + Bv \tag{27}$$

and the output vector is

$$i_s = Cx \tag{28}$$

By using the derived mathematical model of the induction machine, e.g. if the component form of the equations (27), is used, since this is required in an actual implementation and adding the correction term , which contains the difference of actual and estimated states, a full-order state observer, which estimates the stator currents and rotor flux linkages, can be described as follows:

$$\frac{d\hat{x}}{dt} = A\hat{x} + Bv + G(i_s - \hat{i}_s) \tag{29}$$

and the output vector is

$$\hat{i}_s = C\hat{x} \tag{30}$$

where A is a state matrix , B is the input matrix, G is the observer gain matrix, C is the output matrix, x is the state vector, v is the input vector, $\mathrm{i_s}$ stator current vector.

Also the state matrix of the observer ($\hat{\mathrm{A}}$) is a function of the rotor speed, and in a speed–sensorless drive, the rotor speed must be estimated. The estimated rotor speed is denoted by $\hat{\omega}_{\mathrm{r}}$, and in general $\hat{\mathrm{A}}$ is a function of $\hat{\omega}_{\mathrm{r}}$. The estimated speed is considered as a parameter in $\hat{\mathrm{A}}$, however in extended Kalman filter considered as a state variable. In eqns (27) and (28) the different terms are explained as follows:

$$\hat{A} = \begin{bmatrix} -\left[1/T_s^{'} + (1-\sigma)/T_r^{'}\right] I_2 & \left[L_m /(L_s^{'} L_r)\right]\left[I_2 / T_r - \hat{\omega}_r J\right] \\ L_m I_2 / T_r & -I_2 / T_r + \hat{\omega}_r J \end{bmatrix}$$

$$B = \left[I_2 / L_s^{'}, O_2\right]^T$$

$$C = \left[I_2, O_2\right]^T$$

$$v^{INV} = v_s^{INV} = \left[v_{\alpha s}^{INV}, v_{\beta s}^{INV}\right]^T \tag{31}$$

$$\hat{x} = \left[\hat{i}_s, \hat{\psi}'_r\right]^T$$

$$i_s^{INV} = \left[i_{\alpha s}^{INV}, i_{\beta s}^{INV}\right]^T, \quad \hat{i}_s = \left[\hat{i}_{\alpha s}, \hat{i}_{\beta s}\right]^T$$

$$J = \begin{bmatrix} 0 & -1 \\ 1 & 0 \end{bmatrix}$$

$I_2 = \mathrm{diag}(1,1)$, is a second order identity matrix.
O_2, is a 2x2 zero matrix.

In state matrix $\hat{A}$, the different terms are as follows:

L_m and L_r are the magnetising inductance and rotor self-inductance respectively, L'_s is the stator transient inductance, $T'_s = L'_s / R_s$ and $T'_r = L'_r / R_r$ are the stator and rotor transient time constants respectively, and $\sigma = 1 - L_m^2 / (L_s L_r)$ is the leakage factor.

The observer gain matrix is defined as

$$G = -\begin{bmatrix} g_1 I_2 + g_2 J \\ g_3 I_2 + g_4 J \end{bmatrix}$$

which yields a 2x4 matrix. The four gains in G can be obtained from the eigen-values of the induction motor as follows:

$$g_1 = -(k-1)\left(\frac{1}{T'_s} + \frac{1}{T'_r}\right)$$

$$g_2 = (k-1)\hat{\omega}_r$$

$$g_3 = (k^2-1)\left\{-\left[\frac{1}{T'_s} + \frac{(1-\sigma)}{T'_r}\right]\frac{L'_s L_m}{L_r} + \frac{L_m}{T_r}\right\} \tag{32}$$

$$+\frac{L'_s L_m}{L_r}(k-1)\left(\frac{1}{T'_s} + \frac{1}{T'_r}\right)$$

$$g_4 = -(k-1)\hat{\omega}_r \frac{L'_s L_m}{L_r}$$

It follows that the four gains depend on the estimated speed, $\hat{\omega}_r$. By using eqns (27) and (28) it is possible to implement a speed estimator which estimates the rotor speed of an induction machine by using the adaptive state observer shown in Fig. 4 [16].

In Fig. 4 the estimated rotor flux-linkage components and the stator current error components are used to obtain the error speed tuning signal and given by equations:

$\underline{\hat{\psi}}_r = \hat{\psi}_{\alpha r} + j\hat{\psi}_{\beta r}$ and $\underline{e} = e_{\alpha s} + je_{\beta s}$. The estimated speed is obtained from the speed tuning signal by using a PI controller thus,

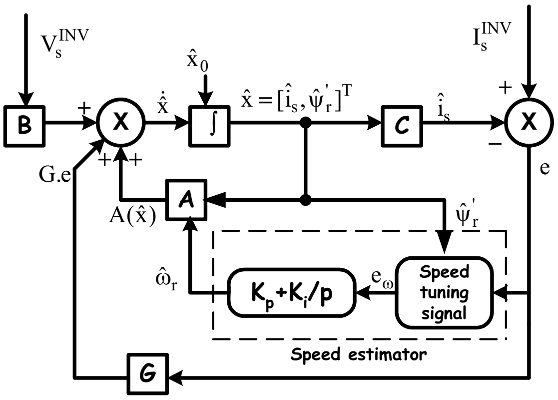

Fig. 4: Adaptive speed observer (speed-adaptive flux observer)

$$\hat{\omega}_r = K_p(\hat{\psi}_{\beta r} e_{\alpha s} - \hat{\psi}_{\alpha r} e_{\beta s}) + K_i \int (\hat{\psi}_{\beta r} e_{\alpha s} - \hat{\psi}_{\alpha r} e_{\beta s}) dt \tag{33}$$

where K_p and K_i are proportional and integral gain constants respectively, $e_{\alpha s} = i_{\alpha s}^{INV} - \hat{i}_{\alpha s}$ and $e_{\beta s} = i_{\beta s}^{INV} - \hat{i}_{\beta s}$ are the stator current errors respectively.
The adaptation mechanism is similar to that as used in the MRAS-based speed estimators, where the speed adaptation has been obtained by using the state-error equations of the system considered.
In the expressions $\alpha = d$ and $\beta = q$ for first machine and $\alpha = x$ and $\beta = y$ for second machine.

VI. SIMULATION RESULTS

The results of the simulation given in this section are obtained using two identical 4-pole, 50 Hz five-phase induction machines. The indirect vector controller for both machines is the same and is the one shown in figure 2. Various simulation tests are performed in order to verify the independence of the control of the two machines. The results are reported in this section. Operation in the base speed region only is considered and the stator d-axis current references of both machines are constant at all times. Both machines are running under load conditions. Both machines can be operated in two ways:

A. *Fixed voltage and fixed frequency supply*

In this case both machines are connected to two five-phase supply system. If the supply voltages for machine-1 are $v_{a1}, v_{b1}, v_{c1}, v_{d1}, v_{e1}$ and for machine-2 are $v_{a2}, v_{b2}, v_{c2}, v_{d2}, v_{e2}$ then the resultant supply voltages applied to the series-connected two motors are $V_A = v_{a1} + v_{a2}$, $V_B = v_{b1} + v_{c2}$, $V_C = v_{c1} + v_{e2}$, $V_D = v_{d1} + v_{b2}$, $V_E = v_{e1} + v_{d2}$.
The simulation time for test is 2 sec. and both machines are loaded simultaneously at t=1.2s. The machines are running under acceleration transient and steady-state at no-load and load conditions. Both the machines are running under different test conditions to verify the decoupling of both machines. The corresponding test results are shown in figure 5(a) to (f). Each test results shows both reference and estimated speeds for IM1 and IM2.

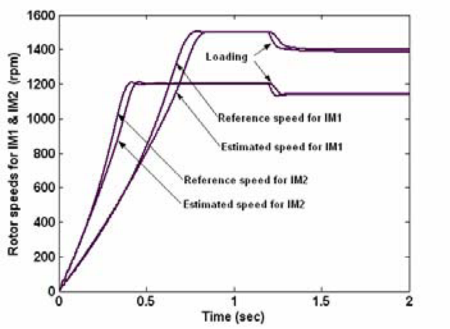

(a)

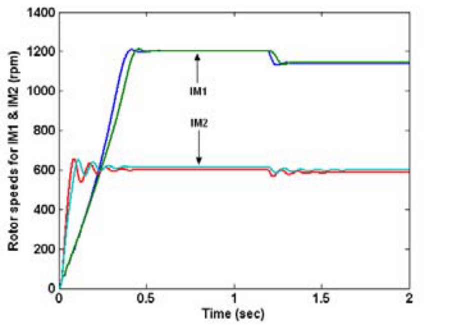

(b)

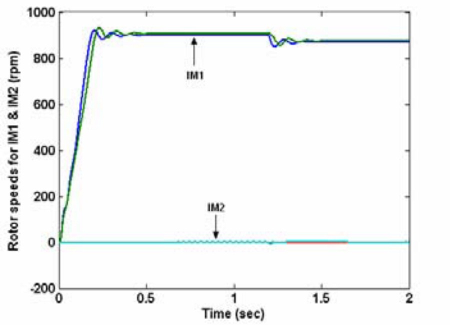

(c)

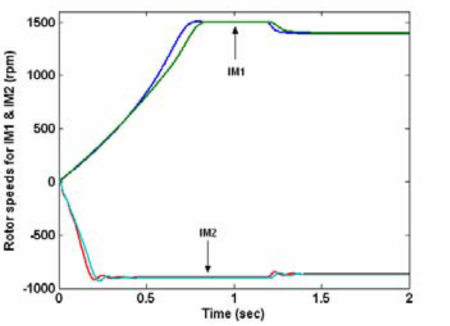

(d)

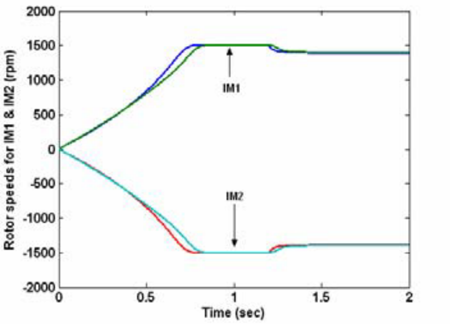

(e)

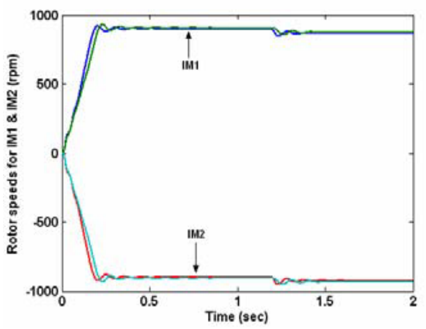

(f)

Fig. 5: Speed responses for fixed voltage and fixed frequency series connected two motors system.

B. Vector controlled series-connected two motors:

In this case both machines are vector controlled. Two vector controller are used for control of series connected two motors. If the output currents of first controller for IM-1 are $i^*_{a1}, i^*_{b1}, i^*_{c1}, i^*_{d1}, i^*_{e1}$ and the output currents of second controller for IM-2 are $i^*_{a2}, i^*_{b2}, i^*_{c2}, i^*_{d2}, i^*_{e2}$ then the resultant supply currents applied to the series-connected two motors are

$$i^*_A = i^*_{a1} + i^*_{a2} \qquad i^*_B = i^*_{b1} + i^*_{c2}$$

$$i^*_C = i^*_{c1} + i^*_{e2} \qquad i^*_D = i^*_{d1} + i^*_{b2}$$

$$i^*_E = i^*_{e1} + i^*_{d2}$$

The simulation time for test is 2 sec. and both machines are loaded simultaneously at t=1s. The machines are running under acceleration transient from t=0.3s and 0.4s and steady-state at no-load and load conditions.

Both the machines are reversing from t=1.2s and 1.3s. Both the machines are running under different test condition to verify the decoupling of both machines. The corresponding test results are shown in figure 6(a) to (f). Each test results shows both reference and estimated speeds for IM1 and IM2.

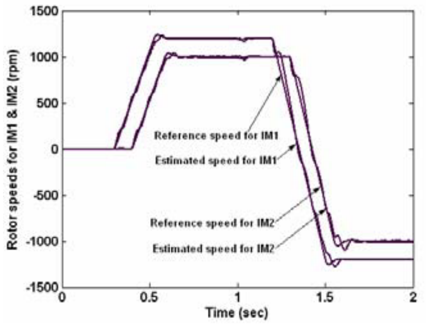

(a)

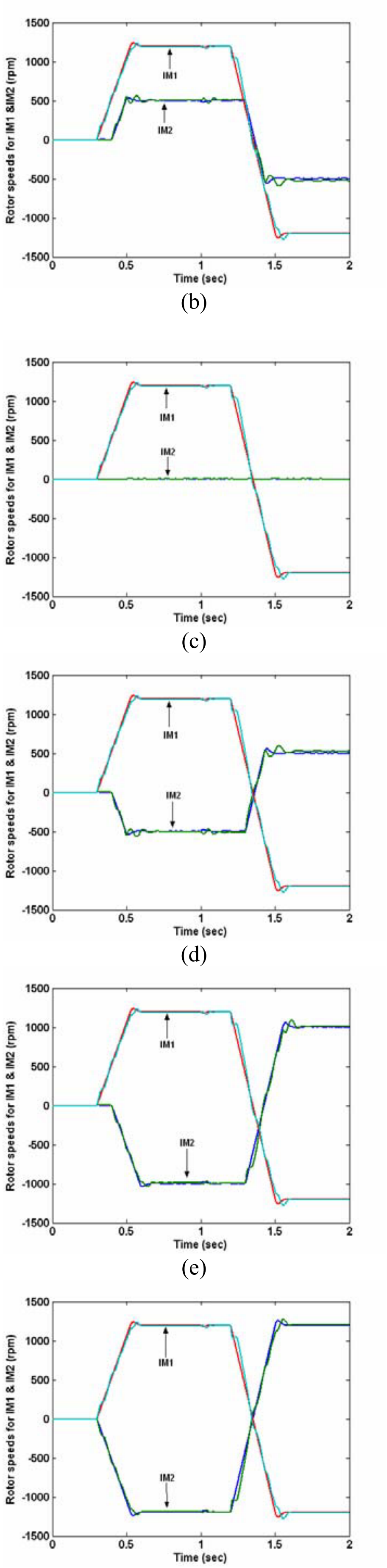

(b)

(c)

(d)

(e)

(f)

Fig. 6: Speed responses for vector-controlled series connected two motors system.

VII. Discussion

Fig. 5(a) to (f) shows the test results for fixed voltage and fixed frequency supply fed series connected two motor system. In first test fig. (a), IM1 is running at 1500 rpm and IM2 at 1200 rpm and both machines are loaded at t=1s. In fig. (b), IM1 is running at 1200 rpm and IM2 at 600 rpm. In fig. (c), IM1 is running at 900 rpm and IM2 at 0 rpm. In fig. (d), IM1 is running at 1500 rpm and IM2 at -900 rpm. In fig. (e), IM1 and IM2 both are running at 1500 rpm but in opposite direction. In fig. (f), IM1 and IM2 both are running at 900 rpm but in opposite direction.

These test results shows that when machine is running at higher speed then there is settling time delay of around 0.1sec. Also under loading condition, a 10rpm difference can be seen. As the speed decreases the settling time delay decreases but ripples in response increases in both conditions i.e. no-load and load conditions. This discussion is true for both conditions i.e. when machine is running in forward direction or in reverse direction. These test results also shows that both machines IM1 and IM2 are independently controlled even in sensorless mode.

Fig. 6(a) to (f) shows the test results for vector controlled series connected two motor system. In all test, IM1 is set at ±1200 rpm and both machines are loaded at t=1.0s. In first test fig. (a), IM2 is set at ±1000 rpm. In fig. (b), IM2 is set at ±500 rpm. In fig. (c), IM2 is set at 0 rpm. In fig. (d), IM2 is set at ∓ 500 rpm. In fig. (e), IM2 is set at ∓ 1000 rpm. In fig. (f), IM2 is set at ∓ 1200 rpm. In vector controlled the settling time error is very small as compare to ideal supply fed machine. Also in vector controlled there is no speed error in loading condition. But when speed decreases then ripples in speed response increases under both forward and reversing conditions. These test results again shows that both machines IM1 and IM2 are independently controlled in vector controlled technique in sensorless mode.

VIII. Conclusion

The paper discusses a series-connected five-phase two-motor drive and provides full simulation verification of the possibility of independent fixed voltage and fixed frequency supply and vector control of the two machines in sensorless mode. A brief review of the operating principles is provided. The emphasis is further placed on presentation of simulation results for various transients (acceleration, deceleration and speed reversal). By presenting the results of series-connected two-motor five-phase drive it is fully verified that the control of the two series-connected machines is truly decoupled even in sensorless mode.

The investigated drive structure is applicable to all types of five-phase ac machine with sinusoidal flux distribution. It is believed that the best prospect for real-world industrial applications exists in the winder area, where the series-connected two-motor drive could provide a substantial saving on the capital outlay, especially if permanent magnet synchronous machines are used. Although the efficiency of the complete system remains affected by the series connection, there should be no need to de-rate the motors due to the increase in stator winding losses.

ACKNOWLEDGEMENT

The authors gratefully acknowledge support provided for the work on this project by the AICTE, File No. 8023/BOR/RPS-86/2006-07.

REFERENCES

[1] Williamson, S. and Smith, S.: ‘Pulsating torques and losses in multiphase induction machines’, IEEE Trans. on Industry Applications, vol. 39, no. 4, 2003, pp. 986-993.

[2] Green, S., Atkinson, D.J., Jack, A.G., Mecrow, B.C. and King, A.: ‘Sensorless operation of a fault tolerant PM drive’, IEE Proc. – Electr. Power Appl., Vol. 150, No. 2, 2003, pp. 117-125.

[3] Wang, J.B., Atallah, K and Howe, D.: ‘Optimal torque control of fault-tolerant permanent magnet brushless machines’, IEEE Trans. on Magnetics, Vol. 39, No. 5, 2003, pp. 2962-2964.

[4] Gataric, S.: ‘A polyphase Cartesian vector approach to control of polyphase AC machines’, Proc. IEEE Ind. Appl. Soc. Annual Meeting IAS, Rome, Italy, 2000, Paper No. 38-02

[5] Levi, E., Jones, M. and Vukosavic, S.N.: ‘Even-phase multi-motor vector controlled drive with single inverter supply and series connection of stator windings’, IEE Proc. - Electric Power Applications, Vol. 150, No. 5, 2003, pp. 580-590.

[6] E.Levi, M.Jones, S.N.Vukosavic, and H.A.Toliyat, “A novel concept of a multi-phase, multi-motor vector controlled drive system supplied from a single voltage source inverter,” IEEE Trans. on Power Electronics, Vol. 19, 2004, pp. 320-335.

[7] Levi, E., Jones, M., Vukosavic, S.N. and Toliyat, H.A.: ‘Operating principles of a novel multi-phase multi-motor vector controlled drive’, IEEE Trans. on Energy Conversion, Vol. 19, No. 3, 2004, pp. 508-517.

[8] Mohapatra, K.K., Baiju, M.R. and Gopakumar, K.: ‘Independent speed control of two six-phase induction motors using a single six-phase inverter’, EPE Journal, Vol. 14, No. 3, 2004, pp. 49-62.

[9] Levi, E., Vukosavic, S.N. and Jones, M.: ‘Vector control schemes for series-connected six-phase two-motor drive systems’, IEE Proc. – Electric Power Applications, Vol. 152, No. 2, 2005, pp. 226-238.

[10] Levi, E., Jones, M., Vukosavic, S.N. and Toliyat, H.A.: ‘A five-phase two-machine vector controlled induction motor drive supplied from a single inverter’, EPE Journal, Vol. 14, No. 3, 2004, pp. 38-48.

[11] Levi, E., Jones, M., Vukosavic, S.N., Iqbal A. and Toliyat, H.A.: ‘Modeling , Control and Experimental Investigation of a five-phase series-connected two-motor drive with single inverter supply’, IEEE Trans. On Industrial Electronics, Vol. 54, No. 3, June 2007, pp. 1504-1516.

[12] Levi, E., Jones, M., Iqbal A. and Toliyat, H.A.: ‘An induction machine/Syn-Rel two-motor five-phase series-connected drive’, IEEE Trans. On Energy Conversion, Vol. 22, No. 2, June 2007, pp. 281-289.

[13] Levi, E., Iqbal, A., Vukosavic, S.N. and Toliyat, H.A.: ‘Modelling and control of a five-phase series-connected two-motor drive’, IEEE Ind. Elec. Soc. Annual Meeting IECON, Roanoke, VA, 2003, pp. 208-213.

[14] Jones, M., Levi, E. and Iqbal, A.: ‘Vector control of a five-phase series-connected two-motor drive using synchronous current controllers’, Electric Power Comp. & Systems, Vol. 33, No. 4, 2005, pp. 411-430.

[15] Jones, M., Vukosavic, S.N., Levi, E. and Iqbal, A.: ‘A novel six-phase series-connected two-motor drive with decoupled dynamic control’, IEEE Industry Applications Society Annual Meeting IAS, Seattle, WA, Vol. 41, No. 4, 2004, pp. 639-646 .

[16] Vas, P.: ‘Sensorless Vector and Direct Torque Control’ (Oxford University Press,1998).

[17] Rajashekara, K., Kawamura, A. and Matsuse, K.: ‘Sensorless Control of AC Motors, Eds. Piscataway’(NJ: IEEE Press, 1996).

[18] Green, S., Atkinson, A.G., Mecrow, B.C. and King, A.: ‘Sensorless Operation of a Fault Tolerant PM Drives’, IEE Proc. Elect. Power application, Vol.150, No.2, 2000, pp.117-125.

[19] White, D.C. and Woodson, H.H.: ‘Electromechanical Energy Conversion’ (New York, John Wiley & Sons,1959).

[20] Jansen, P.L. and Lorenz, R.D.: ‘A physically insightful approach to the design and accuracy assessment of flux observers for field oriented induction machine drives’, IEEE Trans. Ind. Appl., Vol. 30, No. 1, Jan./Feb. 1994, pp. 101–110,.

[21] Profumo, F., Griva, G., Tenconi, A., Abrate**,** M., and Ferraris, L.: ‘Stability analysis of Luenberger observers for speed sensorless high performance spindle drives’, European Conf. on Power Electronics and Applications, EPE’99, Lausanne, Switzerland, 1999, CD-ROM Paper No. 604

[22] Kubota, H., Sato, I., Tamura, Y., Matsuse, K., Ohta, H. and Hori, Y.: ‘Stable operation of adaptive observer based sensorless induction motor drives in regenerating mode at low speeds’, in Conf. Rec. IEEE-IAS Annu. Meeting, Chicago, IL, Oct. 2001, pp. 469–474.

[23] Matlab/Simulink reference guide www.mathworks.co.uk.

BIOGRAPHIES

M. Rizwan Khan received his B.Sc. Engineering and M.Tech. (Electrical) degrees in 1998 and 2001, respectively, from the Aligarh Muslim University, Aligarh, India. He is working as Lecturer in the Department of Electrical Engineering, Aligarh Muslim University, Aligarh since 2001 and currently pursuing his Ph.D. His principal area of research interest is Power Electronics, Artificial Intelligence and Multi-phase motor drives.

Atif Iqbal received his B.Sc. and M.Sc. Engineering (Electrical) degrees in 1991 and 1996, respectively, from the Aligarh Muslim University, Aligarh, India and PhD in 2005 from Liverpool John Moores University, Liverpool, UK. He has been employed as Lecturer in the Department of Electrical Engineering, Aligarh Muslim University, Aligarh since 1991 and is currently working as a Reader in the same university. He is recipient of Maulana Tufail Ahmad Gold Medal for standing first at B.Sc. Engg. Exams in 1991, AMU and research fellowship from EPSRC,UK for pursuing Ph.D. studies. His principal area of research interest is Power Electronics and Multi-phase machine drives.

IGBT Based Cyclo-Inverter

Vineeta Agarwal[1] and Peeyush Agarwal[1]

Abstract - This paper proposes a novel, power electronics system, an IGBT based Cyclo-Inverter, capable of converting power at the main frequency to a higher frequency. It finds its application in induction heating, fluorescent lighting, ballast, high frequency power supplies and so many other applications where high frequency reduces the size of equipment. A methodology is developed to generate the trigger signals for various IGBTs used in the cyclo-inverter such that the circuit is not restricted to a particular value of output frequency but it can produce any output frequency that is an integer multiple of the input supply frequency. Hardware design is obtained using readily available ICs and other components. The trigger circuit has been tested qualitatively by observing various waveforms on CRO. The operation of proposed system has been found to be satisfactory.

Keywords - Cyclo-Inverter, IGBT, Triggering Pulses, Zero Crossing Detector (ZCD), Operational Amplifier (OPAMP)

I. INTRODUCTION

Developments in the field of DC to AC converter or inverter circuit are a subject of investigation. A wide variety of inverter circuits are possible depending upon the output frequency and voltage [1-4]. Simplest is the single-phase bridge inverter circuit. The output voltage waveform is fairly square and contains harmonics. [5]. Most applications of DC to AC converter prefer a sine wave rather than a square wave output [6]. Sine wave output may be obtained from resonant inverters or load commutated inverters [7- 8]. A unique advantage of this type of inverter is that device-switching loss is eliminated and therefore, the inverter can operate at high frequency (200 Hz to 100 kHz) with high efficiency. One of the main disadvantages with this circuit is that high rating is required for the commutating components because they carry the load current continuously.

In this paper an attempt has been made to design direct AC-to-AC converter or cyclo-inverter, which uses self commutated device IGBT and eliminates the need for external commutation circuit. The converter is suitable for heating and melting applications [9], active power filters, low EMI, high power density UPS and so on. Trigger requirements are obtained for single-phase centre tapped transformer configuration. Hardware design is obtained using readily available ICs and other components. Experiment results are presented for a resistive load.

II. PROPOSED CONVERTER

Fig. 1 shows the detailed circuit of the proposed converter. It consists of two converters a positive converter PC and a negative converter NC connected in anti parallel. IGBTs 1 and 2 form positive converter whereas IGBTs 3 and 4 form negative converter, NC. Output is obtained through proper conduction of IGBTs in the two input cycles. For example, to generate an output frequency double to the input frequency a firing sequence of 14, 23, 14, …, and so on, is adopted whereas for an output frequency of three times that of input frequency, this firing sequence becomes 141, 323, 141, …, and so on. Thus, the output of converter will have a frequency, $f_o = f_i \times N_r$ where N_r is an integer and f_i is the source frequency.

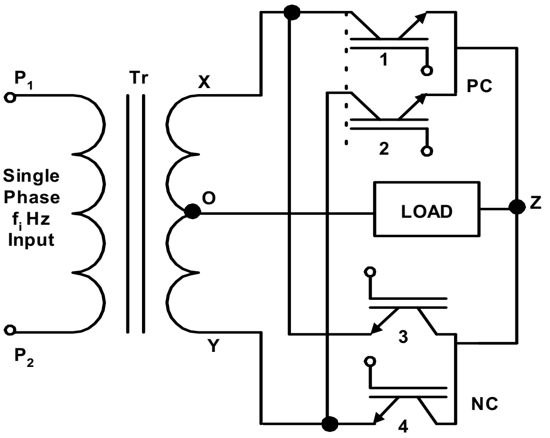

Fig. 1: IGBT Based Frequency Multiplier

Fig. 2 shows the idealized waveform with a firing sequence of 14, 23, and 14, for an output frequency double to the input frequency for a purely resistive load.

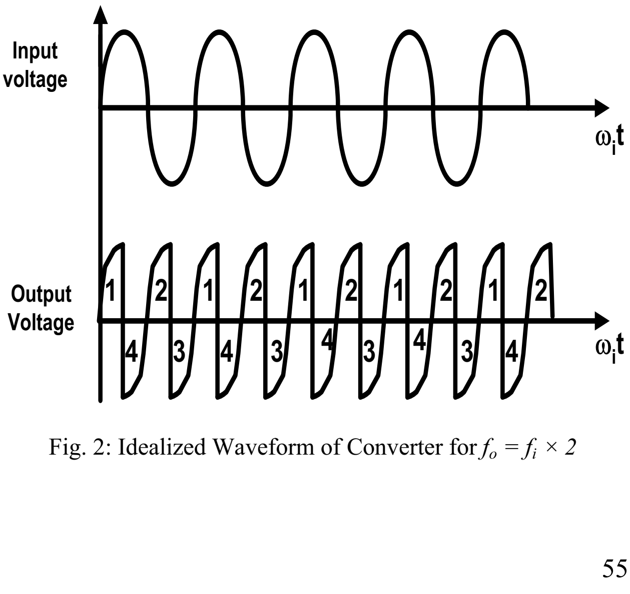

Fig. 2: Idealized Waveform of Converter for $f_o = f_i \times 2$

The paper first received 22 Sep 2006 and in revised form 23 Apr 2007
Digital ref: AI70201140

[1] Department of Electrical Engineering, M.N.N.I.T. Allahabad, 211004, India, Email: vineeta@mnnit.ac.in

III. PRINCIPLE OF TRIGGERING PULSE GENERATION

There is a definite firing sequence for a given value of N_r to generate the high frequency output f_o. Fig. 3 shows the schematic details of the trigger scheme to generate the required high frequency output. The input signal having frequency f_i, which has to be converted into high frequency signal, is stepped down from a step down transformer in input stage. It is then converted into a square signal using Zero Crossing Detector (ZCD). Another reference signal, having frequency f_o is derived directly from a frequency multiplier using a Phase lock loop PLL and a divide by N_r counter. The two signals are then fed to a pulse generator block, which generates the required pulse for IGBT. The output of pulse-wave generator is fed to the driver circuit, which isolates and boosts the level of pulses.

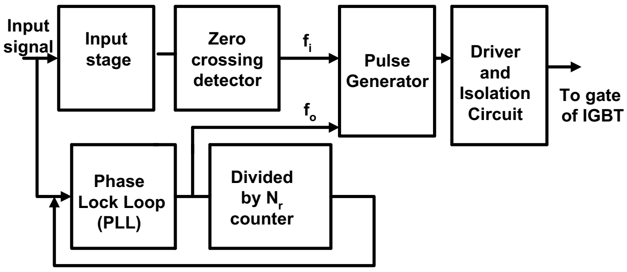

Fig. 3: Block Diagram for trigger pulse generation

The isolated pulses thus obtained, drive the gate of individual IGBTs. The next section illustrates the hardware implementation of this technique.

IV. HARDWARE IMPLEMENTATION

The trigger requirements are obtained for single phase to single phase centre tapped transformer configuration. Block diagram of Fig. 3 has been designed using following sub circuits.

A. Input Stage and Zero Crossing Detector

A step down transformer (220 V/6 V), connected to the main source is used in the input stage of the control circuit. Since the transformer operates at a frequency f_i it provides the desired input frequency reference to the control circuit. The polarity of secondary voltage V_r is matched with that of secondary of power transformer. The voltage V_r is fed to the zero crossing detector (ZCD) as shown in Fig. 4.

A zero crossing detector consists of a comparator, LM 741, suitable to give TTL - compatible output. It compares input voltage V_r with a reference voltage kept at zero. The output is driven into positive saturation when V_r passes zero in positive direction. When V_r changes its direction the output switches and becomes zero. Diodes $D1$ and $D2$ clamp the OPAMP inputs to ± 0.7 V and protect it from damage due to excessive input voltage. The resistance R is selected to limit the current through D_1 and D_2 to safer value of 1.2 mA.

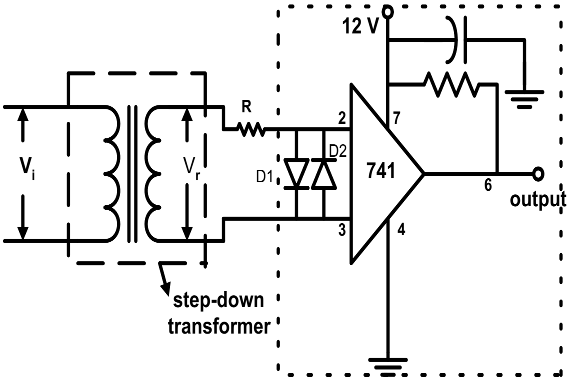

Fig. 4: Input Interfacing Circuit

B. Square Wave Generation at frequency f_o

A square wave output at frequency f_o is generated by using a PLL and a divide by N_r counter. Fig. 5 shows the block diagram for a frequency multiplier using PLL IC 565. It consists of phase comparator, amplifier, low pass filter and VCO. The phase comparator compares the input frequency f_i with the feed back frequency f_o and generates an output signal which is function of the difference between the phases of two input signals. The output signal of the phase comparator is a dc voltage. The output of phase comparator is applied to low pass filter to remove high frequency noise from the dc voltage. This output of the filter is known as error voltage or control voltage for VCO.

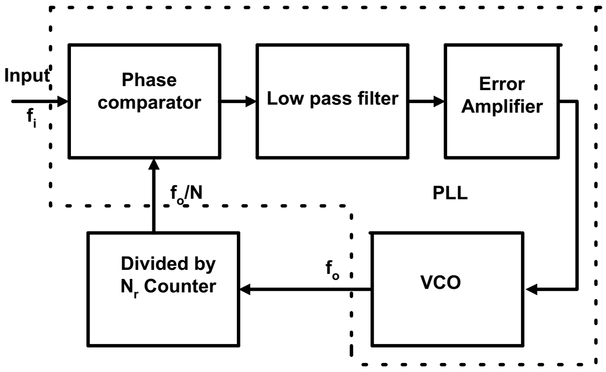

Fig. 5: Block diagram of frequency multiplier using PLL

When control voltage is zero VCO is in free running mode and its output frequency is called as center frequency f_o. The nonzero control voltage results in a shift in the VCO frequency from its free running frequency. f_o to a frequency $f = f_o + K_v\ V_C$, where K_v is the voltage to frequency transfer coefficient of the VCO. The control voltage applied as the input to VCO, forces the VCO to change its output frequency in the direction that reduces the difference between the input frequency and the output frequency of VCO. This action commonly known as capturing continues till the output frequency of VCO is same as the input frequency. Once the two frequencies are same the circuit is locked.

If a divide by N_r counter is inserted between the VCO output and the phase comparator input then the output of the counter will be locked to the input frequency f_i, and VCO will be actually running at a multiple of the input frequency. Therefore, in the locked state, the VCO output frequency f_o is given by

$$f_o = N \times f_i \tag{1}$$

By selecting proper divide by N_r network, desired multiplication is obtained.

Fig. 6 shows the detailed circuit diagram of IC 565 used as a frequency multiplier. The frequency, f_o, of VCO is given by (2)

$$f_o = 0.31/R_oC_o \tag{2}$$

Here R_o and C_o are external resistor and capacitor connected to pins 8 and 9, respectively. The values of R_o and C_o are adjusted such that free running frequency will be at the center of the input frequency range. The value of R_o is restricted from 2 kΩ to 20 kΩ, but a capacitor can have any value. A capacitor C_2 connected between pin 7 and positive supply (pin 10) forms a first order low pass filter with an internal resistance of 3.6 kΩ.

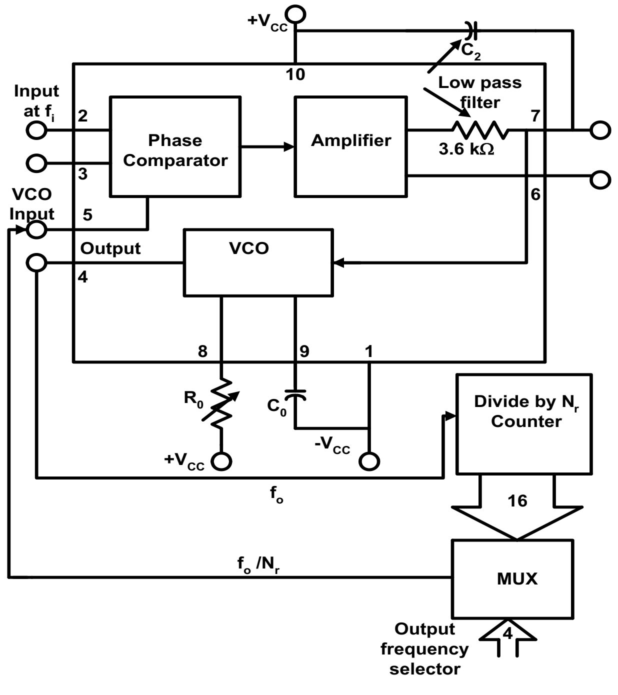

Fig. 6: Detailed circuit diagram of IC 565 used as used as a frequency multiplier

The output of PLL is fed to a divide by N_r counter. The counter counts the output of VCO for a predetermined period defined by the output frequency f_o, and thus toggles at N_r times the output frequency. The counter which has been implemented using a 4 × 16 decoder and 16 mod counters (mod 2, mod 3, ---- up to mod 17), has sixteen separate output channels, one for each N_r. Fig. 7 shows a divide by N_r counter implemented for N_r from 2 to 17. A particular mod counter and output channel is selected by taking a 4 bit word $U_1U_2U_3U_4$ from user and decoding it by a 4× 16 decoder according to the truth table shown in Table 1.

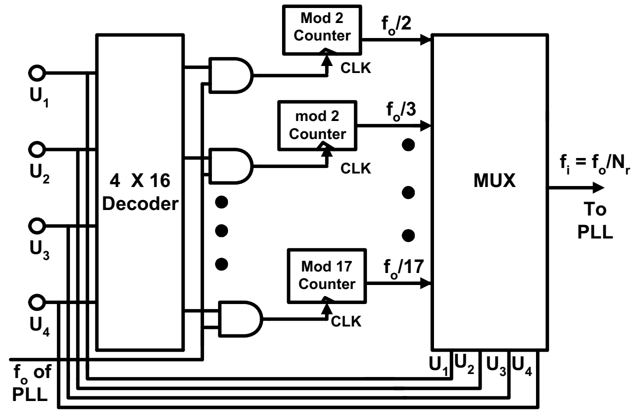

Fig. 7: Divide by N_r counter for N_r from 2 to 17

Table 1 Truth Table for Decoder

U1	U2	U3	U4	N_r
0	0	0	0	2
0	0	0	1	3
0	0	1	0	4
-				
-				
1	1	1	1	17

The maximum count N_r obtainable with the counter corresponds to the maximum output frequency to be generated.

The counter outputs are connected to a 16 to 1 multiplexer. Using four single pole double throw switches generates the four bit multiplexer address. Depending upon the desired output frequency the multiplexer address is selected. The output of MUX is thus at a frequency f_o /N_r which is well synchronized with f_i.

C. *Pulse Wave Generation*

The triggering pulses are different for the same IGBT for different values of N_r. For example for $N_r = 3$, the gating pulses are generated using two set of pulses having frequencies 50 Hz (input supply frequency) and 150 Hz (N_r times the input supply frequency that is desired output frequency) as shown in Fig. 8.

Let X1 represents the pulses at a frequency of 50 Hz and X2 of 150 Hz. Then ANDing of X1 and X2 will result the pulses required by the IGBT T1. Further if this X2 is inverted by a NOT gate, then the ANDing of X1 and X2' will result the pulses required by the IGBT T4. Similarly, ANDing of X1' and X2 result the pulses required by IGBT T2 and then ANDing the X1' and X2' finally generates the required pulses required for IGBT T3.

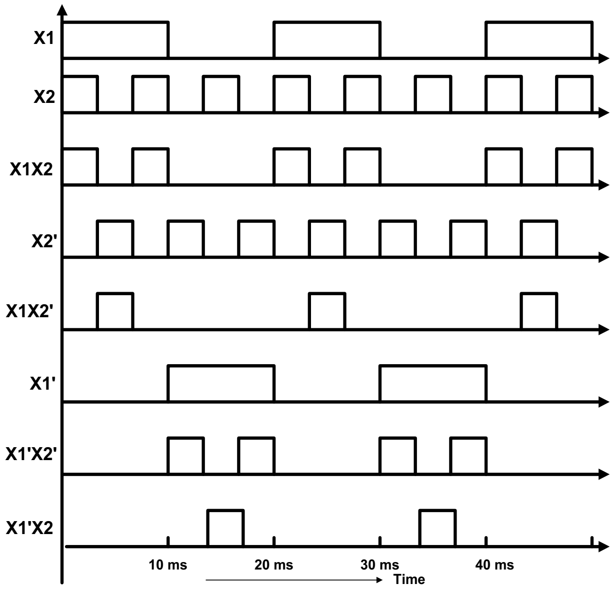

Fig. 8: Gate pulses for Different IGBTs

The circuit diagram to obtain the required pulses is shown in Fig. 9

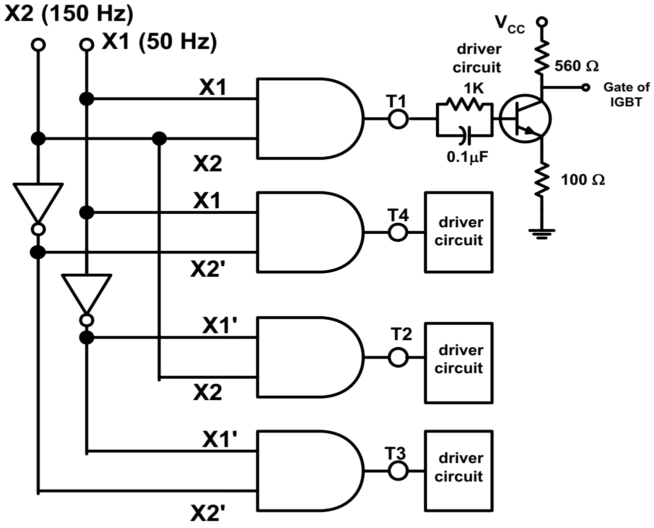

Fig. 9: Circuit Diagram to Generate Gate Pulses

The pulses produced by the pulse wave generator circuit are usually at low power level. They may not be able to trigger the devices into conduction if fed directly. These pulses are therefore boosted to high power level by a circuit known as *driver circuit*. A transistor, in the driver circuit operates in the active region. It is designed to operate in the voltage range of 5 - 20V. As the voltage is increased from 0V to 20Vthe same voltage will appear across the collector and emitter but the voltage across the collector resistance increase only up to 15V for 20V of input. The amplified pulses are isolated using opto-coupler 4N35 and fed to the gate of respective IGBT.

V. EXPERIMENTAL RESULTS

Testing of trigger system and its hardware involves ascertaining that the trigger signals are produced at correct instants. Experimental results are obtained qualitatively by observing the waveforms on CRO at salient points of the control circuit. Fig. 10 shows the complete system diagram of IGBT based cyclo inverter. It consists of a center-tapped transformer, four IGBTs, IRG4PH40UD, with ultra fast soft recovery diode, trigger circuit board, driver circuit and opto couplers for isolation. A variable resistance is used as a load. The input center-tapped transformer rating is 3 kVA.

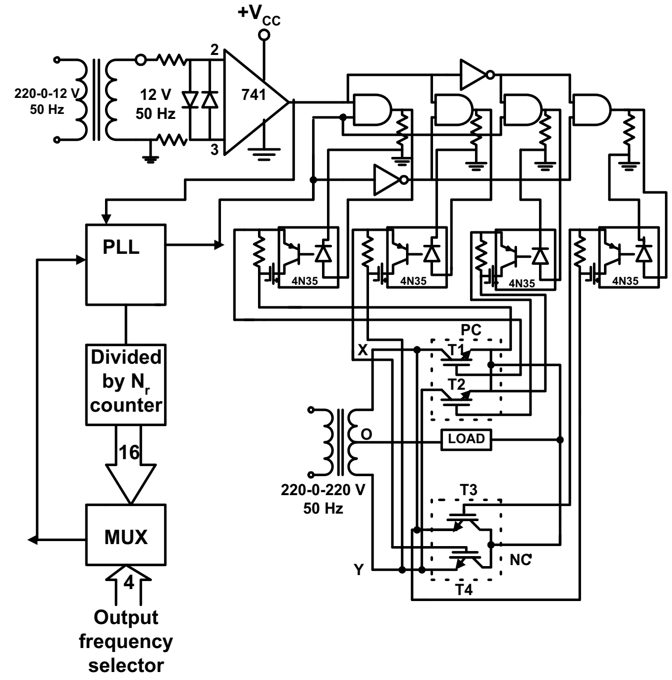

Fig. 10: System Diagram of complete set-up.

Assuming that the power factor to be 0.8, the output power of the transformer will be given as 3× 0.8 = 2.4 kW. Table 2 shows the input and output voltage and current of the module for N_r =3. The circuit has been tested for different loading conditions and average output efficiency thus obtained is approximately 90.1%.

Table 2 Input and Output voltage and current for N_r =3

$V_{in}(V)$	$I_{in}(A)$	$P_{in}(kW)$	$V_o(V)$	$I_o(A)$	$P_o(kW)$	η
220	5.5	1.21	210.7	5.2	1.0956	90%
220	10.96	2.411	210.7	10.7	2.225	92.0%
220	8.11	1.77	210.7	7.9	1.66.5	90.0%

Trigger signal for IGBTs T1 and T3 are shown in Fig. 11 for N_r = 3.

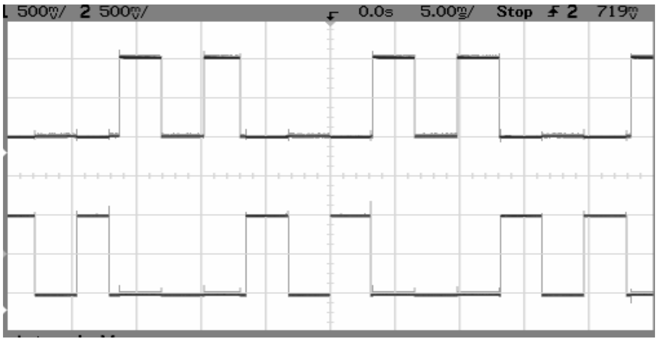

Fig. 11: Trigger signals for IGBTs T1 (upper trace: 2.5 V/div) and T3 (lower trace: 2.5 V/div) for N_r = 3

Figures 12, 13 and 14 show the trace of output voltage of proposed converter for $N_r = 2$, $N_r = 3$ and $N_r = 4$ respectively. Fig. 15 shows the combined trace of input and output voltage waveforms of the module Due to some voltage drop in the circuit the output voltage level is somewhat less than the input supply voltage level. Though the output obtained through this converter is enriched with harmonics but this can be shaped to a sinusoidal waveform by incorporating some advanced modulation techniques. The converter is designed to work satisfactory in the output frequency range of 100 Hz to 850 Hz. The range may be extended by selecting the input address of multiplexer circuit more than four bits.

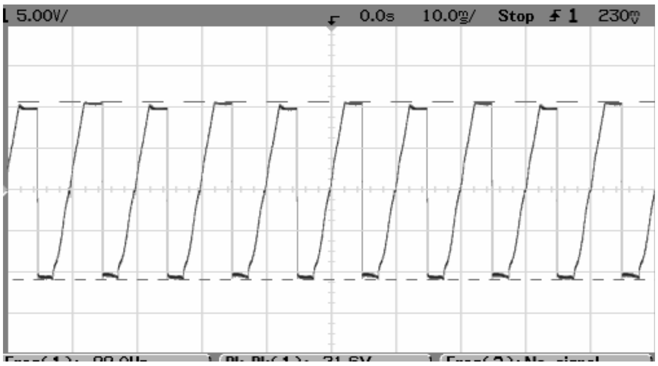

Fig. 12: Output voltage of Converter for $N_r = 2$ (50 V/div)

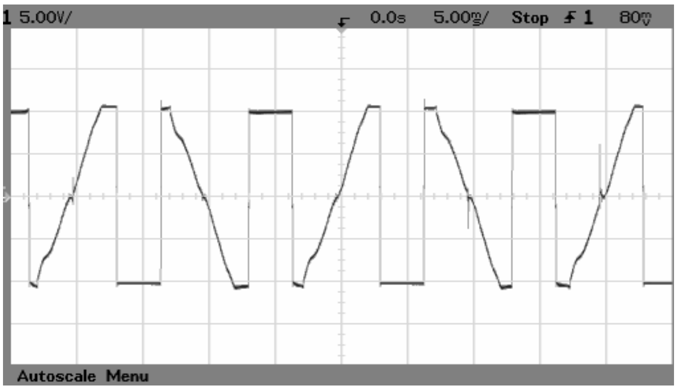

Fig. 13: Output Voltage of Converter for $N_r = 3$ (50 V/div)

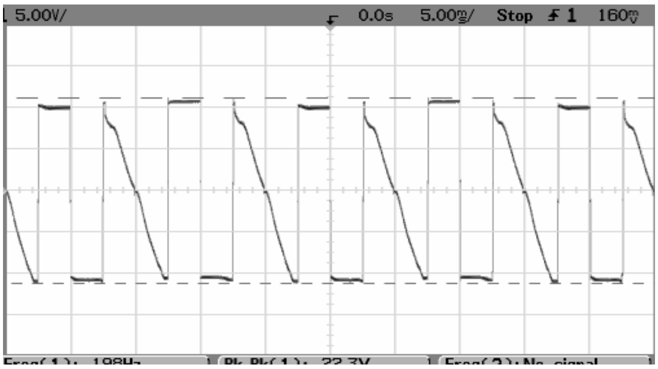

Fig. 14: Output Voltage of Converter for $N_r = 4$ (50 V/div)

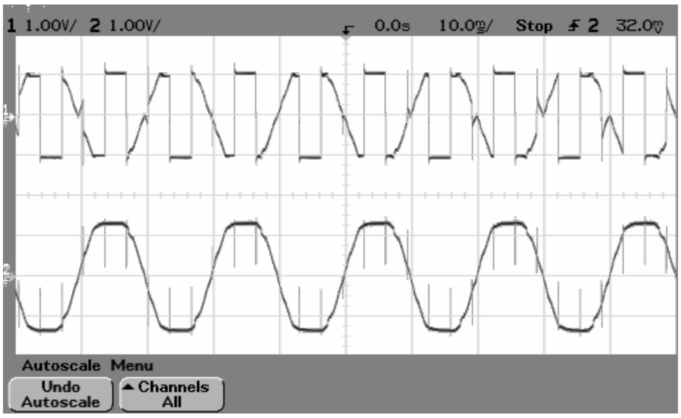

Fig. 15: Input (lower trace: *100* V/div) and output voltage (upper trace: 50 V/div) for $N_r = 3$

VI. CONCLUSIONS

A direct IGBT based AC-to-AC converter has been developed which generates an output at a frequency that is higher than the input frequency. A methodology is obtained for generating the required trigger signal for any integer multiple output frequency. Hardware realization of control circuit and power circuit has been done using readily available ICs and less expensive JK flip flops. Using the proposed design so that no new components are needed for changing the value of N_r from one value to another reduces the complexity of the control circuit. The trigger circuit has been tested qualitatively by observing the various waveforms on CRO. The operation of proposed system has been found satisfactory.

REFERENCES

[1] V. Ambrozic, M, Bertoluzzo, G. S. Buja, and R Menis, "An assessment of the inverter switching characteristics in DTC induction motor drives", IEEE Transactions on Power Electronics, Vol. 20, Issue 2, Mar 2005, pp. 457 – 465.

[2] A, Nakamori, N. Eguchi, Y. Nakanishi, "High speed large capacity inverter for power system apparatus", Decision and Control, 1996, Proceedings of the 35th IEEE, Vol. 4, 11-13 Dec. 1996, pp.4472 – 4473.

[3] W. Dong; J.-Y. Choi, Y. Li, H. Yu; J. Lai, D. Boroyevich, F.C. Lee, "Efficiency considerations of load side soft-switching inverters for electric vehicle applications", APEC, Fifteenth Annual IEEE, Vol. 2, 6-10 Feb. 2000, pp. 1049 – 1055.

[4]. G.J. Van der Merwe, L. van der Merwe, "Inverters-dynamic load responses as a result of the impressed inverter output waveform", Proceedings. ISIE '98, Vol. 1, 7-10 July 1998, pp.45 – 50.

[5] Po-Tai Cheng; S. Bhattacharya, D. M. Divan, "Control of square-wave inverters in high-power hybrid active filter systems", IEEE Transactions on Industry Applications, Vol 34, Issue 3, May-June 1998, pp.458 – 472.

[6] Du Yonggui, Xie Keming, "The SPWM inversion mode of suppressing harmonic waves based on genetic algorithm", Proceedings of the Fifth International Conference, Vol.2 Aug. 2001, pp. 1304 - 1307

[7] Vineeta Agarwal and Sachin Nema, "Resonant AC to AC", ISIE, 20-23 June, 2005, Vol.2, Dubrovnik, Croatia, pp. 495-498.

[8] J. E Quaicoe and S. B. Dewan, "Clamped Six-Pulse Cyclo-inverter with a series tuned load", IEEE Transactions on

Magnetics, Vol. MAG-21, No. 5, Sep. 1985, pp. 1717-1719.
[9] H.Sugimura, T. Ahmed, M. Orabi, H.-W. Lee, and M. Nakaoka, “Commercial Utility Frequency AC to High Frequency AC Soft Switching Power Conversion Circuit with Non Smoothing DC Link for IH Dual Packs Heater”, The 30th Annual Conference of the lEEE Industrial Electronics Society, Nov 2 - 6, 2004, Busan, Korea.

BIOGRAPHY

Vineeta Agrawal has graduated from Allahabad University, India, in 1980, and received Master’s degree in Electrical Engineering in 1984, from the same university. She joined as lecturer in 1982 in Electrical Engineering Department in M. N. R. Engineering College and since then she has been teaching in the same college. During teaching, she did her Ph.D. course in Power Electronics.

At present she is Professor and Head of Department of Electrical Engineering at Moti Lal Nehru National Institute of Technology, Allahabad. She has taught numerous courses in Electrical and Electronics. Her research interests are in single phase to three-phase conversion and AC drives. She has a number of publications in Journals and Conferences in her field. She has attended both National and International Conferences and presented papers there.

AC-DC-AC CONVERTER WITH REDUCED SWITCHES AS MATRIX CONVERTER

Sanjeevikumar P[1] and Rajambal K[2]

Abstract –This paper presents an AC-DC-AC converter as a matrix converter topology with simple commutation procedure. AC-DC-AC converter is analysed with reduced number of switches and with simple clamp circuit provides the same performance of conventional matrix converter in terms of voltage transfer ratio, unity power factor, no DC link capacitor and pure sine wave with only higher order harmonics in both line and load side around the switching frequency. Moreover the converter can utilize the conventional PWM technique on inverter side, which greatly simplifies the complexity of control. Theoretical analysis and simulation results are provided to verify its performance.

Keywords – Matrix converters, AC-DC-AC converter, Space Vector Pulse Width Modulation (SVPWM), clamp circuits.

I. INTRODUCTION

The matrix converter found revived attention recently when compared to conventional dual converter [1]-[2] with a compact structure of nine bidirectional switches to form (3x3) matrix shapes as shown in Fig.1. It has several advantages such as absence of energy storage component like capacitor or inductor, straightforward four quadrant operation and sinusoidal input current and output voltage with only harmonics around or above the switching frequency [3]-[4]. However, this topology does not found much application in industry due to potential commutation problem requiring a complex control circuit, in general, a bipolar snubber, inherent restriction to the voltage transfer ratio of 0.866 and nine bi-directional power switches. The control algorithm developed by Venturini [1] typically requires PLA (Programmable Logic Array) for avoiding commutation problem and for the implementation of PLA in the converter increases the complexity of the circuit. Several methods have been proposed to overcome the commutation problem [5]-[7] but they generally introduce a multiswitcing procedure or an additional protection circuit, which still increases the complexity. Besides this commutation problem, to attain input sinusoidal current and output sinusoidal voltage, both forward and negative sequence components must be calculated and added together. It requires very complex computational burden and additional PWM circuits.

In this paper, a matrix converter topology is analyzed in the form of conventional AC-DC-AC converter without DC link capacitor and reduced switches in the rectifier side. The performance of this AC-DC-AC converter is similar and superior to conventional matrix converter shown in Fig.1. Hence this converter can be treated as a matrix converter with the following advantages such as:

- It performs similar to conventional matrix converter such as good voltage transfer ratio capacity, four quadrant operation, unity power factor and pure sine waveforms with only higher order harmonics in both input current and output voltage.
- Conventional PWM methods can be utilized on the inverter side, which greatly simplifies its control circuit.
- No large energy storage elements like inductor or capacitor except a relatively small size ac filter at the input side are required making this filter more easily to be integrated into a system package.

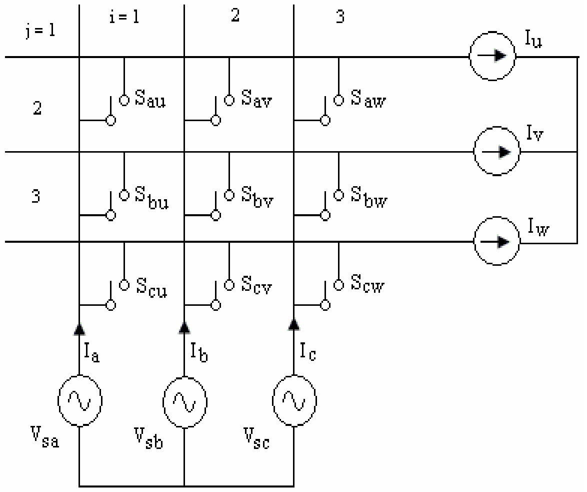

Fig. 1: Conventional Matrix Converter Topology

II. PROPOSED TOPOLOGY

Fig.2. Illustrates the structural view of the analysed matrix converter which is similar to a conventional AC-DC-AC converter but without DC link capacitor. The load side inverter is a conventional DC-AC inverter and the line side converter is a rectifier essentially consists of only three switches. Here the rectifier is operated as a current source rectifier, which is also different from conventional AC-DC-AC converter where line side converter is a voltage source rectifier [8]-[9]. The objective of the proposed converter on the line side rectifier is to maintain

---

The paper first received 8 Dec 2007 and in revised form 31 Mar 2008
Digital ref: AI70201188

[1] Simulation Solutions, Chennai, India, E-mail:sanjeevi_12@yahoo.co.in

[2] Department of Electrical and Electronics, Pondicherry Engineering College, Puducherry, India, E-mail: rajambalk@yahoo.co.in

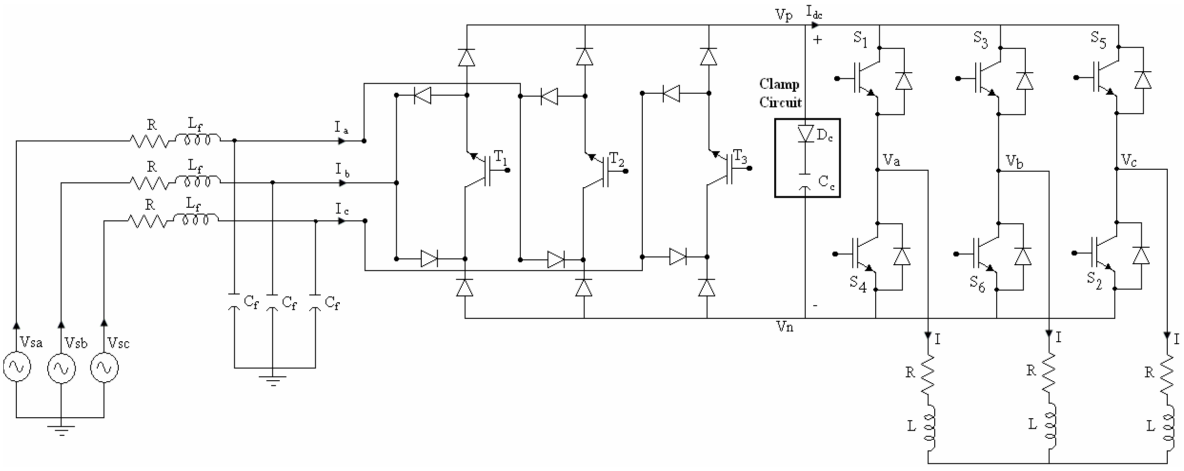

Fig. 2: Basic topology of the proposed matrix converter

a fixed DC voltage on the DC link without capacitor and improve the power factor on the input supply side. Now the capacitor in the DC link is replaced by an AC filter on the line side with a much small value to reduce higher order harmonics. Since converter has no large energy storage elements like a capacitor or an inductor it can be designed for higher capacity utilization. Conventional voltage source inverters are normally equipped with an electrolyte capacitor in their DC link which has a short life compared with an AC capacitor (metalised polyester film, etc.) [10]- [12] and also they occupy a considerably greater space in the inverter. This supports the proposed topology of AC-DC-AC converter without DC link capacitor.

A. STEPS TO REDUCE SWITCHES IN AC-DC-AC CONVERTER

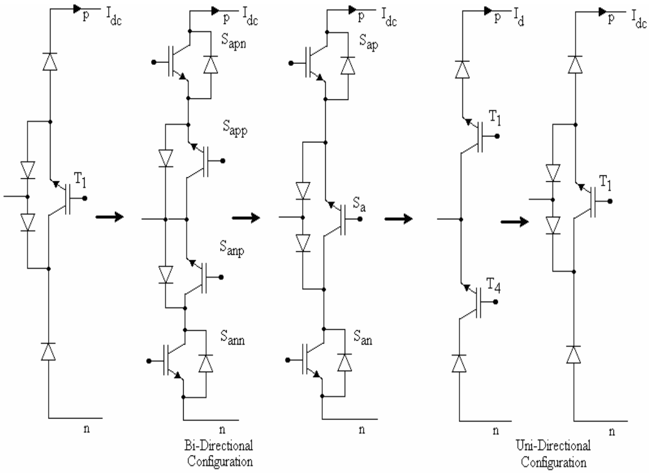

Fig. 3 – 7: Steps to reduce the Switch Number

In general, AC-DC-AC converter requires, 18 switches for current conducting, voltage blocking can be reduced by appropriate assumptions. For example, if V_p is always higher than V_n, the bi-directional switches on the load side can be replaced by uni-directional voltage blocking 6 switches on the inverter side as shown in Fig. 2 and Fig. 3 rectifier with equivalent circuit of input side phase leg "a" and the switches S_{app} and S_{anp} can share the same gate drive signal. These two switches can be replaced by one single switch and two clamp diodes. As a result, a 15-switch topology is developed as shown in Fig. 5.

If the condition that DC link current $i_{dc} \geq 0$ is guaranteed, the number of switches can be reduced to obtain 12 and 9 as shown in Fig. 6 and 7. Hence reduced switched configuration is obtained for AC-DC-AC matrix converter topology with 9 switches is shown in Fig. 2.

III. PWM METHOD ON RECTIFIER SIDE

For the purpose of analysis the values of filter components C, L and R are assumed to be zero. The switching frequency on the rectifier side is assumed to be far greater than the fundamental frequency of the input voltage. DC side voltage is essentially decided by the switching function of the rectifier and the input voltage. Analyzing the six interval of a 3Φ sinusoidal voltage of a cycle, during each interval one of the line or phase voltages will have the maximum absolute value as shown in Fig.8. Each of the switching cycle is split into two portions. For example during interval 1, V_{sa} has the largest absolute voltage, with the corresponding line voltages V_{sa}-V_{sb} and V_{sa}-V_{sc}.

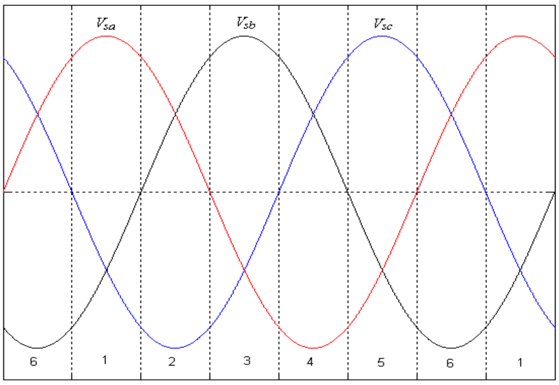

Fig. 8: Six intervals of a switching cycle

The line side switching state in each portion can be determined by the following sequence: In portion 1, for the first 30° conduction period T_1 & T_2 remain turned on;

all other line side switches are turned off. The DC side voltage V_{dc} is equal to V_{sa}-V_{sb}. In portion 2, for the next 30° conduction period T_1 and T_3 remain turned on; all other line side switches are turned off. The DC side voltage V_{dc} is equal to V_{sa}-V_{sc}. This sequence is applicable for all other intervals. By providing this switching sequence, DC voltage at the DC link can be maintained with a fixed value. Since the DC voltage is fixed, the inverter can be operated even with conventional PWM techniques.

IV. SPACE VECTOR PULSE WIDTH MODULATON ON INVERTER SIDE

SVM is an advanced computation-intensive PWM method which provides good voltage transfer capacity and reduced harmonics on the load side. SVM is possibly the best PWM techniques for inverters. The inverter is analyzed as a VSI, the three-phase output voltages V_{su}, V_{sv} and V_{sw} are supplied by the DC voltage source which is fed from the line side fully controlled current source rectifier where $V_{dc} = 3V_m/2$. Here the symmetrical conduction mode of operation of SVM is used to ensure the reduction of harmonics at the inverter output.

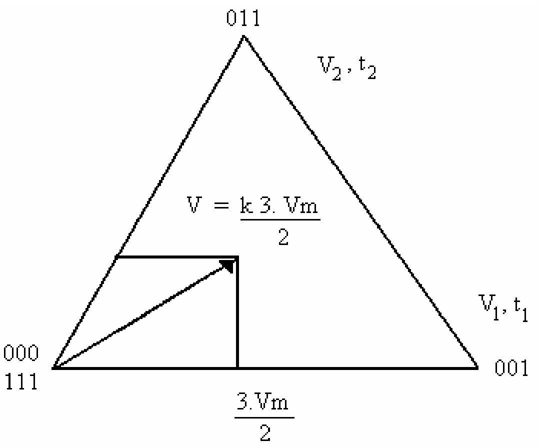

Fig. 9: Space Vector PWM for inverter during the instant $0<\theta<60^0$

In the symmetrical conduction mode, to overcome commutation problem dead time has to be introduced by allowing zero voltage vector before and after of the each conduction cycle. The duty cycle of conduction period has to be appropriately selected for the switching sequences using (1) – (3). The voltage available across the load will be kV_m where V_m is the peak voltage of the line side voltage, which ensures that the converter is similar to the conventional matrix converter. Since V_{dc} is fixed the inverter side operation is free from commutation problem. However dead time is required for its feasible operation. Fig. 9 shows the space vector PWM for inverter during the interval $0<\theta<60^0$ of the sector 1, where the output voltage $V=k.3V_m/2$.

$$T_1 = \frac{2}{\sqrt{3}}\frac{V_1}{V_2}T_c\sin(60° - \theta_s) \qquad (1)$$

$$T_2 = \frac{2}{\sqrt{3}}\frac{V_1}{V_2}T_c\sin(\theta_s) \qquad (2)$$

$$T_0 = T_c - T_1 - T_2 \qquad (3)$$

V. SIMULATION RESULTS

The proposed AC-DC-AC converter is analyzed as a matrix converter using Matlab/Simulink software for its performance. All the switches utilized are ideal switches.

Simulation parameters taken for analysis are: -

Input line Voltage = 220V
Input and Output Frequency = 60Hz
Modulation Index = 0.8
Filter Inductance = 200µH
Filter Capacitance = 900µF
Filter Resistance = 0.2 ohm
Load Inductance = 5mH
Load Resistance = 8 ohm

Switching Frequency:-

Rectifier side = 12000 Hz
Inverter side = 2000 Hz

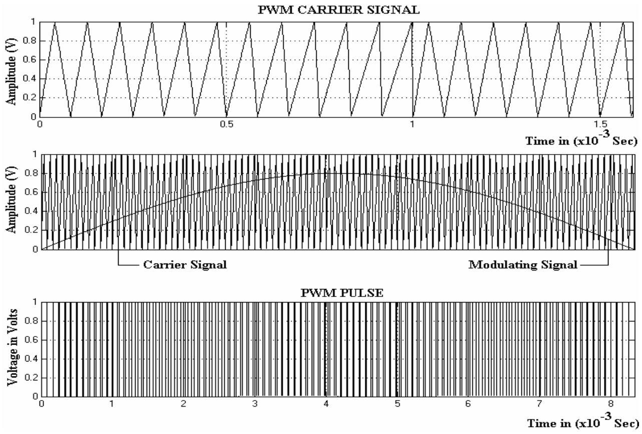

Fig. 10 – 12: PWM scheme for Rectifier

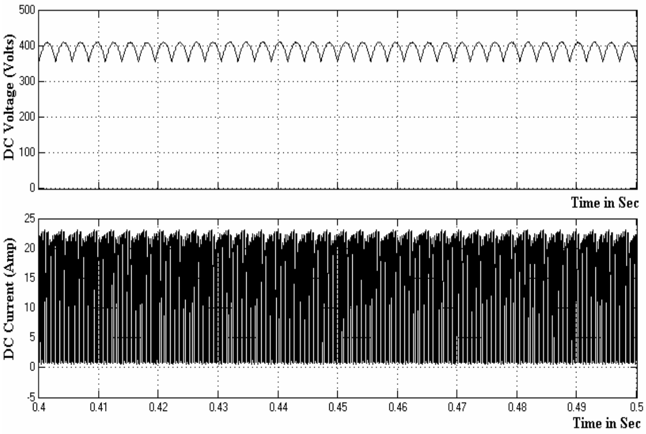

Fig. 13 – 14: DC link voltage V_{dc} and current I_{dc}

In Fig. 10 to 12 PWM signal applied to the input converter (rectifier) using sinusoidal modulation technique is given where the carrier is initially triangular in nature, which slowly changes into ramp. With this type of carrier line side THD is significantly reduced.

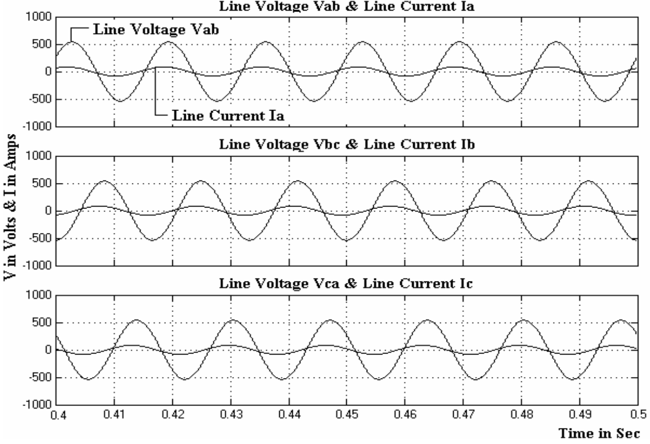

Fig. 15 – 17: Line voltage and current (Rectifier side)

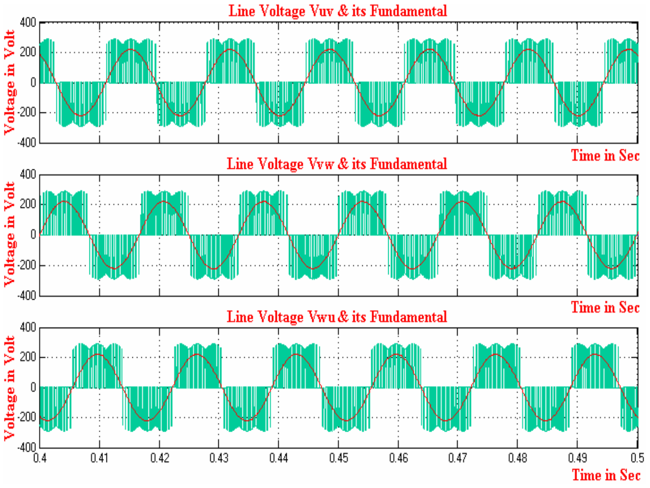

Fig. 18 – 20: Load voltage and its Fundamental

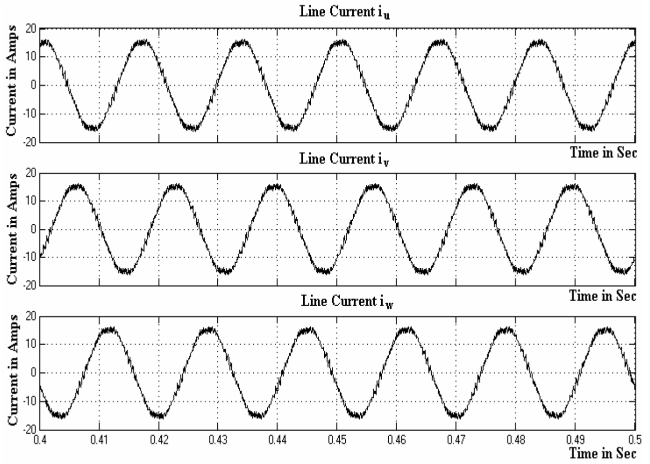

Fig.21–23: Load current showing sinusoidal characteristics

Fig. 13 to 14 depict the DC link voltage V_{dc} and current I_{dc}. Fig. 15 to 17 show the waveform of three-phase voltage and current at the input side providing leading power factor. This results that at line side there are no lower order harmonics and all other higher order harmonics are suppressed by the filter. Fig. 18 to 20 shows that three phase output voltages of the inverter (rms) are essentially sinusoidal and the fundamental component is found to be 90% of square wave operation. This in turn, demonstrates that there are no lower order harmonics in the output voltage. Fig. 21 to 23 shows that three-phase output line current (rms) are essentially sinusoidal with only harmonics above or around the switching frequency. Fig. 24 - 25 shows the THD response on Line Side Rectifier with 12000Hz Switching Frequency and on Load Side Inverter with 2 kHz Switching Frequency.

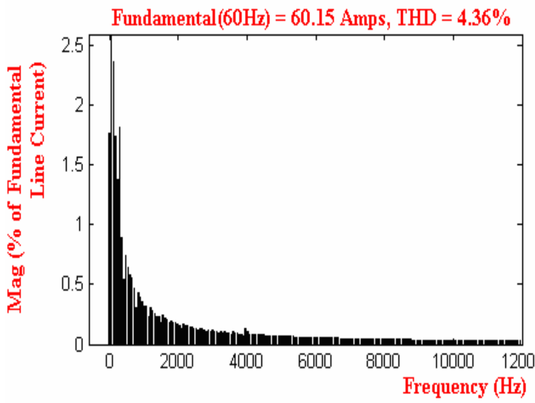

Fig. 24: THD response on Line Side Rectifier with 12000Hz Switching Frequency

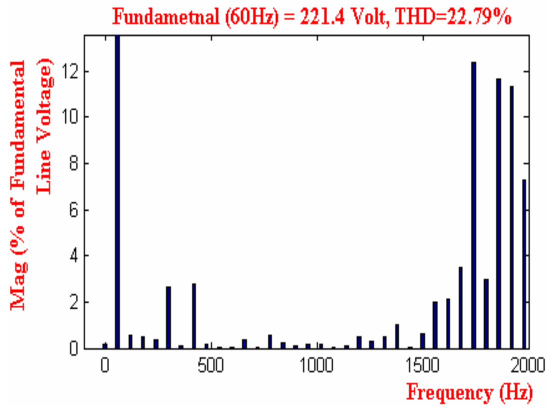

Fig. 25: THD response on Load Side Inverter with 2 kHz Switching Frequency

VI. CONCLUSION

This paper presents a successful analysis of matrix converter topology in the form of AC-DC-AC converter with reduced switch configuration and simplified commutation strategy, which reduces complexity of control when compared with the conventional matrix converter. Both the input current and output voltage are pure sine waveforms with only harmonics around or above the switching frequency. Hence filter requirement on both line and load side are reduced in size. The converter provides leading power factor at the line side and also improved power factor at the load side. Since DC link capacitor is eliminated, large capacity compact converter system can be designed. It has a good voltage transfer ratio similar to conventional matrix converter. Total Harmonic Distortion (THD) on line side is 4.36% and on the load side is 22.79%. This implies that PWM methods analyzed provide feasible results. Space vector modulation is utilized for good voltage transfer from DC link and reduced distortion. Clamp circuit requirement is reduced in size when compared to the conventional matrix converter. From the performance analysis it can be concluded that the proposed converter is free from commutation problem and has better performance than conventional matrix converter.

REFERENCES

[1] L.Huber, and D.Borojevic, "Space Vector Modulated Three-Phase to Three-Phase Matrix Converter with Input Power Factor Correction," IEEE Transactions on Industry Applications, Vol. 31, No. 6, Nov./Dec. 1995.

[2] M.Venturini, "A new sine wave in, sine wave out, conversion technique eliminates reactive component", Proc. of POWERCON, 1980, pp. E3-I-E3-15.

[3] M.G.B. Venturini, and A. Alesina, "Solid-state power conversion: A Fourier Analysis Approach to Generalized Transformer Synthesis", IEEE Trans. on Circuits & System, Vol.34, 1981, pp.310-330.

[4] D.G.Holmes, and T.A.Lipo, "Implementation of a controlled rectifier using AC-AC matrix converter theory", IEEE Trans. on Power Electronics, Vol. 7, No.1, 1992, pp. 240-250.

[5] B.Geethalakshmi, P.Sanjeevikumar and P.Dananjayan, "Performance Analysis of AC-DC-AC Converter as a Matrix Converter", Indian International Conference on Power Engineering, IEEE-IICPE'06, Chennai. 2006. pp. No.57-61.

[6] S.Kim, S.K.Sul, and T.A.Lipo, "AC/AC power conversion based on matrix converter topology with unidirectional switches", IEEE Transactions on Industry Applications, vol. 36, No. 1, 2000, pp. 139-145.

[7] J.S.Kim, and S.K.Sul, "New control scheme for AC-DC-AC converter without DC-link electrolytic capacitor", Proc. of PESC'93, 1993, 300-306.

[8] J.H. Youm, and B.H. Kwon, "Switching technique for current-controlled ac-to-ac converters", IEEE Trans. on Industrial Electronics, Vol. 46, No.2, 1999, pp.309-318.

[9] L. Wei, and T.A. Lipo, "A Novel Matrix converter topology with simple commutation", in Proc. of 36th IEEE Industry Applications Society Conf. Vol.3, Chicago, 2001, pp.1749-1754.

[10] L. Wei and T.A.Lipo, "Matrix converter with reduced number of switches", In Conf. Record of the IEEE PESC'02, June, 2002.

[11] K. Iimori, K. Shinohara, and K.Yamamoto, "Study of Dead-time of PWM Rectifier of Voltage Source Inverter without DC Link Components and Its Operating Characteristics of Induction Motor" IEEE Trans. on Industry Applications, Vol.42, Issue.2, 2006, pp.518-525.

[12] K. Mino, Y. Okuma, and K. Kuroki, "Direct-linked-type frequency changer based on DC clamped bilateral switching circuit topology", IEEE Trans. on Industry Applications, Vol.34, No.6, 1998, pp.1309-1317.

BIOGRAPHIES

P.Sanjeevikumar received Bachelor of Engineering (Electrical & Electronics) from the University of Madras and Master of Technology (Electrical Drives & Control) from Pondicherry University in 2002, 2006. He worked as a Lecturer in the Department of Electrical & Electronics Engineering in IFET College of Engineering, Tamilnadu, India (2002 – 2007). He also worked as Manager Training at Edutech LLC, Dubai, Middle East, UAE. Presently he is with Simulation Solutions as a Senior Project Engineer in Research and Development. He is currently working in the area of alternate topology for Matrix converter, Luo Converters, soft switching PWM schemes and power electronics application towards power systems. He has published papers in national, international conferences and journals in the field of power electronics and power system.

Dr.Rajambal received her Bachelor of Engineering in Electrical & Electronics, Master of Engineering in power electronics and Ph.D in Wind Energy Systems in 1991, 1993 and 2005 respectively from Anna University, Chennai, India. She is working as a Assistant professor in the Department of Electrical and Electronics in Pondicherry Engineering College, Pondicherry, India. Her area of interest includes in the fields of wind energy systems and power converter with soft switching PWM schemes.

An Unusual Full Bridge Converter to Realize ZVS in Large Load Scope

Kuiyuan Wu[1] and William G. Dunford[1]

Abstract - A current-stable switching power supply (300A) for magnet is designed on the basis of ZVS Converter and frequency-fixed PWM technology. An effective method is used to widen the load scope greatly to realize ZVS. Besides this, the saturated inductor is used to form the snubber circuit to help to solve this problem and reduce the duty cycle loss together. In this way, the noise emission and power loss were greatly reduced; the reliability of the power supply was improved obviously. This paper will introduce this effective method and analyze the working process of the converter in detail. The final experimental results are satisfactory and this switching power supply is in good use now.

Keywords – Zero voltage switching, Full bridge converter, ZVS.

I. INTRODUCTION

This converter is mainly used as a large power ZVS converter which can realize ZVS in very wide load scope, theoretically, it can realize ZVS in full load range. The combination of this kind of power converter with PFC or EMI technology, it can improve the power factor and efficiency greatly [1], [2]. In order to reduce the switching loss of the converter so as to improve the efficiency and protect the power switches, ZVS or ZCS technology is often used for high power converters, sometimes, resonant converters are chosen to solve this question [3-7]. With regard to the control method for this kind of power supply, ZVS-PWM method [8] is often used. People often use the leakage inductance of the high frequency transformer to provide energy for ZVS or ZCS realization; this will make the ZVS or ZCS scope limited [9-13]. It is very difficult to realize ZVS for the lagging leg, especially when the load is light. In order to solve this question, this paper introduces a new method to widen the ZVS scope greatly. The final experimental results suggest that this is a good method for large power converters.

This paper is organized as following: The introduction of this converter topology and the snubber circuit with saturated inductor are described in Section II. The detailed analysis of the method to realize ZVS in full load range will be presented in Section III. The experimental results are given in Section IV and finally, Section V presents the conclusion remarks.

II. THE MAIN CIRCUIT OF THE CONVERTER

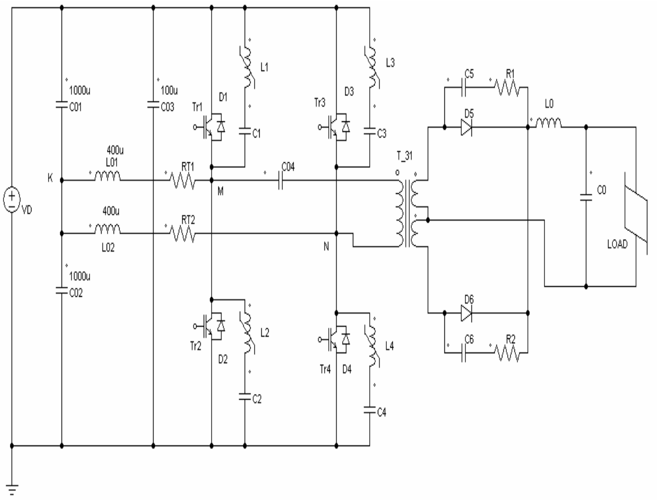

Fig. 1: The main circuit of the converter

A. The choice of the Converter frequency

A very high frequency can not be chosen for the high power switching converters with fixed frequency PWM control because of the component limit and the switching loss. Certainly, attention must be paid to make the power supply good in volume, weight, ripple, instant response speed and the cost to build it. In the end, the switching frequency of 25kHz was chosen for the main converter and the result proved it is proper. Certainly, with the improvement of the electrical cell element properties and the development of electrical technology, the frequency of the switching power supply will be higher in the future.

B. The brief statement of the main Converter Circuit

This paper only discusses the main DC-AC Converter in the power supply. Capacitors C_{01}, C_{02} , and C_{03} are the filter capacitors in the three-phase full bridge rectifier and filer circuit (~380V, 50Hz). One important reason for these three capacitors connected in this way is to connect another two RL branch in order to realize ZVS in full load range, meanwhile, C_{03} Provides a route for high frequency harmonics. In the snubber circuit, $C_1=C_2=C_3=C_4$; $L_1=L_2=L_3=L_4$.Certainly, $L_{01}=L_{02}$; $RT_1=RT_2$

II. THE DETAILED ANALYSIS OF THE METHOD TO REALIZE ZVS IN FULL LOAD RANGE.

In order to explain the working process of the converter clearly, the four control signals "V_{S1}, V_{S4}" and "V_{S2}, V_{S3}" for the four IGBTs are given in Fig. 2.

The paper first received 08 Dec 2007 and in revised form 31 Mar 2008
Digital ref: AI70201182

[1] Department of Electrical and Computer Engineering; University of British Columbia, Vancouver, BC, Canada, V6T 1Z4. Email: wu_kuiyuan@hotmail.com

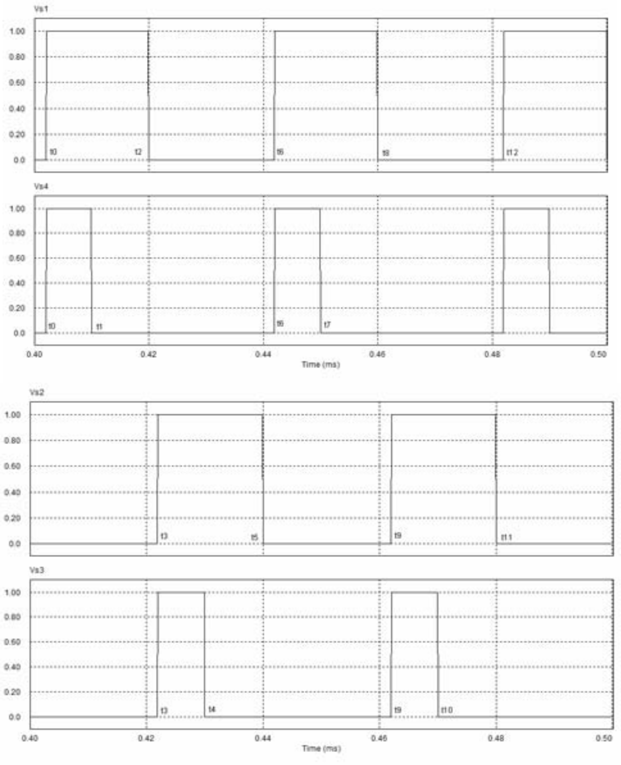

Fig. 2: The Control Signal Waves of the Converter

The time t_0, t_1, t_2 --- and t_{12} are given according to the time sequence of the four Control signals and the period begins at t_0. In this way, it will be more clearly to explain the working process of the ZVS-PWM Converter. The time between t_2 and t_3 or time delay "T_D" is equal to 2 micro-seconds.

A. Converter working process during period of t_0~t_1

1) During this period of time, it can be seen from Figure 2 that both the control signals V_{S1} and V_{S4} are valid positive voltage , so the situation in this period is the steady condition that IGBT$_1$ and IGBT$_4$ are "ON" and the main power U_d transmits energy to the load by way of IGBT$_1$ to main transformer to IGBT$_4$. During this steady period of time, the parallel LC snubber circuits of IGBT$_1$ and IGBT$_4$ are in zero voltage state because of the "ON" state of IGBT$_1$ and IGBT$_4$. This is because:

$$U_L+U_C=0 \tag{1}$$

Because the voltage applied to these two snubber circuits are DC voltage and these two snubber circuits are in steady state, the current in the series LC circuit is always equal to zero (i =0), so:

$$U_L=L\frac{di}{dt}=0(\text{v}) \tag{2}$$

So: U_c=0 (V)

2) During this period of time, the parallel LC snubber circuits of IGBT$_2$ and IGBT$_3$ are also in steady state, their voltages are:

$U_c=U_d$, $U_L=0$.

This is because IGBT$_2$ and IGBT$_3$ are in "off "state, so:

$$U_L+U_C=U_d \tag{3}$$

The same as before, under the Dc steady state, the current in series LC circuit is always equal to zero (i =0), so:

$$U_L=L\frac{di}{dt}=0\ (\text{v}) \tag{4}$$

$U_c=U_d$

3) During this period of time, the situation of these two RL circuits is discussed as following:

(a) L$_{01}$RT$_1$ Circuit: During this period of time (t$_0$~t$_1$), this circuit is in energy-storing state because IGBT$_1$ is "ON". The voltage division between C_{01} and C_{02} makes $U_k=U_d/2$, so, its differential equation is:

$$L_{01}\frac{di_{L1}}{dt}+RT_1 i_{L1}=\frac{U_d}{2} \tag{5}$$

The answer to it is:

$$i_{L1}=\frac{U_d}{2RT_1}(1-e^{\frac{-RT_1 t}{L_{01}}}) \tag{6}$$

The reason to add this circuit is to use the energy stored in inductor L_{01} to help to realize ZVS in full load scope. If the Converter only relies on the energy stored in the leak inductor of the main transformer, it will not be able to realize ZVS for the lagging leg when the load current is low. This is because the energy stored in leak inductor of the transformer will reduce when the load current decreases. However, the energy required to realize ZVS does not reduce a little and it is still two times as much as the energy stored in the capacitors in the LC snubber circuit. So:

$$\tfrac{1}{2}L_L i_p^2 < CU_d^2 \tag{7}$$

The converter will not realize ZVS when the load current is low, however, the converter can use the total energy stored in inductor L_{01} and the leak inductor L_L to realize ZVS after we add the $L_{01}RT_1$ circuit, obviously, the ZVS range of the converter will increase a lot. In this circuit, the RT_1 is a heat sensitive resistor with negative temperature coefficient (NTC) .The reason to add RT_1 to this circuit is to protect inductor L_{01}. When use series circuit $L_{01}RT_1$, the initial current in this circuit will not be too high. As the time lengthens, the resistor will dissipate electrical power and its temperature will increase and its resistance will reduce. Therefore, it will not continue consuming energy after it finished its task.

(b) The analysis of ZVS realization range.

In order to make the lagging leg of the converter realize ZVS, the energy stored in inductor $L_{01}$and the leak inductor L_L must be able to satisfy the energy requirement to charge one snubber LC circuit and discharge the other snubber circuit. That is to say the total energy stored in L$_{01}$ and L$_L$ has to be more than two times of the energy stored in capacitor C in Snubber LC circuit (The inherent capacitance of IGBT and the capacitance between the turns of the transformer are neglected because they are much less than the capacitance of Capacitor C in snubber circuit). That is:

$$\frac{1}{2}L_L I_P^2+\frac{1}{2}L_{01}I_{L1}^2 \geq CU_d^2 \tag{8}$$

where

L$_L$: Leakage inductance, it is equal to 4μH
L$_{01}$: The added inductance, it is 400μH
I$_p$: The current of the primary winding of the transformer when one IGBT in the lagging

leg is turned off
C : Capacitance in the snubber circuit, it is equal to 13000 pF
U_d : The output voltage of the rectifier and filter, it is equal to 514.86(V)

It is well known that the current changing rate in $L_{01}\ RT_1$ circuit reaches maximum when the resistance of RT_1 is equal to zero, therefore, the current value is highest after a definite period of time. Certainly, it can provide the most energy to realize ZVS, this is the situation that can realize the biggest ZVS scope. When the resistance of RT_1 is equal to zero, its differential equation is:

$$L_{01}\frac{di_{L1}}{dt}=\frac{U_d}{2} \tag{9}$$

The answer to it is: $I_{L1}(t)=\dfrac{U_d}{2L_{01}}t$ (10)

Substituting the corresponding values in the formula (8),

$$\frac{1}{2}\times 4\times 10^{-6}\times I_1^2+\frac{1}{2}\times 400\times 10^{-6}\times\frac{\frac{T^2}{4}\times(514.86)^2}{4\times(400\times10^{-6})^2}$$

$$\geq 0.003446 \tag{11}$$

Because the frequency of the converter is equal to 25kHz, $T=1/f=4\times10^{-5}$(s). Substituting this value in formula (11),

$$\frac{1}{2}\times4\times10^{-6}I_1{}^2\geq -0.029689 \tag{12}$$

This formula suggests that the power supply can realize ZVS in full load range and the heat sensitive resistor RT_1 need not be equal to zero initially.

(c) The initial Value decision of RT_1

From the discussion above, we know that the standard to decide the initial value of RT_1 is to enable the realization of ZVS in full load range. When the load current is equal to zero ($I_o=0$), certainly, the current I_1 is zero too. Therefore, formula (8) becomes into:

$$\frac{1}{2}L_{01}I_{L1}^2\geq CU_d^2 \tag{13}$$

Substituting the corresponding values in formula (13)

$$\frac{1}{2}\times400\times10^{-6}I_{L1}^2\geq 0.003446$$

So, $I_{L1}\geq4.15$ (A) (14)

This $L_{01}RT_1$ circuit will be always in the magnetic charged when $IGBT_1$ is "ON" in a half period (T/2). Therefore, the magnetic charging time for this circuit is: $\dfrac{T}{2}=2\times10^{-5}$(s).

Substituting this value in the formula (6),

$$\frac{514.86}{2RT_1}\left(1-e^{\frac{-RT_1}{400\times10^{-6}}\times2\times10^{-5}}\right)\geq 4.15$$

Its answer is: $RT_1\leq25.55$ (Ω) (15)

Therefore, if RT_1 is chosen with the resistance less than 20 Ohms ($RT_1\leq20\Omega$), it can make the converter realize ZVS in full load range.

(d) $L_{02}RT_2$ Series Circuit:

In the period of ($t_0\sim t_1$), the $IGBT_4$ is "ON", so, this circuit is in magnetic energy storing state, too. The situation of this $L_{01}RT_2$ circuit is similar to $L_{01}RT_1$ circuit. Its differential equation and the answer to the equation are the same as those of $L_{01}RT_1$ Circuit; there is no need to list them again here. Certainly, the function of this circuit is to help to realize ZVS in full load range. Because the time that IGBT4 is "ON" is "D·T/2" in this Converter, the time for $L_{02}RT_2$ circuit to store magnetic energy is "D·T/2".We choose $RT_2=RT_1$ and $L_{02}=L_{01}$. In this way, either the left leg or the right leg can act as the lagging leg and it will make no difference for the converter to realize ZVS in full load range. Certainly, this will make it more convenient for engineer to design a suitable Control Circuit for the power converter.

4) The calculation $i_p(t)$ in "$t_0\sim t_1$"

Both $IGBT_1$ and $IGBT_4$ are all "ON" from time t_0 to t_1 ($t_0\sim t_1$), so its differential equation is:

$$U_{c04}+(L_L+L_0')C_{04}\frac{d^2U_{c04}}{dt^2}=U_d \tag{16}$$

The initial values for equation (16) are:

$i_p(0+)=0$, $U_{c04}(0+)=0$

This is because the energy of C_{04} and L_L had released totally and the energy of L_o would not transfer to the primary winding of the transformer before the beginning of period of *TD/2*. This will be analyzed later. To make Laplace conversion for equation (16),

$$U_{c04}(s)+(L_L+L_0')C_{04}[s^2U_{c04}(s)-SU_{c04}(0+)]=\frac{U_d}{s}$$

$$\therefore U_{c04}(s)=\frac{U_d}{[(L_L+L_o')C_{04}s^2+1]\times s} \tag{17}$$

where
$L_L=4\mu H$
$C_{04}=10\mu F$
$L_0'=81L_o=567\mu H$

Substituting these values in formula (17)

$$U_{c04}(s)=\frac{1.1486\times10^{11}}{(5.71s^2+10^9)\times s} \tag{18}$$

Make Laplace reverse-conversion for formula (18).

$$U_{c04}(t)=514.86-514.86\cos 13229\,t \tag{19}$$

Therefore, the current of primary winding in "$t_0\sim t_1$" is :

$$i_p(t)=C_{04}\frac{du_{C_{04}}(t)}{dt}=10\times10^{-6}\times514.86\times13229\sin 13229t$$

$$=68.1\sin 13229\,t \tag{20}$$

In the period of "$t_0\sim t_1$", we can get the oscillation frequency of the primary current $i_p(t)$ from formula (20) :

$$f_1=\frac{13229}{6.28}=2106.53\ (\text{Hz}).$$

The frequency of the converter is: f=25kHz, therefore: f_1=0.08426f.

This means "T_1=11.87T". Therefore, the current of the primary winding *ip(t)* is nearly rising linearly in this period of time.

B. Period of "t_1~t_2 "

At the time t_1, Control signal Vs_4 reduces to zero, so, $IGBT_4$ will turn off at time t_1. Because the energy stored in the transformer still exists and the voltage of the secondary winding is not equal to zero, the filter inductor *Lo* in the output circuit and the energy stored in it can not release freely through the secondary winding of the transformer and the rectifier diodes. Therefore, the energy stored in inductor L_0, leak inductor L_1 and additional inductor L_{02} will be used to charge L_4C_4 snubber circuit and discharge L_3C_3 snubber circuit. Generally speaking, the energy stored in output filter inductor L_0 is much more than the energy stored in L_1 and L_{02}. Therefore, the energy needed to realize ZVS for the leading leg is enough. Certainly, the turning off of $IGBT_4$ is finished under the Zero-Voltage state. T_3 is assumed to be the time for capacitor C_3 to discharge completely. The current *ip(t)* is nearly two times of current through $L_3 C_3$ snubber circuit in this period of time. In the period of T_3, the capacitor C_3 will be discharged totally, so, the voltage Uc_3 will be equal to zero at $t_1 + T_3$, Certainly the voltage U_{L3} is equal to zero at this time . This is because: "U_{c3}=0" means that i_{c3} reaches its peak value, $U_{L3}=L\frac{di_{c3}}{dt}$ causes "$U_{L3}=0$"; Certainly, if the inductor L_3 has already saturated, its voltage will have no choice but to be zero, therefore, $U_{c3}+U_{L3}=0$. This will make the counter – parallel diode D_3 turn on, so, $IGBT_3$ is able to realize ZVS at this time. Because the control signal V_{s3} is low in this period of time, the stored energy has not released totally and $IGBT_1$ is still "ON", these will make the diode D_3 continue to be "ON". Therefore, this constitutes a free – wheeling period of time. During this period of time, the energy stored in L_L, L_{02} and *Lo* will continue to release and the voltage of the secondary winding will continue to reduce. In fact, the free-wheeling period begins at "t_1+T_3". For the wave shape of control signal and primary current during this period of time, please see Fig. 2, Fig. 3 and Fig. 4.

C. Period of "t_2～t_3"

The control signal Vs_1 will become zero at t_2 and $IGBT_1$ will turn off . The remaining energy in L_L and L_{o1} will begin to charge the L_1C_1 snubber circuit and discharge the L_2C_2 snubber circuit. At this time, the voltage of the secondary winding has already reduced to zero; so, inductor *Lo* will form the free–wheeling circuit through the output rectifier diodes and it will not take part in the ZVS realization of the main converter. If we only use leak inductor L_L to realize ZVS, it will be impossible to do so for the lagging leg when the load current is low. In order to solve this problem, we add a series circuit $L_{01}RT_1$ to guarantee the ZVS realization in full load range. When the resistance of RT_1 is lower than 20 Ω, it will be no problem to realize ZVS in full load range. Certainly, the capacitor C_2 in L_2C_2 snubber circuit will have released its stored energy completely before t_3; we assume the time needed to do so is "T_2". After the time "t_2+T_2", the parallel diode D_2 will be "ON" and this enables $IGBT_2$ to realize ZVS. From time "t_2+T_2" to time t_3, the parallel diodes D_2 and D_3 are "ON", This makes inductors L_{01} and L_L return their remaining energy to the input supply. The control signals for $IGBT_2$ and $IGBT_3$ become high at t_3 and the inductors have already released their energy totally at t_3, so, $IGBT_2$ and $IGBT_3$ begin to turn on at t_3. The input power begins to transfer energy to the output again. The waveforms of control signal and primary current are shown in Fig. 2, Fig. 3 and Fig. 4.

D. The converter working process during other periods

The method for following stages analysis is the similar to the above, so, there is no need to analyze them in detail again. In order to be convenient, the inductor *L* in *LC* snubber circuit is assumed to be a linear one in the above working process analysis. If the inductor *L* is turned into a saturated one, we only need to divide into several more stages to analyze the working process of the converter and the analysis method is the same as before. When the output current is very small, the simulation results for the current of the primary winding *ip(t)*, the voltage "*Vce1(t)*" and "*Vce4(t)*" during the whole period are as following: (The unit for "*ip(t)*" is "Ampere"; The unit for "*Vce1(t)*" and "*Vce4(t)*" is "Volt".)

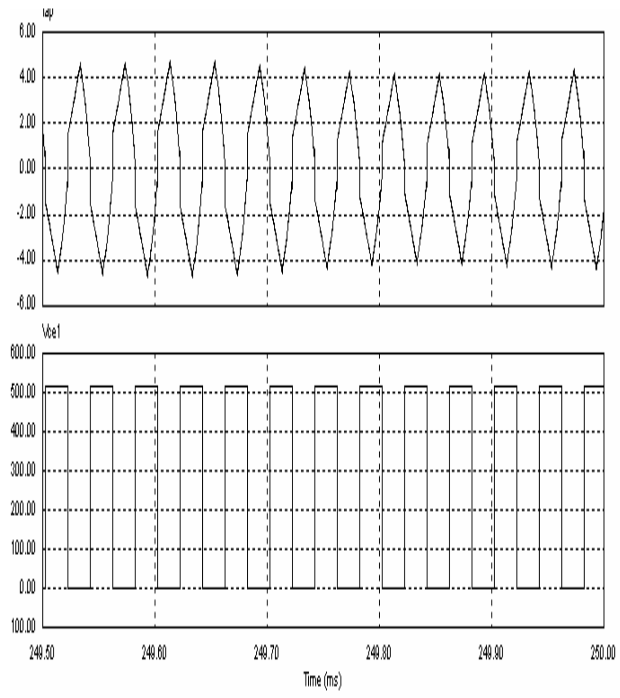

Fig. 3: $I_p(t)$ and V_{ce} of IGBT waveforms

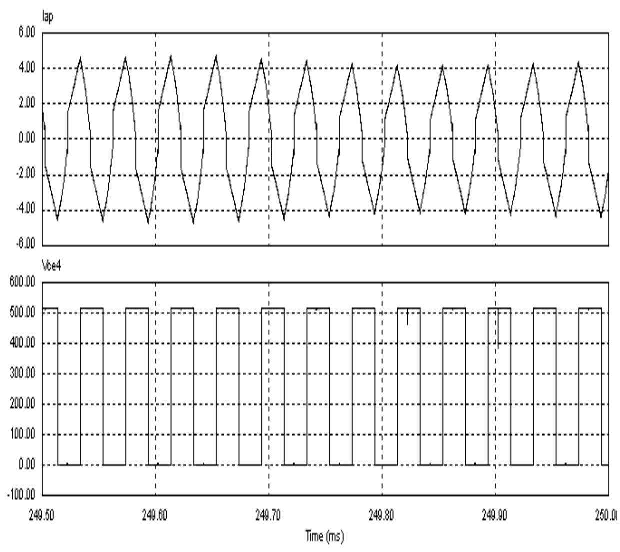

Fig. 4: I_p *(t)* and V_{ce} of IGBT$_4$ waveforms

III. THE FINAL EXPERIMENTAL RESULTS

The experimental result is satisfactory. This power supply can realize ZVS in nearly full load range (0~300A). Its current stability is: s =0.000347. Here, several working wave shapes and the current stability test curves for this power supply are listed as following.

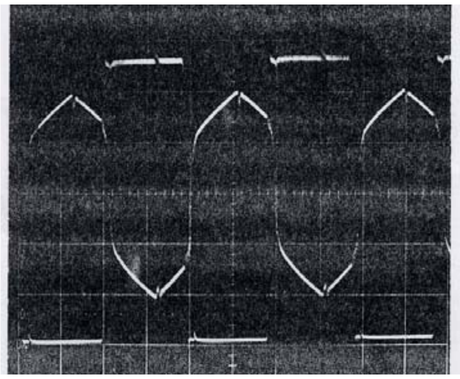

Fig. 5: I_p *(t)* and $V_{ce}$of IGBT$_1$

(V_{ce}: 100V/div; I_P *(t)*: 10A/div; *t*: 10µs/div)

In Fig. 5, the square wave is V_{ce} of IGBT$_1$; the approximate sine wave is $I_p(t)$.

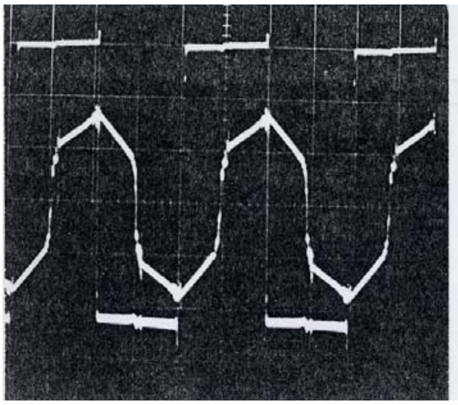

Fig. 6: I_p *(t)* and $V_{ce}$of IGBT$_3$

(V_{ce}: 100V/div; I_P *(t)*: 10A/div; *t*: 10µs/div)

In Fig. 6, the square wave is V_{ce} of IGBT$_3$; the approximate sine wave is $I_p(t)$.

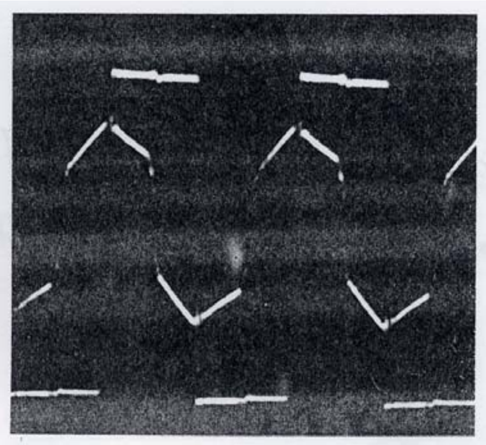

Fig. 7 I_p *(t)* and V_{ce} of IGBT$_4$

(V_{ce}: 100V/div; I_p *(t)*: 10A/div; *t*: 10µs/div)

In Fig. 7, the square wave is V_{ce} of IGBT$_4$; the approximate sine wave is $I_p(t)$. The amplitude of the square wave approximately has 5.15 grids. The amplitude of the current wave approximately has 1.8 grids. The periods of current and voltage approximately have 4 grids. From these experimental working shapes, it can be seen that this power supply has realized ZVS in a wide load scope. Although it has been already proved that this power converter can accomplish ZVS-PWM in full load scope with this method theoretically, its working station when the electrical current $I_p(t)$ is zero was not tested because this wide load scope has already reached the requirement satisfactorily. With regard to the stability of the output electrical current, please see Fig. 8; the Hall sensor was used to measure the output current and connect with the main control circuit. Because the output voltage of the Hall sensor is proportional to the output current of the power supply, its voltage can represent the output current. This curve was tested when the output electrical current is equal to 300 Amperes and the output voltage is equal to 30 Volts.

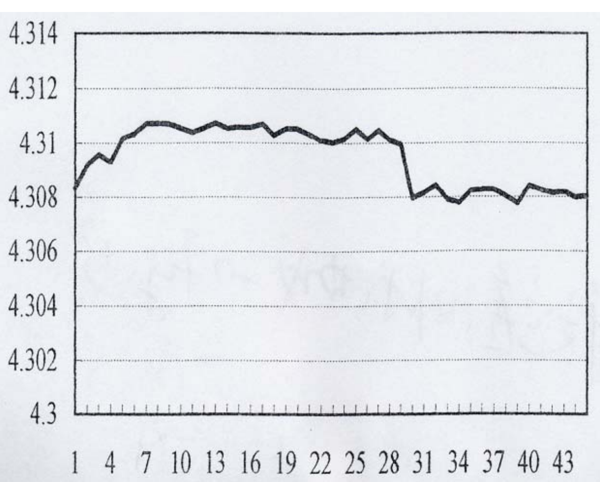

Fig. 8: The curve of the output electrical current (X-axis unit: 11minutes/div; Y-axis: Volts)

From this curve, it can be seen that *Imax* is *A8* (4.31074V) and $I_{\min}$ is $A39$ (4.30775V); and there is:

$$(A8 - A39)/2 = 0.001495;\ (A8 + A39)/2 = 4.309245$$

$$S = 0.001495/4.309245 = 0.000347$$

Therefore, the current stability is: $S = 0.000347$. This value satisfies the design requirement ($S \le 0.001$) very well. From all of these experimental results, it can be seen this method is successful to widen ZVS-PWM scope.

IV. CONCLUSIONS

The application of the saturated inductor to form snubber circuit and the additional two *RL* branches to enlarge the ZVS scope for the large power full bridge converter has been presented. The specifications of this switching power supply have been improved greatly and the converter can realize ZVS-PWM in a much more wider scope with this topology. IGBT locked-up problem can be solved and ZVS can be realized effectively with this snubber circuit. The recently developed frequency-fixed PWM control method is used for this power supply. In this way, it will make the ZVS converter work more steadily than before. The final experimental result proves that using this method is a good choice for large power full bridge ZVS converter.

REFERENCES

[1] F.Yuan, D.Y.Chen, Y.Wu and Y.Chen, “A Procedure for Designing EMI Filters for Ac Line Applications,” IEEE Transactions on Power Electronics, Vol.11, No.1, January 1996, pp.170-181.

[2] M.Nave, “Power Line Filter Design for Switched Mode Power Supplies,” New York: Van Nostrand Reinhold, 1991.

[3] W. McMurray, “Resonant Snubbers with Auxiliary Switches”, IEEE Transactions on Industry Applications, Vol.29, No.2, March/April 1993, pp.355-362.

[4] R.Erickson, A.Hernandez, A.Witulski, and R.Xu,, “A Nonlinear Resonant Switch”, IEEE Transactions on Power Electronics, Vol.4, No.2 April 1989, pp.242-252.

[5] A.Witulski, A.Hernandez, and R.ERICKSON, “Small-Signal Equivalent Circuit Modeling of Resonant Converters”, IEEE Transactions on Power Electronics, Vol.6, No.1, January 1991, pp.11-27.

[6] R.L.Steigerwald, “High Frequency Resonant Transistor Dc-Dc Converters”, IEEE Transactions on Industrial Electronics, Vol.31, No.2, May 1984, pp.181-191.

[7] K.D.T.Ngo, “Generalization of Resonant Switches and Quasi-Resonant Dc-Dc Converters”, IEEE Power Electronics Specialists Conference, 1987 Record, pp.395-403.

[8] R.Redl, L.Belogh, and D.Edwards, “Optimum ZVS Full-Bridge DC/DC Converter with PWM Phase-Shift Control: Analysis, Design Considerations, and Experimental Results”, IEEE Applied Power Electronics Conference, 1994 Record. pp. 159-165.

[9] Dhaval B. Dalal: “A 500kHz Multi-output Converter with Zero Voltage Switched”, IEEE Appl. Power Electronics Conference, 1990.

[10] G. Hua and F.C. Lee, “A New Class of ZVS-PWM Converters”, High Frequency Power Conversion Conference Proceedings, 1991, pp. 244-251.

[11] V.Vlakovic, J.A.Sabate, R.B.Ridley and F.C.Lee, “Small-signal Analysis of the Zero-Voltage-Switched Full-Bridge PWM Converter”, 1990 VPEC Seminar Proceedings (USA), pp. 19-29.

[12] K.Liu and F.C.Lee, “Zero-Voltage-Switching Technique in Dc-Dc Converters”, IEEE Power Electronics Specialists Conference, 1986 Record, pp 58-70.

[13] J.G.Cho, J.A.Sabate,and F.C.Lee, “Novel Full Bridge Zero-Voltage-Transition PWM DC/DC Converter for High Power Applications”, IEEE Applied Power Electronics Conference, 1994 Record, pp.143-149.

[14] Huang Jun: “Semi-conductor converter Technology”, Mechanical Industry Press, 1980.

[15] Zhang Li, Zhao Yong Jian “Modern Power Electronic Technology”, Science Press, 1992.

[16] Dai Zhong Da: “Modern Control Theory”, Tsinghua University Press, 1991.

[17] R.D.Middlebrook, “Null Double Injection and the Extra Element Theorem”, IEEE Transactions on Education, Vol.32, No.3, August 1989, pp.167-180.

[18] B.Kuo, “Automatic Control Systems”, New York: Prentice-Hall, Inc, 1986.

[19] D. M. Mitchell, “DC-DC Switching Regulator Analysis”, New York: McGraw-Hill, 1988.

[20] Graham C.Goodwin, Stefan F.Graebe, Mario E.Salgado, “Control System Design”, Prentice-Hall of India, 2006.

Author Index

Submission details

Only online submission will be accepted. Please first register and submit online. The paper is in double column and is similar to most IET or IEEE journal format. No page limit. Any number of pages of more than 6 will be subject to additional charge.

The paper guidelines can be downloaded using the link: http://perc.polyu.edu.hk/apejournal/

Any queries, please contact Prof. Eric Cheng, Publishing Director of APEJ, Dept. of Electrical Engineering, The Hong Kong Polytechnic University, Hung Hom, Hong Kong.
Email : eeecheng@polyu.edu.hk   Fax: +852-23301544

Any secretary support, please contact Mr. Ken Ho, Power Electronics Research Centre, The Hong Kong Polytechnic University, Hung Hom, Hong Kong.
Email : eeapej@polyu.edu.hk Tel: +852- 3400 3348   Fax: +852-23301544

Publication Details

The Journal will be published 3 times a year. The first issue was published in 2007. Response time for paper acceptance is within 3 months.

Financial Charge

All the accepted papers will be printed without charge for 6 or less pages. An additional page charge is HK$100 per page. A hardcopy of the journal will be posted to the corresponding author fee of charge. Additional copies of the journal can be purchased at HK$200 each. The charge includes postage and packing.

All Chinese Papers will be subjected to a translational fee of HK$350 per page. It will be charged when the paper is accepted for publication.

Advertising

Advertisement is welcome. Full page advertisement is HK$1000. For colour advertisement, the amount is doubled. All the advertisement will be both posted online in the journal website and hardcopy of the journal.

For advertising enquiries and details, please contact Ms. Anna Chang, eeapej@polyu.edu.hk .
Tel: +852 3400 3348   Fax: +852 2766 6156

For payment, please send your cheque, payable to ‘The Hong Kong Polytechnic University’, address to Ms. Canary Tong, Secretary of APEJ, Dept. of Electrical Engineering, The Hong Kong Polytechnic University, Hung Hom, Hong Kong.